ABSTRACT

Title of dissertation: MODELING THE ANISOTROPY OF STEP FLUCTUATIONS ON SURFACES: THEORETICAL STEP STIFFNESS CONFRONTS EXPERIMENT

Timothy J. Stasevich
Doctor of Philosophy, 2006

Dissertation directed by: Professor Theodore L. Einstein
Department of Physics

In this thesis we study the anisotropy of step stiffness: an important parameter describing the fluctuations of surface steps within the continuum step model. Using a lattice-gas framework, we derive many practical formulas for the anisotropy of step stiffness on face centered cubic {001} and {111} surfaces. We compare our formulas to experiments on Ag an Cu surfaces and thereby predict the size of nearest-neighbor, next-nearest-neighbor, and three-adatom, non-pairwise "trio" interactions between adatoms. To further corroborate our theory, we perform a series of first-principle calculations of the relevant adatom interactions. We also incorporate our formulas into simulations and model the relaxation of a Ag step initially pinned by surface impurities. Finally, we extend our theory to model Ag steps decorated by C_{60}, from which we deduce the interaction energies between C_{60} and Ag, as well as between two C_{60} molecules. Together, our work provides a consistent picture of step stiffness anisotropy from an experimental, theoretical, and numerical perspective.

MODELING THE ANISOTROPY OF STEP FLUCTUATIONS ON SURFACES: THEORETICAL STEP STIFFNESS CONFRONTS EXPERIMENT

by

Timothy J. Stasevich

Dissertation submitted to the Faculty of the Graduate School of the
University of Maryland, College Park in partial fulfillment
of the requirements for the degree of
Doctor of Philosophy
2006

Advisory Committee:
Professor Theodore L. Einstein, Chair/Advisor
Professor Ellen D. Williams
Professor John D. Weeks
Professor Janice E. Reutt-Robey
Professor Mikhail A. Anisimov

DEDICATION

This thesis is dedicated to my mom, dad, and grandma. My mom for her imagination, my dad for his logic, and my grandma for showing me how to balance the two.

ACKNOWLEDGMENTS

First and foremost, my heartfelt thanks to my family and friends, without whom I would not be writing this now. My deepest thanks go to my wife, Ayumi. Her continued love, patience, and support have smoothed and balanced the journey. I would also like to deeply thank my advisor, Ted Einstein. His guidance and critical eye have made this thesis a reality. My undergraduate advisor, Jeff Prentis, also deserves many thanks. His inspirational lectures and after-hours discussions continue to guide my research. Big thanks to all the other teachers who have shown me how to think and find the truth. Among those at MRSEC, Ellen Williams deserves my special praise, not only for first hiring me, but also for her help and support along the way. Among my coauthors, I'd like to thank Royce Zia, without whom my first "first-author" paper would not have been. I'd also like to thank all of my office-mates. Big thanks, in particular, to Hailu Gebremariam, who has always been a joy to work with and talk to. Many thanks as well to Masashi (Tosh) Degawa, for his friendly advice and interesting perspective about Japan, and to Chenggang Tao for his friendship, experimental expertise, and (table) tennis passion! Among the administrative staff, my heartfelt thanks to all at MRSEC and UMD-physics, especially Jane Hessing, who has been wonderfully helpful and supportive throughout the years. Finally, big thanks (and apologies) to the countless I've failed to mention but, nonetheless, have helped me along the way. Thank You.

TABLE OF CONTENTS

Chapter 1

Introduction and Background

1.1 Motivation

We live in a fast evolving world, where the demand for smaller technology continues to grow exponentially. To keep pace, our knowledge of physics at ever-smaller length scales must also grow. Modern electronics components are so small, for example, that thermal effects are important. For these tiny systems, motion is jerky and chaotic instead of smooth and predictable. Such a radical environment severely limits our ability to engineer and ultimately fabricate micro-devices. Components in future technological applications will therefore not be built and assembled piece by piece, like traditional manufacturing techniques. Instead they will be grown or self-assembled, probably on template surfaces,[1] as modern computer chips are already made. Before this process can be controlled, however, it must first be theoretically understood and ultimately modeled. With this goal in mind, surface morphology, which will undoubtedly play a crucial role in the manufacturing process, has been the focus of significant research lately.

Among the surfaces studied, stepped and/or vicinal surfaces are perhaps the most technologically relevant. These surfaces are formed when a solid is cut or grown close to a crystalline high-symmetry orientation at moderate temperatures (below the high-symmetry surface roughening transition), making them smooth to

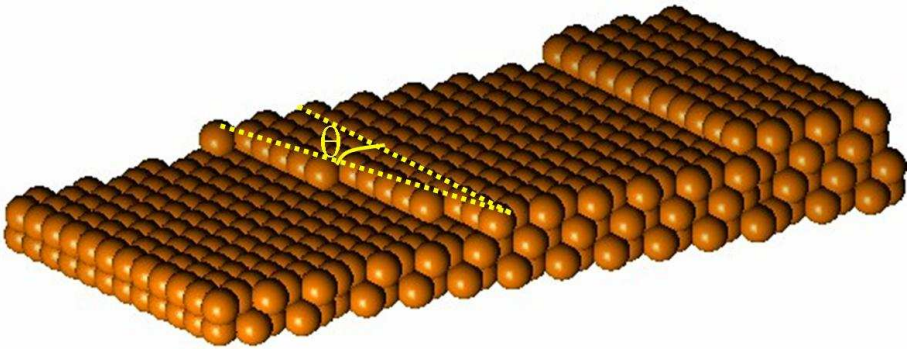

Figure 1.1: A depiction of two steps forming part of a {111} vicinal surface. Each sphere represents an atom. The upper step is oriented along the high-symmetry, close-packed direction, while the lower step makes an angle θ with respect to that direction.

the macroscopic touch. Closer inspection, however, reveals a series of atomically flat terraces separated from one another by steps: surface boundaries where the height changes by an atomic unit (see Fig. 1.1). As already hinted at, stepped surfaces have great commercial potential; not only can they serve as substrates and templates for the controlled growth of engineered microstructures, such as quantum dots,[2] but their constituent steps and terraces are potential catalysts for chemical and biological reactions.[1]

Properly modeling stepped surfaces is intrinsically a multi-scale problem. Unlike gas and liquid interfaces, stepped surfaces are inherently anisotropic, meaning many of their properties depend on orientation with respect to crystal structure. Whereas the source of anisotropy is the simple packing arrangement of atoms, the effects of anisotropy can be seen at all length scales. At the microscopic scale, for example, crystal anisotropy causes surface adatoms and defects to move more easily in some directions than others. This in turn is reflected at the mesoscopic scale through the anisotropic energies, fluctuations, and interactions of surface steps.

At the macroscopic scale, this anisotropy appears in the growth, shapes, and self-assembly of large surface structures,[2–4] and ultimately in the surface morphology as a whole, familiar to most in the striking shapes of precious and semi-precious gems such as amethyst and diamond. Understanding surface anisotropy at all length scales is therefore technologically practical, albeit technically demanding.

The real challenge in constructing a multiscale model is properly bridging the relevant time and length scales. Whereas a macroscopic stepped surface appears smooth and is best described by traditional continuum theory, a microscopic stepped surface is discrete (since individual atoms are resolved), making it best described by density functional theory or molecular dynamics. Connecting these two extremes involves at least six orders of magnitude in both space and time. Ideally one would construct a model that retains atomic resolution, so that crystal anisotropy is naturally included. Unfortunately, the computational demands of this approach makes simulations of experimentally relevant time and length scales (millimeters and seconds) nearly impossible.

A powerful alternative approach, employed by the continuum step model,[5] describes the evolution of stepped surfaces through the collective motion of their constituent mesoscopic steps. Here, each step is coarse-grained in the direction parallel to its edge, making it mathematically continuous and well behaved. The step appears to move and fluctuate as adatoms attach to it, detach from it, and move along it. The fluctuations and net movement of steps not only reflect the underlying dynamics of adatoms, but also control the overall surface morphology. Here, anisotropy is introduced with empirical parameters for the steps that can ultimately

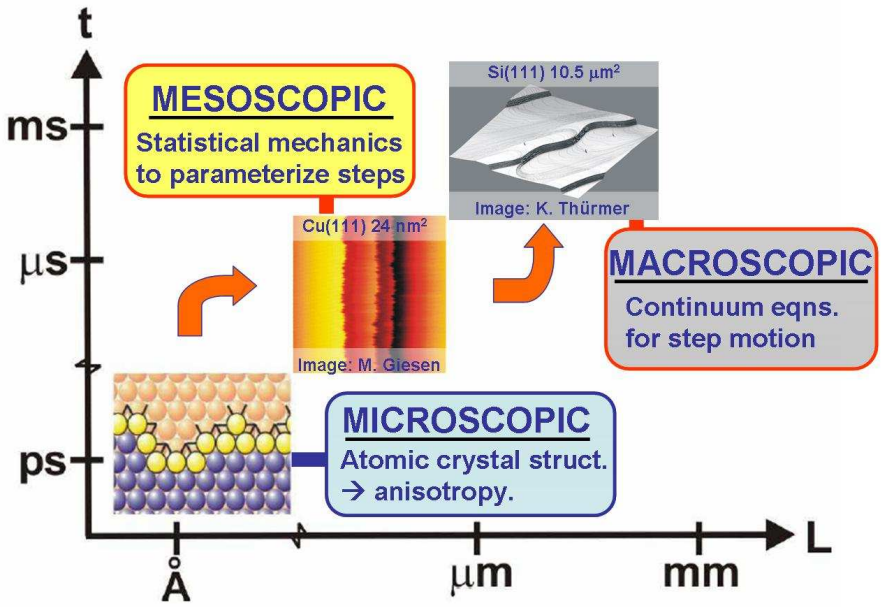

Figure 1.2: A schematic showing the vast range of time and length scales required when modeling vicinal surfaces. The lower-left figure represents the microscopic scale, where individual surface atoms are resolved and events take place on the order of picoseconds. In this domain, density functional theory can be used to precisely calculate the interaction energies between atoms (bond strengths). The middle figure depicts the mesoscopic domain, where atoms are no longer resolved and steps become the dominant surface feature. Here steps appear to move and fluctuate by themselves because atoms are constantly attaching to them, detaching from them, or running along them. The parameters describing steps can be linked to the microscopic domain via statistical mechanics. Finally, the upper-right figure depicts the macroscopic domain, where the surface is composed of countless continuous steps, all moving and interacting with one another, ultimately controlling how the surface evolves. This is the domain of the continuum step model, which describes surface evolution through a set of continuum differential equations relating the step parameters.

be linked to microscopic interactions using statistical mechanics (via lattice-gas models, for example). Steps are therefore convenient, coarse-grained structures that provide a bridge between the discrete, microscopic world of atoms and the continuous, macroscopic world of experimentally relevant stepped surfaces (see Fig. 1.2).

Within the continuum step model, steps are described with just three parame-

ters: the step stiffness, the adatom mobility, and the step-step interaction strength. For isolated steps, perhaps the most important parameter is the step stiffness, which measures how easily a step fluctuates or wanders perpendicular to its mean orientation. Because of crystal anisotropy, the step stiffness depends on the local step angle, measured from the the high-symmetry, close-packed direction (see the lower step in Fig. 1.1). Formally, the stiffness is derived from the step line tension, or step free energy per unit length, which is just the one-dimensional analog of surface tension. While the line tension controls the equilibrium shapes of single-layer clusters of atoms or vacancies (which can be thought of as steps that close in on themselves and are often referred to as "islands"), the stiffness controls the relative size of fluctuations *about* the equilibrium shape. A precise theoretical description of step stiffness, including its anisotropy, is thus an essential ingredient for modeling the dynamics of stepped surfaces using the continuum step model.

In this thesis, we will focus almost exclusively on the anisotropy of step stiffness, for which it turns out to be difficult to derive general, explicit formulas. To date, most experimental and numerical treatments vastly oversimplify matters, either ignoring the anisotropy altogether, or including it in a simple sinusoidal form that reflects the underlying surface symmetry. Here we will attempt to rectify this situation by clarifying the origin and role of step stiffness anisotropy, while also simplifying its application within experiments and simulations.

This thesis is organized as follows: In the remainder of this Chapter we discuss the historical origin of step stiffness, as well as describe its context within the continuum step model. In Chapters 2 and 3 we use a lattice-gas framework to solve

for the step stiffness anisotropy in terms of surface adatom interactions, first for fcc {001} and then for fcc {111} stepped surfaces. In both Chapters we compare simple and practical low-temperature formulas for the stiffness anisotropy with experimental data. Towards the end of Chapter 3 we also extend our formalism to describe a novel experimental system: Ag(111) steps fully decorated by a single layer of C_{60}. In Chapter 4 we further validate the derived formulas for step stiffness using VASP (the Vienna Ab-initio Simulation Package) to perform first-principles, quantum mechanics calculations of the relevant adatom interactions. There we show that even simple, homogenous systems such as Cu can have significant non-pairwise adatom interactions. Next, in Chapter 5, we show how our formulas can straightforwardly be incorporated into simulations of the continuum step model, allowing for quantitative comparison with dynamic experiments that provide new insight into the anisotropy of step-edge adatom mobility, the remaining parameter describing isolated steps within the continuum step model. Finally, in Chapter 6, we offer a summary of results, as well as concluding remarks and challenges for the future.

1.2 Step Stiffness: History and Background

Step stiffness is an intuitive parameter, describing how easily a mesoscopic surface step bends. As the name suggests, the stiffer a step, the less it fluctuates. The step stiffness, which we will refer to as $\tilde{\beta}(\theta, T)$, depends on both the local step angle θ (again, measured from the high-symmetry, close-packed direction) and the temperature T. An intuition for these dependencies is easily obtained by focusing

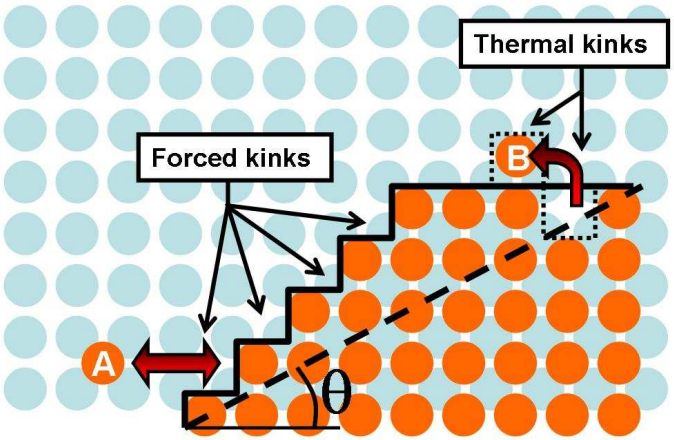

Figure 1.3: An overhead illustration of a step edge (solid, black line) with local orientation angle θ. Dark, orange spheres are adatoms, while lighter, blue spheres are surface atoms. Here a lone terrace adatom, labeled "A," is in the process of attaching or detaching from the step edge. Adatom "B," on the other hand, is thermally excited out of an energetically favorable close-packed position, forming four thermal kinks in the process (shown here as a dotted line). The remaining kinks are all forced, meaning they must be present to give the step its orientation. The step appears to fluctuate as adatoms move along the step edge and attach and detach from it.

on the microscopic origin of step fluctuations: the constant movement of adatoms nearby and along surface steps.

From the perspective of a lone terrace adatom, labeled "A" in Fig. 1.3, a step edge is an energetically favorable place because it allows the adatom to form additional bonds with the constituent step-edge adatoms. If the adatom attaches to a close-packed step ($\theta = 0$), every attachment site is equivalent, so movement from one site to another is relatively easy. In this case, the adatom will usually hop along until it eventually finds a step-edge kink, a deviation from the close-packed direction that is even more energetically favorable because the adatom can nestle into the kink corner and form additional bonds to other step-edge adatoms.

As the adatom attaches to the kink site, the kink itself appears to move, making the step appear to fluctuate. (Note that a single adatom on a close-packed step is itself equivalent to two step-edge kinks.) From this perspective, kinks are the predominant source of step fluctuations, and the more kinks a step has, the more it fluctuates. This means that steps oriented near the close-packed direction tend to be stiffer than those closer, since steps nearer generally have fewer kinks.

To understand the temperature dependence of $\tilde{\beta}(\theta, T)$, it is useful to divide step-edge kinks into two types: those that are geometrically forced, and those that are thermally activated. Forced kinks must be present to give a step an overall orientation angle θ. Thus, close-packed steps have no forced kinks, whereas steps with angle θ have a density $\tan\theta$ of such kinks, as depicted in Fig. 1.3. All other kinks are thermally activated. As the temperature rises, the number of thermal kinks initially increases exponentially, causing the step stiffness to decrease. Eventually, the number of thermal kinks far surpasses the number of forced, causing all steps to fluctuate in roughly the same way, regardless of step angle θ. Thus, as a rule of thumb, step stiffness decreases with an increase in temperature, and simultaneously becomes more isotropic.

Mathematically, the step stiffness is defined in terms of the step line tension $\beta(\theta, T)$:

$$\tilde{\beta}(\theta, T) \equiv \beta(\theta, T) + \beta''(\theta, T), \tag{1.1}$$

where the prime denotes differentiation with respect to θ. Experimentally, the relative line tension can be directly measured from the equilibrium crystal shape (ECS)

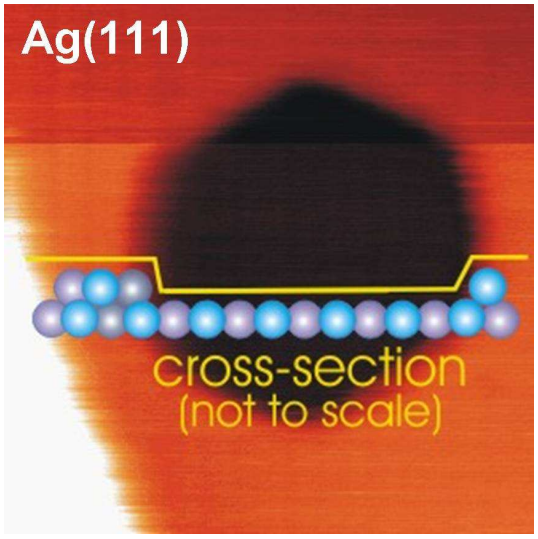

Figure 1.4: An STM image of a hexagonal vacancy island on Ag(111) at room temperature. The overlay shows a cartoon slice through the island as viewed from the side that clearly illustrates the monolayer depth of the island (which might be more appropriately called a pit). STM image courtesy of Margaret Giesen.

of adatom and vacancy islands through the famous Wulff construction. Remember these islands are just groups of adatoms (vacancies) that come together and form a two-dimensional crystal on top of (within) the surface. The shapes of these islands are relatively simple, aside from distortions due to thermal effects. For example, Fig. 1.4 shows a vacancy island on Ag(111) at room temperature which clearly has a hexagonal shape. The essential idea is that steps bounding the ECS are oriented at thermodynamically favorable angles (angles having minimal line tension). The more favorable a given step angle is, the more that step angle appears on the ECS. Geometrically, the Wulff construction has a simple interpretation. If $\beta(\theta, T)$ is plotted in polar coordinates and a line is drawn perpendicular to the curve at every angle, then the region enclosed by all of the perpendicular lines is the ECS, within a constant. This is depicted in Fig. 1.5, along with the generic temperature

dependence of $\beta(\theta, T)$ and the ECS.

At absolute zero, the ECS is most anisotropic. Assuming adatoms only interact with nearest-neighbors, the ECS is a perfect square for islands on face-centered-cubic (fcc) {001} surfaces and a perfect hexagon for islands on fcc {111} surfaces. This makes sense because at absolute zero there are no thermal effects, so the ECS is composed of steps with the lowest line tension, namely, close-packed steps. As the temperature rises, however, the ECS corners become thermodynamically unfavorable, causing them to round. Simultaneously, thermal kinks begin to form and $\beta(\theta, T)$ begins to drop. Near the critical temperature T_c, both the ECS and $\beta(\theta, T)$ become circular. Exactly at T_c, $\beta(\theta, T_c) = 0$, so steps proliferate and the surface becomes rough. For obvious reasons, this transition is called the "roughening transition."

This generic behavior is consistent with our intuition of the step stiffness as

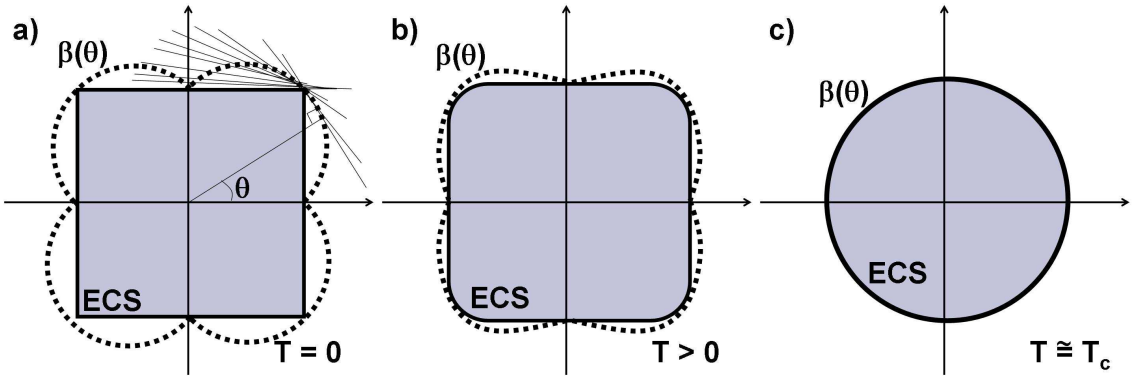

Figure 1.5: By applying the Wulff construction to the polar plot of $\beta(\theta, T)$ (thick, dotted line) the ECS (thick, solid line) is obtained. In (a) the process is depicted for an island on an fcc (001) surface at $T = 0$, when the ECS is a perfect square assuming adatoms only interact with nearest neighbors. At temperature above absolute zero, the corners of the ECS begin to round, as shown in (b). At higher temperatures still, near the critical temperature T_c, both $\beta(\theta, T)$ and the ECS become circular.

described above. At high temperatures, $\beta(\theta, T)$ is a circle, so $\beta''(\theta, T) = 0$. Combining this observation with Eq. (1.1) implies the high-temperature step stiffness and line tension are more or less equivalent. At these temperatures, the stiffness, like the line tension, is isotropic, as our intuition suggested. (Remember at high temperatures the number of thermal kinks becomes so great, all directions look more or less equivalent.) At lower temperatures, the stiffness and line tension begin to differ, especially near high-symmetry directions ($\theta = 0$, $\pi/2$, $3\pi/4$, and π in Fig. 1.5), where cusps in $\beta(\theta, T)$ begins to form, causing $\beta''(\theta, T)$ to diverge exponentially. This means that the low-temperature stiffness is very anisotropic, again, as our intuition suggested. (Remember, at low temperatures, forced kinks—the number of which change with step angle—are the predominant source of fluctuations).

1.2.1 Step Stiffness as a Gauge for Step Bending

The significance of step stiffness was not fully appreciated until fairly recently. Traditionally, it was assumed that $\beta(\theta, T)$ was the key thermodynamic parameter describing step fluctuations. To a certain extent this is true. As long as the temperature is relatively high, $\beta(\theta, T) \approx \tilde{\beta}(\theta, T)$. However, at low temperatures the assumption fails, and the stiffness gains a character all its own.

The argument was first laid out in a response[6] from Fisher, Fisher, and Weeks to a paper on capillary waves and surface tension by D. B. Abraham.[7] In his paper, Abraham calculated exactly, via the nearest-neighbor Ising model, several properties of one-dimensional interfaces (steps for our purposes). His results generally agreed

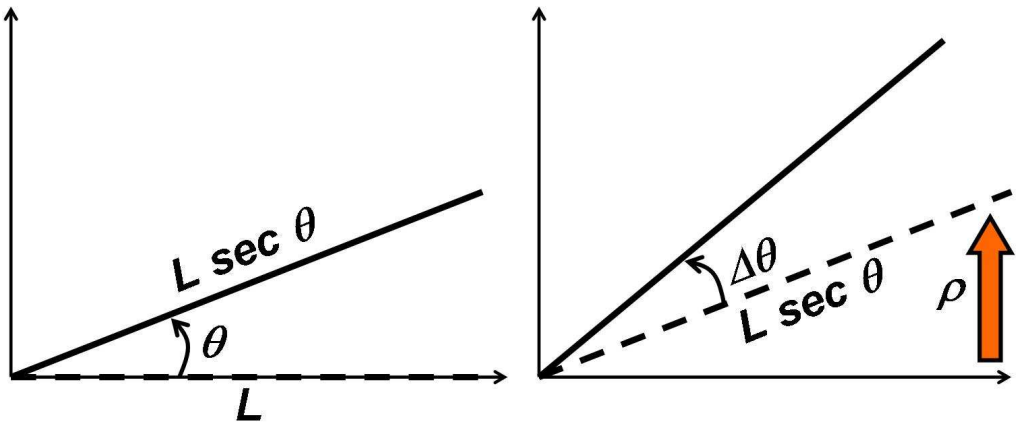

Figure 1.6: In the left image, a close-packed step fluctuates θ about its equilibrium angle $\theta = 0$ (dashed line). In the right image, a step "torqued" by an amount ρ fluctuates $\Delta\theta$ about its equilibrium angle θ (dashed line).

with the more traditional capillary-wave theory, but with the wrong coefficients involving the line tension. In their response, Fisher, Fisher, and Weeks argued that there was no disagreement, as long as the anisotropy of the line tension is considered, so that the line tension is replaced by the stiffness!

The basic idea is straightforward. Imagine a close-packed step ($\theta = 0$) of length L. What is the free energy required to bend the step, or tilt it by a small amount θ? In the process of bending the step, the length increase to $L' = L \sec\theta$, as shown in the left image of Fig. 1.6. The change in free energy ΔF is thus

$$\begin{aligned} \Delta F &= L'\ \beta(\theta,T) - L\ \beta(0,T), \\ &= L\sec\theta\ \beta(\theta,T) - L\ \beta(0,T). \end{aligned} \tag{1.2}$$

Now, if θ is small, we can Taylor expand both $\beta(\theta,T)$ and $\sec\theta$ about $\theta = 0$:

$$\beta(\theta,T) = \beta(0,T) + \beta'(0,T)\ \theta + \frac{1}{2}\beta''(0,T)\ \theta^2 + ..., \tag{1.3}$$

$$\sec(\theta) = 1 + \theta^2/2 + ... \tag{1.4}$$

Plugging these into Eq. (1.2) and noting by symmetry that $\beta'(0,T) = 0$, as our Wulff plots in Fig. 1.5 convey, we find

$$\Delta F \approx \frac{1}{2} L \left[\beta(0,T) + \beta''(0,T)\right] \theta^2. \tag{1.5}$$

Notice the last term is not proportional to the line tension alone, but rather the line tension plus its curvature, a.k.a, the stiffness. In their response they wrote: "The resistance to small distortions, which form the basis of capillary-wave theory, is thus controlled by an 'effective' interface tension." This "effective" tension was later appropriately coined stiffness, since it measures how easily a step thermodynamically bends, as Eq. (1.5) suggests.

One shortcoming of the above argument is that it only works when $\beta'(0,T) = 0$, which is generally only true for close-packed steps. An obvious question then arises: Does the argument still hold for steps at arbitrary angles? The answer is yes, as first discussed by Leamey et al.[8] and further developed by the Akutsus.[9] In the Akutsu's paper, they consider a step having orientation angle θ and length $L \sec\theta$. They treat θ as a fluctuating variable by introducing the Andreev free energy[10] $G(\rho,T)$, related through a Legendre transform to $F(m \equiv \tan\theta, T)$ (here we bury the θ dependence into the step slope m) :

$$\begin{aligned} G(\rho,T) &= \min_m \tilde{G}(m,\rho,T) \\ \tilde{G}(m,\rho,T) &\equiv F(m,T) - \rho m \end{aligned} \tag{1.6}$$

where ρ—the conjugate variable to m—can be thought of as a "torque" that maintains the slope (see the right image in Fig. 1.6). The equilibrium step slope m^* and

angle θ^* are determined by minimizing $\tilde{G}(m,\rho,T)$ with respect to m, as Eq. (1.6) suggests. More explicitly, we have

$$\frac{\partial \tilde{G}(m,\rho,T)}{\partial m} = 0 \;\Rightarrow\; \frac{\partial F(m,T)}{\partial m} = \rho. \tag{1.7}$$

The last equality yields m^* as a function of ρ, which is inserted into $\tilde{G}(m,\rho,T)$ to complete the Legendre transformation and yield the Andreev free energy $G(\rho,T) \equiv \tilde{G}(m^*(\rho),\rho,T)$. Just as the Helmholtz free energy is the appropriate potential describing systems at constant temperature, the Andreev free energy is the appropriate potential describing steps subjected to a constant "torque" ρ. We will revisit the Andreev free energy $G(\rho,T)$ later in Chapter 2, where we derive an analytic formula for the step stiffness anisotropy on fcc $\{001\}$ surfaces.

To continue our argument, we consider the change in $\tilde{G}(m,\rho,T)$ when a step with equilibrium slope m^* is tilted away from that slope by an amount $\Delta m \equiv m - m^*$. We begin by expanding $\tilde{G}(m,\rho,T)$ about m^*:

$$\tilde{G}(m,\rho,T) = G(\rho,T) + \left.\frac{\partial \tilde{G}(m,\rho,T)}{\partial m}\right|_{m=m^*} \Delta m + \frac{1}{2}\left.\frac{\partial^2 \tilde{G}(m,\rho,T)}{\partial m^2}\right|_{m=m^*} (\Delta m)^2 + ... \tag{1.8}$$

It follows from Eq. (1.7) and Eq. (1.6), respectively, that

$$\left.\frac{\partial \tilde{G}(m,\rho,T)}{\partial m}\right|_{m=m^*} = 0, \tag{1.9}$$

$$\left.\frac{\partial^2 \tilde{G}(m,\rho,T)}{\partial m^2}\right|_{m=m^*} = \left.\frac{\partial^2 F(m,T)}{\partial m^2}\right|_{m=m^*}, \tag{1.10}$$

so we can bring $G(\rho,T)$ to the other side of Eq. (1.8) and find

$$\Delta\tilde{G} \equiv \tilde{G}(m,\rho,T) - G(\rho,T) \approx \frac{1}{2}\left.\frac{\partial^2 F(m,T)}{\partial m^2}\right|_{m=m^*} (\Delta m)^2. \tag{1.11}$$

Finally, we note that $F(m,T) = \beta(m,T)\ L\sec\theta = \beta(m,T)L\ \sqrt{1+m^2}$, so that

$$\frac{\partial^2 F(m,T)}{\partial m^2} = \tilde{\beta}(m,T)\ L\cos^3\theta, \tag{1.12}$$

while

$$\Delta m = \sec^2\theta\ \Delta\theta. \tag{1.13}$$

Plugging these into Eq. (1.11), we have our final result (where we once again highlight the θ dependence implicit in m):

$$\Delta\tilde{G} \approx \frac{1}{2}\ L\sec\theta\ \tilde{\beta}(\theta,T)\ (\Delta\theta)^2. \tag{1.14}$$

This equation is analogous to Eq. (1.5), as desired. Thus, regardless of the overall step angle θ, the stiffness is an appropriate measure for the free energy required to bend the step.

1.2.2 Step Stiffness as Steps "Inertia" or "Diffusivity"

Although it is appealing and intuitive to view the step stiffness as a gauge for how easily steps thermodynamically fluctuate, there is another perspective that further accentuates its profound nature. From this perspective, the step is viewed as the path that a particle constrained to move in one dimension traces out through time. As we will now see, this powerful and beautiful analogy clarifies the role of step stiffness.

To exploit the analogy, we imagine the step fluctuates about the y-axis (or, equivalently, we orient our y-axis to be parallel to the average step orientation). With this done, we can describe the step position using a continuous function $x(y,t)$

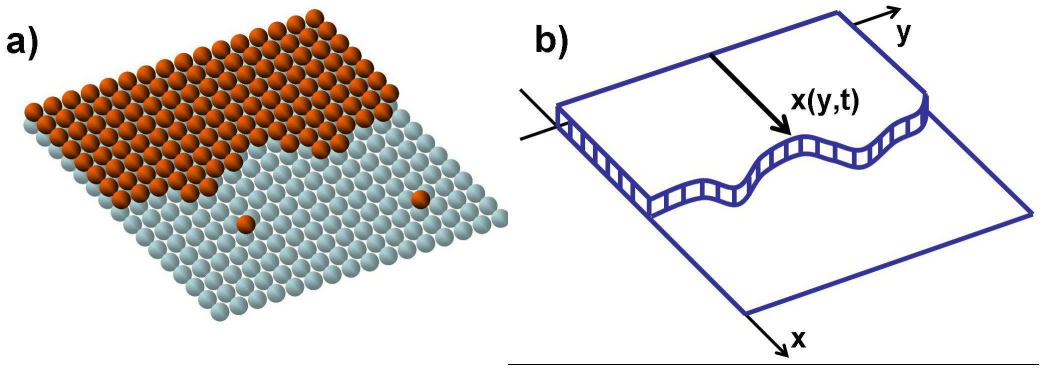

Figure 1.7: In (a), a portion of a step is shown, along with the constituent step-edge adatoms. In (b), the step is coarse-grained so it can be described by a continuous function x(y,t). Notice the terrace in (a) contains a couple adatoms, which we assume are in thermodynamic equilibrium with the step.

(Maryland notation). We illustrate such a step in Fig. 1.7 and show how it is coarse-grained. Our analogy begins to take shape by dividing Eq. (1.14) by the step length $L \sec\theta$. This gives the change in step free energy per unit length $\Delta\tilde{g}$:

$$\Delta\tilde{g} \equiv \frac{\Delta\tilde{G}}{L\sec\theta} \approx \frac{1}{2}\,\tilde{\beta}(\theta,T)\,(\Delta\theta)^2. \tag{1.15}$$

For small step fluctuations, $\Delta\theta \approx \partial x/\partial y$, so Eq. (1.15) becomes

$$\Delta\tilde{g} \approx \frac{1}{2}\,\tilde{\beta}(\theta,T)\,\left(\frac{\partial x}{\partial y}\right)^2. \tag{1.16}$$

This subtle change of variables allows us to compare $\Delta\tilde{g}$ to the energy of a particle of mass m traveling with velocity v. Specifically, by replacing y with time t in Eq. (1.16), so that $\partial x/\partial y$ is replaced by velocity $v \equiv \partial x/\partial t$, we have the energy $mv^2/2$, provided the stiffness is interpreted as mass. (In making this analogy, the time is fictitious, so there is really nothing "dynamical" going on with the step.) This means that the stiffness is the thermodynamic "inertia" of a step, in the sense that the step is analogous to the time-evolved path (world-line) of a particle constrained

to move in one dimension. As such, it plays a very important role in describing step motion, ultimately quantifying the step response to other steps, to atomistic mass-transport processes, and to external driving forces.

We can take this analogy even further by computing the average squared displacement of the step edge $C(y) = \langle [x(y) - x(0)]^2 \rangle$. Again, we imagine the step traces out the time-evolved path of a particle constrained to move in one-dimension, only now we imagine the movement is diffusive, so that $C(y)$ is analogous to the more familiar average distance squared $C(t)$ a one-dimensional random-walker travels:

$$C(t) = \langle [x(t) - x(0)]^2 \rangle = 2\tilde{D}t, \tag{1.17}$$

where $\tilde{D}$ is the diffusion coefficient (we use the tilde to remind us that the time is, again, fictitious). We wish to determine the proper combination of step parameters that is analogous to $\tilde{D}$. Our intuition suggests that stiffer steps correspond to the world lines of particles with smaller diffusion coefficients and vice versa. As we will now show, this turns out to be fundamentally correct.

To prove this intuitive result and facilitate the calculation of $C(y)$, we Fourier transform the step edge:

$$x(y) = \frac{1}{\sqrt{2\pi}} \int dq \; x_q \; e^{iqy}. \tag{1.18}$$

In this case, Eq. (1.16) becomes

$$\Delta\tilde{g} = \frac{1}{2\pi} \int dq \; \frac{1}{2} \; \tilde{\beta}(\theta, T) q^2 |x_q|^2. \tag{1.19}$$

Using the equipartition of energy theorem, we know each mode has $k_B T/2$ worth of

energy in equilibrium. We thus have

$$\langle |x_q|^2 \rangle = \frac{k_B T}{\tilde{\beta}(\theta, T) q^2}. \tag{1.20}$$

With this, we can determine $C(y)$:

$$\begin{aligned} C(y) &= \langle [x(y) - x(0)]^2 \rangle \\ &= \frac{1}{2\pi} \int dq \; dq' \langle x_q x_{q'} \rangle (e^{iqy} - 1)(e^{iq'y} - 1) \\ &= \frac{k_B T}{\tilde{\beta}(\theta, T)} |y|, \end{aligned} \tag{1.21}$$

where we have used Eq. (1.20) in a generalized form, namely,

$$\langle x_q x_{q'} \rangle = \frac{k_B T}{\tilde{\beta}(\theta, T) q^2} \; \delta(q + q'). \tag{1.22}$$

Comparing Eq. (1.21) to Eq. (1.17), we find the analogy we were looking for. Specifically,

$$\tilde{D} \sim \frac{1}{2} \frac{k_B T}{\tilde{\beta}(\theta, T)}. \tag{1.23}$$

As we expected, the stiffer the step, the smaller the diffusion coefficient. To avoid confusion, the combination of terms on the right hand side of Eq. (1.23) is usually written[11] in terms of the step diffusivity b^2. The term "diffusivity" brings to mind diffusion, but reminds us that the dynamics only correspond to the analogous, yet fictitious, one-dimensional random walker. Still, the analogy provides yet another perspective from which we clearly see the importance of step stiffness when quantifying step dynamics.

In short, the stiffness is the key thermodynamic parameter describing step movement and fluctuations. We can interpret its meaning in three ways, all useful

in their own right. In the first, we imagine a step bends or fluctuates about its equilibrium orientation by a small amount. In this case, the stiffness measures the thermodynamic ease of the fluctuations, regardless of whether they are about a close-packed orientation or some other orientation, as Eqs. (1.5) and (1.14) show. In the second and third interpretations, we envision a step as the path a particle constrained to move in one dimension traces out through time. If the path corresponds to that of a particle moving with velocity v, the stiffness corresponds to the particles mass or inertia. If, on the other hand, the path corresponds to a random-walker, then the stiffness corresponds to the inverse diffusion coefficient or more traditionally, the inverse diffusivity.

1.3 The Role of Step Stiffness in the Continuum Step Model

Having established an intuition for step stiffness and rigorously quantified its meaning from multiple perspectives, we now discuss its crucial role within the continuum step model,[5] where it serves as one of three key parameters. Remember this model describes surface evolution through the collective dynamics of constituent steps, assumed to be continuous. Before we can quantify the net step dynamics and have any hope of modeling the overall surface morphology, we must first quantify the fluctuations and movement of a single, isolated step. To do so, we will again imagine the step can be described by a continuous function $x(y,t)$, as in Fig. 1.7. Our goal is to quantify the step movement by calculating its velocity $\dot{x}(y,t) \equiv \partial x(y,t)/\partial t$.

Based on our newly developed intuition, it is not surprising that step stiffness

critically affects step velocity. In particular, there are three important domains[5,12–15] defining the movement of an isolated step based on the underlying adatom dynamics: attachment-detachment (AD), terrace-diffusion (TD), and periphery-diffusion (PD). The first two domains describe steps that fluctuate because they exchange adatoms with the terrace. In the AD regime, the adatoms diffuse relatively quickly on the terrace, making their attachment to and detachment from steps the bottleneck to net movement. In the TD regime, on the other hand, the diffusion along the terrace is relatively slow, making it the bottleneck to net step movement. In both cases, the step velocity is proportional to the step stiffness.[5,13,14]

In the PD regime, however, steps do not exchange adatoms with the terrace. Instead, steps fluctuate because adatoms diffuse along their periphery. In this regime, we assume the adatom attachment and detachment rates are negligible, so the step length is essentially conserved. The PD regime turns out to be especially important at lower temperatures, when adatoms no longer have enough thermal energy to detach from steps. For our purposes, this regime is most relevant because we are interested in the anisotropy of step stiffness, which becomes significant when the temperature is low. In the PD domain, the step velocity can be written

$$\dot{x}(y,t) = \frac{\partial}{\partial y}\left\{\frac{\Gamma(x')}{k_B T}\frac{\partial}{\partial y}\left[\tilde{\beta}(x')\ \mathcal{K}(x',t)\right]\right\} + \eta(y,t). \tag{1.24}$$

where $k_B T$ is the thermal energy, $\Gamma(x',T)$ is the adatom mobility along the step edge (which is anisotropic itself), $\mathcal{K}(x',t)$ is the step curvature, and $\eta(y,t)$ is correlated, conserved noise:

$$\langle \eta(y,t)\eta(y_0,t_0)\rangle = 2\Gamma\delta(t-t_0)\delta''(y-y_0). \tag{1.25}$$

In these equations and those that follow, we no longer explicitly show the temperature dependence. Furthermore, for notational convenience, we use a prime to denote differentiation with respect to y and occasionally suppress the θ dependence within the step slope $x'(y,t) = m \equiv \tan\theta$.

Eq. (1.24) is essentially the diffusion equation describing the random hops of adatoms along the step edge. To derive it, we let $ds \equiv \sqrt{1+(x')^2}\, dy$ be the differential distance along the step and $c(s,t)$ be the step-edge adatom concentration (number of adatoms per unit length). If we assume the adatom diffusion constant along the step edge $D_{PD}(s) = D_{PD}(x'(s))$ depends on the step slope x' at s, then the diffusion equation reads

$$\frac{\partial c(s,t)}{\partial t} = \frac{\partial}{\partial s}\left[D_{PD}(s)\frac{\partial c(s,t)}{\partial s}\right] \tag{1.26}$$

where the term in square brackets is just the net flux of adatoms at s. To convert the left-hand side of this equation to velocity, we multiply by the adatom area Ω. This gives

$$v_n(s,t) \equiv \frac{\partial\left[\Omega c(s,t)\right]}{\partial t} = \frac{\partial}{\partial s}\left\{D_{PD}(s)\frac{\partial\left[\Omega c(s,t)\right]}{\partial s}\right\} \tag{1.27}$$

where $v_n(s,t)$ is the normal step-edge velocity.

To proceed further, we utilize the Gibbs-Thompson relation to connect the adatom concentration with the thermodynamic step chemical potential $\mu(s,t)$ (the free energy required to add a step-edge adatom at position s):

$$c(s,t) = c_{eq}\; e^{\mu(s,t)/k_BT}, \tag{1.28}$$

where c_{eq} is the equilibrium adatom concentration. For small $\mu(s,t)/k_BT$, we can

rewrite Eq. (1.28) as

$$c(s,t) - c_{eq} \approx c_{eq}\ \frac{\mu(s,t)}{k_B T}. \tag{1.29}$$

This suggests we redefine the concentration so that it is measured from its equilibrium value $[c(s,t) - c_{eq} \to c(s,t)]$. Plugging this into Eq. (1.27) gives

$$v_n(s,t) = \Omega \frac{\partial}{\partial s}\left[c_{eq}\frac{D_{PD}(s)}{k_B T}\ \frac{\partial \mu(s,t)}{\partial s}\right]. \tag{1.30}$$

Thus, the step velocity is driven by gradients in the step chemical potential $\mu(s,t)$ along the step edge. If the change in the gradient of $\mu(s,t)$ along the step edge is large, then adatoms quickly moves down the gradient, causing the step to move quickly as well.

To arrive at Eq. (1.24), we need only connect $\mu(s,t)$ with $\tilde{\beta}(s)$. This can be done by writing both the total number of step adatoms N and the total step free energy F as functionals of $x(y,t)$:

$$N[x(y,t)] = \int \frac{x(y,t)}{\Omega}\ dy, \tag{1.31}$$

$$F[x(y,t)] = \int \beta(s)\ ds = \int \beta(x')\ \sqrt{1+(x')^2}\ dy. \tag{1.32}$$

With these functionals, we can express the step chemical potential as a functional derivative of F with respect to N:

$$\begin{aligned} \mu(x',t) = \frac{\delta F}{\delta N} &= \frac{\delta F[x(y,t)]}{\delta x}\frac{\delta x}{\delta N} \\ &= -\Omega\ \frac{d}{dy}\left\{\frac{\partial}{\partial x'}\left[\beta(x')\sqrt{1+(x')^2}\right]\right\}. \end{aligned} \tag{1.33}$$

The basic idea is straightforward: the addition of an adatom causes the step to lengthen and bend, which in turn costs free energy. As before, the step stiffness

turns out to be the central thermodynamic parameter defining the step movement. We make the connection concrete with the following simplifications:

$$\frac{d}{dy} = x'' \frac{\partial}{\partial x'}, \tag{1.34}$$

$$x' = \tan\theta \rightarrow \frac{\partial x'}{\partial \theta} = 1 + (x')^2, \tag{1.35}$$

$$\frac{\partial \beta(x')}{\partial x'} = \frac{\partial \beta(\theta)}{\partial \theta} \frac{1}{1 + (x')^2}. \tag{1.36}$$

With some algebra, this allows us to express the chemical potential as a function of θ:

$$\begin{aligned} \mu(\theta, t) &= \Omega \frac{-x''}{[1 + (x')^2]^{3/2}} \tilde{\beta}(\theta) \\ &= \Omega \mathcal{K}(\theta, t) \tilde{\beta}(\theta), \end{aligned} \tag{1.37}$$

where $\mathcal{K}(\theta, t)$ is the step curvature. Plugging this into Eq. (1.30) yields Eq. (1.24), provided two things: First, we define the adatom mobility to be $\Gamma(x') \equiv \Omega^2 D_{PD}(x') c_{eq}$, which is proportional to the adatom step-edge diffusion constant, as the name "mobility" would suggest. Second, we assume the temperature is low enough so that the step fluctuations are not too wild, implying x' is small and $ds \approx dy$.

By itself, Eq. (1.37) is significant. It says that the larger the step curvature and/or step stiffness, the larger the chemical potential. Since adatoms move from high to low chemical potential, we see that steps with large curvature quickly become flat, while steps with small stiffness (far from high-symmetry orientations) quickly move and readjust until they have larger stiffness.

Finally, it is worth mentioning that Eq. (1.24) is a fourth-order differential equation, which ultimately requires two derivatives of $\tilde{\beta}(\theta)$ with respect to θ. Thus,

the step velocity is extremely sensitive to the anisotropy of $\tilde{\beta}(\theta)$, which we already argued is extreme at lower temperatures. This is in contrast to the step mobility $\Gamma(\theta)$, which only requires one additional derivative with respect to θ. The sensitivity of step velocity to the anisotropy of step stiffness therefore requires an accurate formula for $\tilde{\beta}(\theta)$ in order to properly model step flow in the PD domain. Deriving such a formula will be the subject of the next two Chapters.

In summary, we have shown that the step stiffness plays a crucial role in describing step dynamics. Not only have we developed an intuition for step stiffness based on the fundamental step defects, kinks, but we have also rigorously defined its meaning. Briefly, step stiffness is a measure for how easily a step fluctuates. It is large and anisotropic at low temperatures (with high-symmetry steps being the stiffest), and it becomes smaller and more isotropic as the temperature approaches T_c, where it ultimately becomes negligible. In both the AD and TD domains, the velocity of a step edge is proportional to the step stiffness. In the PD domain, which is relevant at lower temperatures, however, two additional derivatives of the stiffness are required, making the velocity extremely sensitive to step orientation and stiffness anisotropy.

Chapter 2

Step Stiffness on {001} Surfaces

In this Chapter, we focus on deriving an analytic formula for the anisotropy of step stiffness on fcc {001} surfaces. We begin with a brief introduction to lattice-gas models, which will form the basis of our calculations, not only in this Chapter, but in Chapters 3 and 4 as well. We use such a model to derive a low-temperature formula for the step stiffness anisotropy assuming adatoms only interact with nearest-neighbors (NN). Although the formula is appealingly simple, comparisons with experiments on Cu(001) have shown it underestimates the stiffness by a factor of 4 in directions away from the close-packed directions. A subsequent estimate of the stiffness in the two high-symmetry directions alone suggested that inclusion of attractive next-nearest-neighbor (NNN) interactions could fully explain the discrepancy. To address this problem, we introduce the solid-on-solid (SOS) model to calculate the full anisotropy of step stiffness, as defined by Eq. (1.1), assuming adatoms interact with both NNs and NNNs. At low-temperatures, our result reduces to a simple, transparent expression. The effect of the strongest trio (three-site, nonpairwise) interaction can also be easily incorporated by modifying the interpretation of the two pairwise energies.

2.1 Ising Expansion on a Square Lattice

The orientation dependence of $\beta(\theta)$ and $\tilde{\beta}(\theta)$ on $\{001\}$ surfaces can be determined by first calculating the free energy $F(\theta)$ of a single step oriented at a fixed angle θ. Because of the four-fold symmetry of the surface, all calculations can be done in the first octant alone (from 0° to 45°, which is mirror-symmetric with the second octant, from 45° to 90°). To approximate $F(\theta)$, we perform a low-temperature Ising expansion of the partition function, as done by Rottman and Wortis.[16]

We begin by considering a step on a square lattice (representative of $\{001\}$ surfaces) with one end fixed to the origin and the other end, a distance L away, fixed to the point ($M \equiv L\cos\theta$, $N \equiv L\sin\theta$), as depicted in Fig. 2.1. We assume the constituent adatoms form a "lattice-gas," occupying only preferential, high-symmetry positions predefined by the crystal substrate. We furthermore assume the adatoms interact with one another by forming a finite number of "bonds" (such as NN, NNN, ...), the strength of which are fixed by the relative adatom positions. In Fig. 2.1, the single-layer island (or compact adatom-filled section) is in the lower region, separated by the step edge — which is drawn as a bold solid line — from the upper part of the figure, representing the "plain" region. Within such a lattice-gas framework, the energy of the step edge $\mathcal{E}_n$ is just the energy of the broken bonds required to form it. If we assume that adatoms only interact with NNs, then the sum of all the broken NN bonds (dotted lines in Fig. 2.1) is

$$\mathcal{E}_n = \varepsilon(M + N + 2n),\ n = 0, 1, 2, \ldots, \tag{2.1}$$

where ε, sometimes[17] called the "Ising parameter," is the bonding energy associated

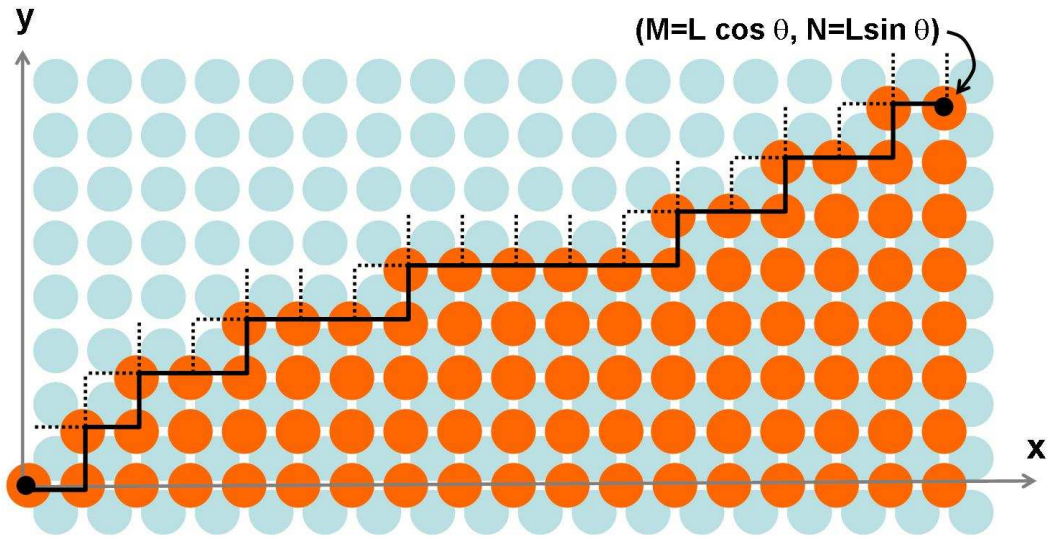

Figure 2.1: A step on a square lattice (fcc {001}) is shown from above, with the lighter blue spheres representing surface atoms, and the darker orange spheres representing adatoms. The step, shown as a thick, solid line, connects the origin with the point $(M = L\cos\theta, N = L\sin\theta)$. All $M+N$ broken NN bonds required to form the step are shown as dotted lines. Since this is the shortest possible step connecting the origin and (M, N), it contains only forced kinks and its energy is minimal: $\mathcal{E}_0 = \varepsilon(M+N)$. Other higher energy steps necessarily have thermal kinks, which increase the microscopic step length.

with the "severed half" of the NN lattice-gas bond: Since the NN lattice-gas energy ϵ_1 is attractive (negative), and half of it is attributed to the atom on each end, it "costs" a positive energy $\varepsilon = -\frac{1}{2}\epsilon_1$ for each step-edge atom. Because longer steps require more step-edge atoms, the step energy is only a function of the microscopic step length: $M+N+2n$ (this should not be confused with the macroscopic, experimentally measurable step length L). Thus, $\mathcal{E}_0$ corresponds to the shortest possible step, one with only forced kinks (geometrically required). Higher-energy steps necessarily have thermal kinks which require the addition of two more step-edge links – corresponding to one more step-edge atom – one going away from the fixed endpoint

and one going toward it. Because this corresponds to two more broken bonds, in general, $\mathcal{E}_{n+1} - \mathcal{E}_n \equiv \Delta\mathcal{E} = 2\varepsilon$. With these energies, we can write down the partition function Z_θ, assuming θ is fixed but L is large enough so that integer values of M and N can be found:

$$Z_\theta = g_{M,N}(0)e^{-\mathcal{E}_0/k_BT} + g_{M,N}(1)e^{-\mathcal{E}_1/k_BT} + ... \tag{2.2}$$

where k_BT is the thermal energy and $g_{M,N}(n)$ corresponds to the number of ways a step of length $M + N + 2n$ can be arranged between the two endpoints.

For low temperatures, only the first term in Eq. (2.2) need be considered (Appendix A provides the leading correction term, which gives a correction of order $\exp(-2\varepsilon/k_BT)$). To lowest order, then, $F = -k_BT \ln Z_\theta$ is

$$F \approx \mathcal{E}_0 - k_BT \ln \binom{M+N}{M}, \tag{2.3}$$

where we have inserted the value of $g_{M,N}(0)$ obtained from a simple combinatorial analysis.[16,18] After taking the thermodynamic limit (M, $N \gg 1$) and using Stirling's approximation, F becomes

$$F \approx \mathcal{E}_0 - k_BT \left[(M+N)\ln(M+N) - M\ln M - N\ln N\right]. \tag{2.4}$$

Remembering $M = L\cos\theta$, $N = L\sin\theta$, $\mathcal{E}_0 = \varepsilon(\cos\theta + \sin\theta)$, and dividing by the macroscopic step length L gives the low-temperature anisotropy of the line tension $\beta(\theta) = F/L$:

$$\begin{aligned} a_{||}\beta(\theta) &= \varepsilon(\cos\theta + \sin\theta) + k_BT\left[(\cos\theta + \sin\theta)\ln(\cos\theta + \sin\theta) - \right. \\ &\qquad \left. \cos\theta\ln(\cos\theta) - \sin\theta\ln(\sin\theta)\right], \end{aligned} \tag{2.5}$$

where $a_{||}$ is the NN distance. Using Eq. (1.1), we can now easily find the anisotropy of the low-temperature step stiffness $\tilde{\beta}(\theta)$:[19]

$$\frac{\tilde{\beta}(\theta)a_{||}}{k_BT} = \frac{2}{\sin(2\theta)\sqrt{1+\sin(2\theta)}}. \tag{2.6}$$

Here it is worth mentioning that the energetic portion $\mathcal{E}_0$ of the low-temperature line tension does not contribute to the stiffness because it is a linear combination of $\sin\theta$ and $\cos\theta$. As such, the addition of its second derivative with respect to θ cancels with itself. This turns out to be true regardless of the type of pairwise interactions included in the bond-counting model.[20] (Chapter 3 provides another example for fcc {111} surfaces.) Thus, in a very general sense, the low-temperature step stiffness is largely an entropic effect.

In a recent paper,[19] Eq. (2.6) was shown to underestimate the experimentally observed stiffness by a factor of 4 for steps oriented away from the close-packed direction. In that paper, the anisotropy of the stiffness was experimentally measured using two independent methods: direct measurement of the diffusivity on vicinal Cu surfaces with various tilts and examination of the shape of (single-layer) islands. The agreement of the two types of measurements assures that the underestimate is not an anomaly due to step-step interactions. In the same paper, the effect of next-nearest-neighbor (NNN) interactions ϵ_2 was crudely estimated by examining a general formula obtained by Akutsu and Akutsu,[21] showing a correction of order $\exp(-\epsilon_2/k_BT)$, which was glibly deemed to be insignificant. In subsequent work the Twente group[22] considered steps in just the two principal directions and showed that if one included an attractive NNN interaction, one could evaluate the step free

energies and obtain a ratio consistent with the experimental results. This group later extended their calculations[23] to examine the stiffness.

We address the discrepancy between experiment and theory in the next section, where our goal will be to compute the step line tension $\beta(\theta)$ and the stiffness $\tilde{\beta}(\theta)$ as functions of azimuthal misorientation θ, when NNN (in addition to NN) interactions contribute. Since it is difficult to generalize the low-temperature expansion of the Ising model,[16,24,25] we instead study the SOS (solid-on-solid) model, which behaves very similarly at low temperatures and at azimuthal misorientations that are not too large, but can be analyzed exactly even with NNN interactions. This derivation is described in Section 2.2, with most of the calculational details placed in Appendix A. In Section 2.3 we derive a simple expression for the stiffness in the low-temperature limit, presented in Eq. (2.20). We also make contact with parameters relevant to Cu(001), for which this limit is appropriate. In Section 2.4 we extend the formalism to encompass the presumably-strongest trio (3-atom, non-pairwise) interaction, showing that its effect can be taken into account by shifting the pair energies in the preceding work. The final section offers discussion and conclusions.

2.2 NNN SOS Model on a Square Lattice

Including NNN interactions in the low-temperature expansion of the square-lattice Ising model lifts the remarkable degeneracy of the model with just NN bonds. In that simple case, as we saw earlier, the energy of a path depends solely on

the number of NN links, independent of the arrangement of kinks along it; thus, the energy $\mathcal{E}_0$ of the ground state is proportional to the number of NN links of the shortest path between two points, and the entropy is related to the number of combinations of horizontal and vertical links that can connect the points.[16,18] Including NNN interactions causes the step energy to become a function of both the length of the step and the number of its kinks, eliminating the simple path-counting result.[18] It can then become energetically favorable for the step to lengthen rather than add another kink. This causes the NN energy levels to split in a non-trivial way, making it possible for a longer step to have a lower energy than a shorter step. A related complication is that the expansion itself depends on the relative strength of the NNN-interaction: Instead of an expansion just in terms of $\exp(-|\epsilon_1|/k_BT)$, the expansion also is in terms of $\exp(\epsilon_2/2k_BT)$. Hence, to take the NNN-expansion to the same order of magnitude as the NN-expansion, an unspecified number of terms is required, depending on the size of the ratio ϵ_2/ϵ_1.

Since the NNN Ising model cannot be solved exactly and we cannot generalize the low-T expansion, we turn to an SOS model, which was used in earlier examinations of step problems, most notably in the seminal work of Burton, Cabrera, and Frank,[26] and later used for steps of arbitrary orientation by Leamy, Gilmer, and Jackson.[8] It was also applied to an interface of arbitrary orientation in a square-lattice Ising model.[27]

Although the SOS model can be treated exactly, the result is somewhat unwieldy. Fortunately, at low temperature—the appropriate regime for the experiments under consideration—the solution reduces to a simple expression.

2.2.1 Description of Model

Consider a step edge of projected length L separating an upper adatom-free region from a lower adatom-filled region (see Fig. 2.2). The step edge is completely described by specifying its height y_i at position i $(0 \leq i \leq L)$. The energy of the step edge depends on the number of broken bonds required to form it. Let V and H represent the vertical and horizontal NN bond strengths divided by k_BT, and let U and D represent up-diagonal and down-diagonal NNN bond strengths over k_BT. Then the step-edge energy $E \equiv E(\{\Delta_i\})$ depends only on $\Delta_i \equiv y_i - y_{i-1}$.

For clarity, we consider two examples. First, if $\Delta_i = 2$ (as is the case between columns a and b in Fig. 2.2), then between positions i and $i+1$ there are 2 broken H-links, 1 broken U-links, and 3 broken D-links. There are also 2 broken V-links, but

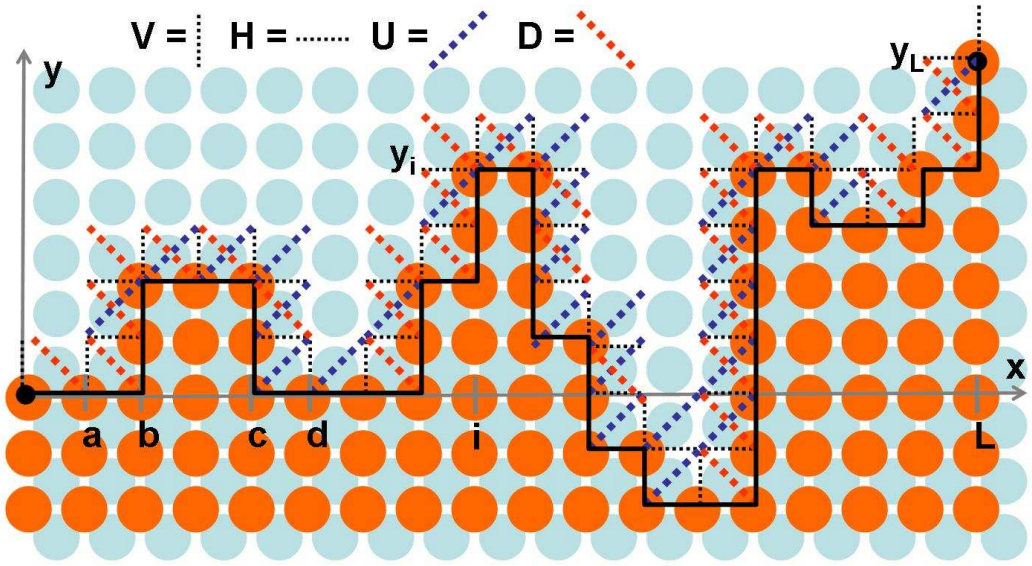

Figure 2.2: A finite-sized step edge whose projected length is L. The step has height y_i at position i $(0 \leq i \leq L)$. The height difference $y_L - y_0$ is fixed; thus, the step edge makes an angle θ with the horizontal axis, and has an overall slope m. The energy of the step edge is found by counting the number of broken links required to form it. Here all NN and NNN broken links are shown.

this number is independent of Δ_i, since every step-edge configuration of projected length L requires exactly L broken V-links. Similarly, if $\Delta_i = -2$ (as is the case between columns c and d in Fig. 2.2), then there would be the same number of broken H-links, but there would now be 3 broken U-links and 1 broken D-links (that is, the number of broken U and D links switch from the previous case). From these examples we see that, in general, there are $|\Delta_i|$ broken H-links, $|\Delta_i - 1|$ broken U-links, and $|\Delta_i + 1|$ broken D-links. It therefore follows that the step-edge energy is

$$\begin{aligned} \frac{E(\{\Delta_i\})}{k_B T} &= \sum_{i=1}^{L} \Big(V + H\,|\Delta_i| + U\,|\Delta_i - 1| + D\,|\Delta_i + 1| \Big) \\ &\equiv \sum_{i=1}^{L} K(\Delta_i). \end{aligned} \tag{2.7}$$

Because we seek the orientation dependence of β and $\tilde{\beta}$, we constrain the step to have an overall offset $Y \equiv y_L - y_0 \equiv L \tan\theta = \sum_{i=1}^{L} \Delta_i$. (Equivalently, we specify that the overall slope of the step is $m \equiv \tan\theta$.) The constrained partition function is therefore

$$Z\,(Y) \equiv \sum_{\{\Delta\}} \delta \left[Y - \sum_{i=1}^{L} \Delta_i \right] e^{-E(\{\Delta_i\})/k_B T}, \tag{2.8}$$

where $\{\Delta\}$ is the set of all Δ_i each of which ranges over all integers. From $Z(Y)$ we can find the orientation dependence of the free energy $F(Y) = -k_B T \ln Z(Y)$, the *projected* free energy per length $f(m) = F(Y)/L$, and the line tension (or free energy per length) $\beta(\theta) = f(m)\cos\theta$ (since the step length is $L/\cos\theta$); thence, we can find the stiffness $\tilde{\beta}(\theta) = \beta(\theta) + \partial^2\beta(\theta)/\partial\theta^2$.

For future reference, note that the process of extracting an atom from the

step-edge and replacing it alongside the edge, creates two pairs of $\Delta = +1$ and $\Delta = -1$, costing $4H$ according to Eq. (2.7) and removing a net of 2 NN bonds, so that $H = -\epsilon_1/2k_BT = \varepsilon_k/k_BT$. Similarly, we compare the energies of two NN atoms, abutting [the lower side of] a step edge ($\{\Delta_i\} = 0$) at i_0 and either parallel or perpendicular to the edge. In the first case, $\Delta_{i_0} = +1$ and $\Delta_{i_0+2} = -1$, with an added energy of $2H + 2(U+D)$ according to Eq. (2.7). In the perpendicular case $\Delta_{i_0} = +2$ and $\Delta_{i_0+1} = -2$, implying an added energy of $4H + 4(U+D)$. Counting bonds we see that the parallel configuration has one more ϵ_1 bond and two more ϵ_2 bonds than the perpendicular configuration. Invoking $H = -\epsilon_1/2k_BT$, we see that $U+D = -\epsilon_2/k_BT$; if $U = D$, then $D = -\epsilon_2/2k_BT$. The factor-of-2 difference between broken links in Eq. (2.7) and broken bonds was noted (for H links) already in the classic exposition by Leamy et al.[8] An alternate argument, presented over a decade ago,[28] for this factor of 2 is that the ragged edge is created by severing bonds along the selected path through an infinite square. This leads to the formation of two complementary irregular boundary layers (with opposite values of $\{\Delta_i\}$, so that the associated energy of each is half that of the broken bonds (at least when $U = D$).

2.2.2 Evaluation of the Free Energy

As detailed in the first part of the Appendix A, the sum in the Fourier transform of $Z(Y)$, which we denote by $W(\mu)$, factorizes. Thus, it can be written as

$$W(\mu) = \exp\left[-Lg(i\mu)/k_BT\right],$$

where $g(i\mu)$ is the reduced Andreev[10] free energy per column. To evaluate the inverse transform, we exploit the saddle point method and obtain (see Appendix A for details)

$$Z(Y) \approx \exp\left[-L\left(\rho_0 \tan\theta + \frac{g(\rho_0)}{k_B T}\right)\right], \tag{2.9}$$

where the saddle point ($\mu_0 = -i\rho_0$) is defined implicitly by the stationarity condition

$$-\frac{g'(\rho_0)}{k_B T} = m \equiv \tan\theta. \tag{2.10}$$

Here, prime (as in g') denotes a derivative with respect to ρ. This result can be regarded as applying a "torque" to the step to produce a rotation $\theta = \tan^{-1} m$ from the minimum-energy, close-packed orientation.[8]

Taking the logarithm of Eq. (2.9), we find the projected free energy per column $f(m)$ as a Legendre transform of the reduced Andreev[10] free energy per column $g(\rho_0)$:

$$\frac{f(m)}{k_B T} \approx \rho_0 m + \frac{g(\rho_0)}{k_B T}. \tag{2.11}$$

Note that this expression is valid only for $L \gg 1$; for finite-sized systems, corrections are required. As standard for Legendre transforms,[29] we have

$$\frac{\ddot{f}(m)}{k_B T} = -\frac{k_B T}{g''(\rho_0)}, \tag{2.12}$$

where $\ddot{f} \equiv \partial^2 f/\partial m^2$. Using $\beta(\theta)a = f(m)\cos\theta$ and $m = \tan\theta$, with a the lattice constant of the square (i.e., the column spacing, which is $(1/\sqrt{2})$ the conventional fcc lattice constant), we can rewrite the stiffness as

$$\tilde{\beta}(\theta)a = \ddot{f}(m)/\cos^3\theta, \tag{2.13}$$

or, similar to results by Bartelt *et al.*,[30]

$$\frac{k_B T}{\tilde{\beta}(\theta) a} = -\frac{g''(\rho_0)}{k_B T} \cos^3 \theta. \tag{2.14}$$

Thus, we only need $g''(\rho)$ to find the stiffness as a function of m or θ.

Of course, ρ_0 in g'' must be eliminated in favor of m via Eq. (2.10). The details for the general case are somewhat involved. Here, we simplify to the physically relevant case of $U = D$ and, defining $S \equiv H + U + D = H + 2D$, just quote the results:

$$\frac{g''(\rho_0)}{k_B T} = -m \left[\frac{2 \sinh \rho_0}{C(S, \rho_0)} + \coth \rho_0 \right] + m^2 \tag{2.15}$$

where $C(S, \rho_0) \equiv \cosh S - \cosh \rho_0$ and $\rho_0(m)$ is found by inverting

$$m = \frac{\sinh \rho_0 \sinh S}{C(S, \rho_0) \left[\sinh S - C(S, \rho_0) \left(1 - e^{-2D} \right) \right]}. \tag{2.16}$$

Some details can be found in the Appendix A. Since Eq. (2.16) is a quartic equation for $\cosh \rho_0$ or e^{ρ_0}, the explicit expression for $\rho_0(m)$ is rather opaque. However, at low-temperatures, a simpler formula emerges, as shown in the next section.

2.3 Low-T Solution: Simple Expression

At low temperatures, we find that the appropriate root for ρ_0 diverges. Then we can write $\cosh \rho_0 \approx \sinh \rho_0 \approx e^{\rho_0}/2$. Of course, $H \propto 1/T$ so that $\cosh S \approx e^S/2$. With these approximations, Eq. (2.16) becomes quadratic in e^{ρ_0}:

$$m = \frac{e^{\rho_0 + S}}{(e^S - e^{\rho_0})[e^S - (e^S - e^{\rho_0})(1 - e^{-2D})]} \tag{2.17}$$

Likewise, the expression for $g''(\rho_0)$, Eq. (2.15), becomes

$$\frac{g''(\rho_0)}{k_B T} = -m \left[\frac{2 e^{\rho_0}}{(e^S - e^{\rho_0})} + 1 \right] + m^2. \tag{2.18}$$

Solving for e^{ρ_0} in Eq. (2.17) and inserting the solution into Eq. (2.18) gives

$$\frac{g''(\rho_0)}{k_B T} = -m\sqrt{(1-m)^2 + 4me^{-2D}}. \tag{2.19}$$

so that, from Eq. (2.14), and recalling $D = -\epsilon_2/2k_BT$, we arrive at our *main result*, a simple, algebraic expression for $\tilde{\beta}$ as a function of m:

$$\frac{k_BT}{\tilde{\beta}a} = \frac{m\sqrt{(1-m)^2 + 4me^{\epsilon_2/k_BT}}}{(1+m^2)^{3/2}} \tag{2.20}$$

$$= \frac{\sin(2\theta)\sqrt{1-(1-2e^{\epsilon_2})\sin(2\theta)}}{2}. \tag{2.21}$$

We examine Eq. (2.20) in several different limiting cases. When $\epsilon_2 = 0$, this reduces to

$$\frac{k_BT}{\tilde{\beta}a} = \frac{m+m^2}{(1+m^2)^{3/2}}, \tag{2.22}$$

$$= \frac{\sin(2\theta)\sqrt{1+\sin(2\theta)}}{2}, \tag{2.23}$$

as in Eq. (2.6), when we solved for the stiffness assuming only NN interactions are relevant. Interestingly, at $\theta = 45°$, Eq. (2.20) shows a simple dependence on ϵ_2, namely,

$$\frac{k_BT}{\tilde{\beta}a} = \frac{e^{\epsilon_2/2k_BT}}{\sqrt{2}}. \tag{2.24}$$

Of course, this reduces to the venerable Ising result of $1/\sqrt{2}$ in the absence of NNN interactions ($\epsilon_2 = 0$).[16,17,31]

By considering just the lowest and second lowest energy configurations,[22,23] Zandvliet et al. obtained the result[23] (expressed with our sign convention for ϵ_2) for the maximally misoriented case $m = 1$

$$\frac{k_B T}{\tilde{\beta} a} = \frac{\sqrt{2}}{1 + e^{-\epsilon_2/2k_B T}}, \tag{2.25}$$

which has, for the attractive ϵ_2 of primary concern here, some qualitative similarities to Eq. (2.24) (including the value $1/\sqrt{2}$ for $\epsilon_2 = 0$) but is too small by a factor of 2 for $\epsilon_2/2k_BT \ll 0$; even the coefficient of the first-order term in an expansion in $\epsilon_2/2k_BT$ is half the correct value. For the opposite limit of repulsive ϵ_2, Eq. (2.25) levels off (at $\sqrt{2}$), in qualitative disagreement with the actual exponential increase seen in Eq. (2.24).

Fig. 2.3 compares Eq. (2.20) to corresponding exact solutions [found by numerically solving Eqs. (2.14), (2.15), and (2.16)] at several temperatures when $\epsilon_2 = \epsilon_1/10$. We see that Eq. (2.20) overlaps the exact solution at temperatures as high as $T_c/6$. As the temperature increases, the stiffness becomes more isotropic, and Eq. (2.20) begins to overestimate the stiffness near $\theta = 0°$.

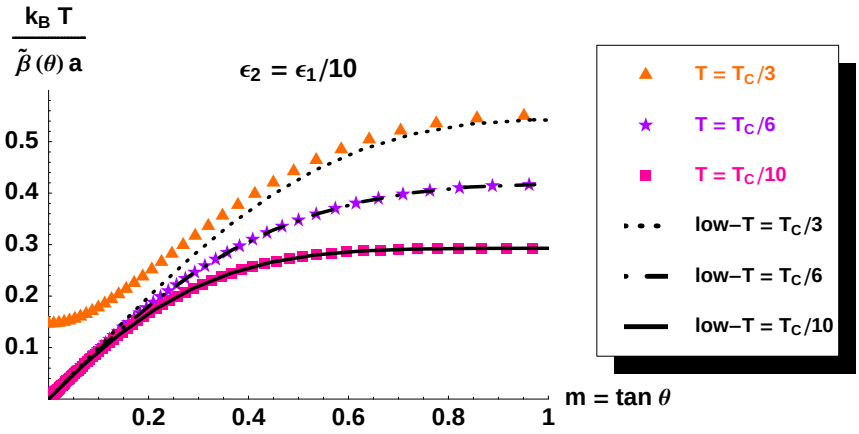

Figure 2.3: The range of validity of Eq. (2.20) is examined by comparing it to exact numerical solutions of the SOS model at several temperatures. In the legend T_c refers to the NN lattice-gas (Ising) model; for $|\epsilon_1| = 256$meV, $T_c = 1685$K.

Finally, in Fig. 2.4 (using the experimental value[32] $\varepsilon_k = 128$ meV $\Rightarrow \epsilon_1 = -256$ meV), we compare Eq. (2.20) to the NN-Ising model at $T = 320$K, as well as to the experimental results of Dieluweit et al.[19] For strongly attractive (negative) ϵ_2, $k_BT/\tilde{\beta}a$ decreases significantly. In fact, when ϵ_2/ϵ_1 is 1/6, so that $-\epsilon_2/2k_BT = (\epsilon_2/\epsilon_1)(\varepsilon_k/k_BT) \approx (1/6)4.64$, the model-predicted value of $k_BT/\tilde{\beta}a$ has decreased to less than half its $\epsilon_2 = 0$ value (viz. by a factor of 0.46, vs. 0.63 if Eq. (2.25) is used), so about 3/2 the experimental ratio. If ϵ_2/ϵ_1 increases even further, $k_BT/\tilde{\beta}a$ further decreases and develops positive curvature, causing an endpoint local minimum to appear at $\theta = 45°$. We can determine when this occurs by expanding Eq. (2.20)

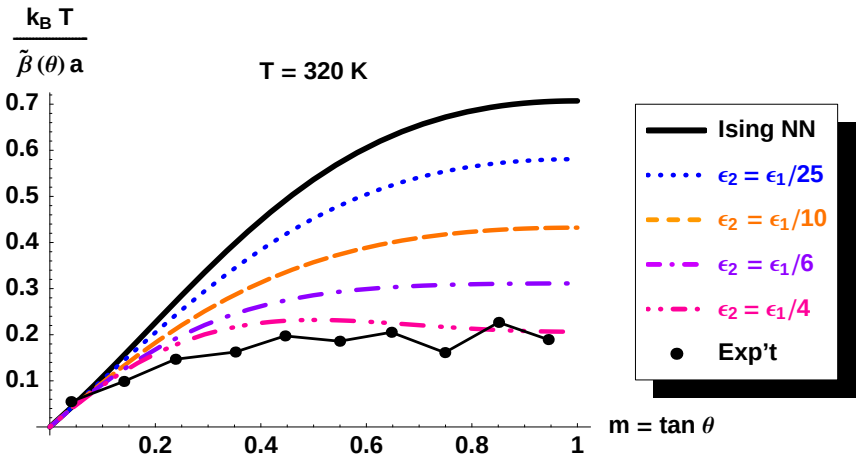

Figure 2.4: Eq. (2.20) is plotted for a variety of different values of $D = -\epsilon_2/2k_BT$, where ϵ_1 and ϵ_2 are NN- and NNN-interaction energies, respectively, in a lattice-gas picture. The solid curve denoted "Ising NN" corresponds to $\epsilon_2 = 0$. The dots labeled "Exp't" are taken from Fig. 2 of the paper by Dieluweit et al.[19] and were derived from the equilibrium shape of islands on Cu(001) at 302K, with the line segments serving as guides for the eye. To minimize clutter, we omit similar data derived from correlation functions of vicinal surfaces at various temperatures. Note that for $\epsilon_2 = \epsilon_1/4$ a maximum has developed near $\tan\theta = 1/2$ that is not evident in the experimental data.

about $m = 1$:

$$\frac{k_B T}{\tilde{\beta} a} = \frac{e^{-D}}{\sqrt{2}} + \left(\frac{e^{D}}{8\sqrt{2}} - \frac{3e^{-D}}{4\sqrt{2}} \right) (m-1)^2 + \ldots \tag{2.26}$$

Setting the coefficient of $(m-1)^2$ to zero gives $-2D = \epsilon_2/k_B T = -\ln(6) \approx -1.8$, which corresponds to a value of $k_B T/\tilde{\beta} a = \sqrt{3}/6 \approx 0.29$, about 2/5 the value at $\epsilon_2 = 0$. For $T = 320$K and $\varepsilon_k = 128$ meV, this corresponds to $\epsilon_2/\epsilon_1 \approx 0.2$. However, for the NNN interaction alone to account for the factor-of-4 discrepancy between model/theory and experiment reported by Dieluweit et al.[19], Fig. 2.4 shows that $\epsilon_2/\epsilon_1 \approx 0.3$ would be required.

2.4 Effect of Trio Interactions

In addition to the NNN interaction, trio (3-atom, non-pairwise) interactions may well influence the stiffness. The strongest such interaction is most likely that associated with 3 atoms forming a right isosceles triangle, whose sides are at NN distance and hypotenuse at NNN separation. In a lattice gas model, there is a new term with ϵ_{RT} times the occupation numbers of the 3 sites.[33] Note that this trio interaction energy ϵ_{RT} is in addition to the contribution $2\epsilon_1 + \epsilon_2$ of the constituent pair interactions. If we count broken trios and weight each by R, we find an additional contribution to Eq. (2.7) of R times

$$4|\Delta_i| + 2\delta_{\Delta_i,0} + 2 = 2|\Delta_i| + |\Delta_i + 1| + |\Delta_i - 1| + 2, \tag{2.27}$$

where we have converted the Kronecker delta at $i = 0$ to make better contact with Eq. (2.7). Thus, without further calculation we can include the effect of this trio by replacing H by $H + 2R$, U by $U + R$, D by $D + R$, and (trivially) V by $V + 2$.

By arguments used at the end of Section IIA, we recognize $R = -\frac{1}{2}\epsilon_{RT}$. Consequently, the effective NN lattice-gas energy is $\epsilon_1 + 2\epsilon_{RT}$ and, more significantly the effective NNN interaction energy is $\epsilon_2 + \epsilon_{RT}$. Thus, ϵ_{RT} must be attractive (negative) if it is to help account for the discrepancy between the model and experiment in Fig. 2 of the paper by Dieluweit et al.[19] Furthermore, by revisiting the configurations discussed in the penultimate paragraph of the Introduction, we find that the kink energy ε_k becomes $-\frac{1}{2}\epsilon_1 - \epsilon_{RT}$. Thus, for a repulsive ϵ_{RT}, $|\epsilon_1|$ will be larger than predicted by an analysis of, e.g., step-edge diffusivity that neglects ϵ_{RT}. Lastly, the close-packed edge energy, i.e. the $T = 0$ line tension $\beta(0) = -\frac{1}{2}\epsilon_1 - \epsilon_2$, becomes $-\frac{1}{2}\epsilon_1 - \epsilon_2 - 2\epsilon_{RT}$

2.5 Discussion and Conclusions

We now turn to experimental information about the interactions, followed by comments on the limited available calculations of them, often recapitulating the discussion by the Twente group.[22] All the experiments are predicated on the belief that at 320K there is sufficient mobility to allow equilibrium to be achieved. If the NNN interactions are to explain at least partially the high stiffness of experiment compared to Ising theory, the NNN interaction must be attractive and a substantial fraction of ϵ_1. Since compact islands do form on the Cu(001) surface, it is obvious that ϵ_1 is attractive. If ϵ_2 is also attractive, as required for reduction of the overestimate of $k_B T/\tilde{\beta}$, then the low-temperature equilibrium shape has clipped corners (octagonal-like, with sides of alternating lengths), as noted by the Twente group.[22]

No evidence of such behavior has been seen. The lack of evidence of a decreasing stiffness near $\theta \approx 45^\circ$ suggests that ϵ_2/ϵ_1 is at most 1/5.

There is implicit experimental information for ϵ_2: from island shapes[17] and fluctuations[34] $\beta(0) = 220 \pm 11$ meV. Since related measurements showed $\frac{1}{2}\epsilon_1 = -128$meV, we deduce $\epsilon_2 = -92$ meV if ϵ_{RT} is insignificant. These values imply that ϵ_2/ϵ_1 is somewhat larger than 1/3, which seems unlikely in light of the unobserved predictions about the shape of islands in that case (cf. the end of Section 2.3).

To corroborate this picture, one should estimate the values of ϵ_1 and ϵ_2, as well as ϵ_{RT}, from first-principles total-energy calculations. In contrast to Cu(111),[35,36] however, no such information even for ϵ_1 has been published for Cu(001); there are, however, several semiempirical calculations which found $\varepsilon_k \approx 0.14$eV.[37] To address this shortcoming, we have carried out calculations[38] of the relevant pairwise and multi-atom interactions on Cu(001) using the VASP package,[39–42] as detailed in Chapter 4. Our calculations suggest that ϵ_2 is indeed attractive, and that ϵ_2/ϵ_1 is about 1/8.

In calculations based on the embedded atom method (EAM), which work best for late transition and noble fcc metals, the indirect ("through-substrate") interactions are expected to be strong only when the adatoms share common substrate nearest neighbors; then the interaction should be repulsive and proportional to the number of shared substrate atoms.[43] If the NN and NNN interactions on Cu(001) were purely indirect ("through-substrate"), we would then predict $\epsilon_2 = \frac{1}{2}\epsilon_1 > 0$. However, whenever direct interactions (due to covalent effects between the nearby adatoms)

are important, they overwhelm the indirect interaction. Our calculations in Chapter 4, which find both ϵ_1 and ϵ_2 attractive (negative), therefore suggest that direct interactions are significant at both NN and NNN separations on Cu(001).

It is also not obvious *a priori* whether multi-atom interactions also contribute significantly. In EAM calculations, longer range pair interactions and multisite non-pairwise interactions are generally very-to-negligibly small. [For homoepitaxy, the only semiempirical result is that they are insignificant for Ag on Ag(001).[44]] Still, such calculations probably underestimate the actual values of these interactions since there is no Fermi surface in this picture, and it is the Fermi wavevector that dominates long-range interactions. Indeed, our calculations in Chapter 4 indicate a *repulsive* right-triangle trio interaction ϵ_{RT} with sizable magnitude (perhaps comparable to $|\epsilon_2|$, consistent with *a priori* expectations.[43,45,46]) However, as we discussed at the end of section 2.4, such a repulsive interaction would diminish rather than enhance the effect of ϵ_2, increasing the discrepancy between experimental step stiffness and theory. As we will discuss in Chapter 4, we believe the introduction of a quarto (4 atom, non-pairwise) interaction can alleviate the discrepancy.

In summary, NNN interactions may well account for a significant fraction, perhaps even a majority, of the discrepancy between NN Ising model calculations and experimental measurements of the orientation dependence of the reduced stiffness;[19] the effect is even somewhat greater than estimated by the Twente group.[22,23] However, inclusion of ϵ_2 is not the whole answer, nor, seemingly, is consideration of ϵ_{RT}. One possible missing ingredient is other multi-site interactions, most notably the quarto interaction mentioned above and discussed in detail in Chapter

4. Since direct interactions are probably important, there is no way to escape doing a first-principles computation; we continue to use the VASP package to extend our preliminary calculations detailed in Chapter 4.[47] A more daunting (at least for lattice-gas aficionados) possibility is that long-range intrastep elastic effects may be important. Ciobanu and Shenoy have made noteworthy progress in understanding how this interaction contributes to the orientation-dependence of noble-metal steps.[48]

Chapter 3

Step Stiffness on {111} Surfaces

Just as we derived a low-temperature formula for the anisotropy of step stiffness on fcc {001} surfaces in Chapter 2, here we derive an analogous formula for fcc {111}. Specifically, we seek formulas for $\beta(\theta)$ and thence $\tilde{\beta}(\theta) \equiv \beta(\theta) + \beta''(\theta)$ as functions of the azimuthal misorientation θ, assuming just nearest-neighbor (NN) interactions in plane and an underlying {111} surface. Such surfaces are characterized by a six-fold symmetric triangular (hexagonal) lattice, allowing all calculations to be done in the first sextant alone (from 0° to 60°). In contrast to $\beta(\theta)$, we shall find that at low T, $\tilde{\beta}(\theta)$ is insensitive, under plausible assumptions, to the symmetry-breaking by the second substrate layer, so that plots from 0° to 30° suffice. Although an analytic solution exists for the orientation dependence of the NN line tension on a square lattice,[16,24,49] only an implicit solution to a 6^{th}-order equation has been found for a hexagonal lattice.[50] This makes comparisons to experiment rather arduous, particularly when trying to compare data on $\tilde{\beta}(\theta)$, which is related to $\beta(\theta)$ through a double derivative with respect to θ. Fortunately, we will see that a remarkably simple formula exists for the orientation dependence of $\tilde{\beta}$ at temperatures which are low compared to the characteristic energy of step fluctuations (i.e. the kink energy or the energy per length along the step). For noble metals, room temperature lies in this limit, facilitating direct comparisons to experiment.

This work is motivated by results from Chapter 2, where we found that the square-lattice NN Ising model underestimates $\tilde{\beta}$ by a factor of 4 away from close-packed directions on Cu{001}. We also showed that much (but not all) of this discrepancy could be understood by considering the addition of next-nearest-neighbor (NNN) interactions. For the triangular lattice, we will see that such a longer-range interaction is not required to describe the orientation dependence of $\tilde{\beta}$.

In the following section, we characterize steps on a hexagonal lattice and perform a low-temperature expansion of the lattice-gas partition function, assuming only NN bonds are relevant, and derive both $\beta(\theta)$ and $\tilde{\beta}(\theta)$. We obtain a remarkably simple expression for the latter in Eq. (3.14). Since this low-T limit is determined by geometric/configurational considerations, it becomes problematic near close-packed orientations ($\theta = 0°$), where the kinks must be thermally activated. Therefore, we make use of exact results to assess in several ways how small θ can be before the simple expression becomes unreliable. In Section 3.2, we present three general results for island stiffness that are valid in the experimentally-relevant low-T limit when configurational considerations dominate the thermodynamics. We show that the line tension cannot be [re]generated from the stiffness and that the stiffness can have full 6-fold symmetry even though the substrate and the line tension have just 3-fold symmetry. Accounting for such 3-fold symmetry with a lattice-gas model on a hexagonal grid requires an extension from the conventional parameterization; we posit an *orientation-dependent* interaction between 3 atoms at the apexes of an equilateral triangle with NN legs. In Section 3.3, we compare our results to experiments on Ag and Cu{111} surfaces, showing that Eq. (3.14) provides a good

approximation and, thus, that NNN interactions are much less important than on Cu{001}. Next, in section 3.4, we extend our analysis to Ag(111) steps decorated by C_{60}. To compare with experiment, we derive an expression for the anisotropy of the decorated step line tension. We use this formula to predict that the attractive interaction between Ag and C_{60} is around -126 meV per molecule. We also study the decorated island perimeter fluctuations. In the process we show that the NN attractive interaction between two C_{60} molecules is roughly -87 meV. To our knowledge, these are the first experimental estimates of their kind. The final section offers a concluding discussion. Three appendices (B.1 - B.3) give detailed calculations of the leading correction of the low-T expansion, of explicit analytic and numerical results based on Zia's exact implicit solution,[50] and of Eq. (3.14) as the low-T limit of Zia's solution.

3.1 Ising Expansion on a Triangular Lattice

3.1.1 Triangular Lattice Step Energy

As in Chapter 2, we begin by doing a low-temperature Ising expansion of the partition function. To make this calculation symmetric with the last, we introduce a linear operator $\mathcal{L}$ that transforms the coordinates of a point on a square lattice (M,N) to those on a triangular lattice (M',N'); cf. Fig. 3.1b. This operator finds the position of a point in a coordinate system whose positive y-axis is bent at 60°

with respect to the positive x-axis:

$$\begin{pmatrix} M' \\ N' \end{pmatrix} = \mathcal{L} \begin{pmatrix} M \\ N \end{pmatrix} = \begin{pmatrix} 1 & -1/\sqrt{3} \\ 0 & 2/\sqrt{3} \end{pmatrix} \begin{pmatrix} M \\ N \end{pmatrix}. \tag{3.1}$$

With the aid of $\mathcal{L}$, we can see how $\mathcal{E}_0$ changes on a triangular lattice. To begin, we imagine a step in the first sextant (from 0° to 60° degrees in the plane) starting at (0,0) and ending at (M', N'). Such a step is shown in Fig. 3.1b. As before, the bold solid line represents the step edge with the bottom region a layer higher than the top (or, alternatively phrased, it separates the upper, adatom-free region from the lower, adatom-filled region). The broken bonds required to form the step will have only three orientations: 0°, 60°, and 120°. If we consider the shortest step between the two points (corresponding to energy $\mathcal{E}_0$), then there will be exactly $M' + N'$ broken bonds oriented at 0° and 60° (these bonds are analogous to those oriented at 0° and 90° on a square lattice). There will be another $M' + N'$

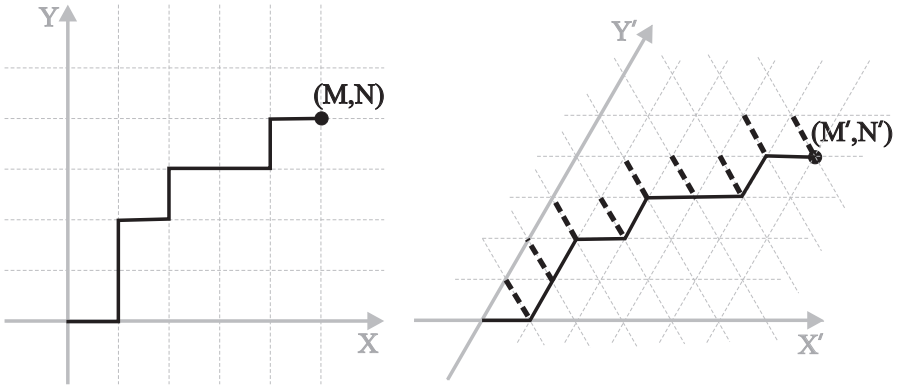

Figure 3.1: There is a one-to-one correspondence between the shortest-distance steps connecting points on a square lattice [(a), left panel] and the shortest distance steps connecting points on a triangular lattice [(b), right panel]. This figure shows two corresponding steps. Analogous to the $M + N$ broken bonds oriented at 0° and 90° on a square lattice, there are $M' + N'$ broken bonds oriented at 0° and at 60° on a triangular lattice. However, there are another $M' + N'$ broken bonds oriented at 120° on a triangular lattice.

broken bonds oriented at 120° (drawn as bold, dashed lines in Fig. 3.1). In total, there will be $2(M'+N')$ broken bonds. Since ε is the energy of these severed bonds, $\mathcal{E}_0^{\triangle} = 2\varepsilon(M'+N')$. Thus, the energy is proportional to the step length, as was the case on a square lattice. Using $\mathcal{L}$ to write M' and N' in terms of M and N gives

$$\mathcal{E}_0^{\triangle} = 2\varepsilon\left(M + \frac{N}{\sqrt{3}}\right) = 2\varepsilon L\left(\cos\theta + \frac{\sin\theta}{\sqrt{3}}\right). \tag{3.2}$$

3.1.2 Triangular Lattice Step Degeneracy

Next we consider the degeneracy factors $g^{\triangle}(n)$ on a triangular lattice. For the ground state $g^{\triangle}(0)$ there is a one-to-one correspondence between the shortest distance steps connecting two points on a square lattice and the corresponding steps on a triangular lattice (see Fig. 3.1). Therefore, we know that the degeneracy factor $g^{\triangle}_{M',N'}(0)$ for steps of energy $\mathcal{E}_0^{\triangle}$ on a triangular lattice must be identical to $g_{M',N'}(0)$ implicit in Eq. (2.3)! More precisely, if we assume the point (M,N) is in the first quadrant, and (M', N') is in the first sextant, then on a square lattice, shortest-distance step-links are oriented at either 0° or 90°, whereas on a triangular lattice they are oriented at either 0° or 60° (i.e. in the first sextant, the shortest path cannot have links oriented at 120°). In both cases, the individual step-links can only be oriented in one of two directions and, therefore, besides the transformation between coordinates, the total number of path arrangements is the same.

Using Eq. (2.3) and Stirling's approximation, we find the low-temperature free

energy (Appendix B.1 provides the lowest-order correction):

$$F \approx \mathcal{E}_0^{\triangle} - k_B T \, \ln[g_{M',N'}(0)] \approx \mathcal{E}_0^{\triangle} - k_B T \times$$
$$\times \left[(M'+N') \ln(M'+N') - M' \ln M' - N' \ln N' \right]. \tag{3.3}$$

Alternatively, we can transform Eq. (2.4) for the square lattice to the triangular lattice by just replacing $N/M \equiv \tan\theta$ with $(2\tan\theta)/(\sqrt{3}-\tan\theta)$. (This ratio is just N'/M', so it might be termed $\tan\theta'$.) [We must also make a simple (and ultimately inconsequential) change to $\mathcal{E}_0$.]

We now take the thermodynamic limit (M', $N' \gg 1$) and write M' and N' in terms of $M \equiv L\cos\theta$ and $N \equiv L\sin\theta$ via Eq. (3.1). Then dividing by L and defining[51]

$$\eta_{\pm}(\theta) = \cos\theta \pm \frac{\sin\theta}{\sqrt{3}}, \qquad \eta_0(\theta) = \frac{2}{\sqrt{3}} \sin\theta, \tag{3.4}$$

all non-negative in the first sextant, we straightforwardly find the step-edge line tension (or free-energy per unit length[52]) $\beta(\theta)$:

$$a_{\|}\beta(\theta) = 2\varepsilon\eta_+(\theta) - k_B T \left[s_+(\theta) - s_-(\theta) - s_0(\theta) \right], \tag{3.5}$$

where $a_{\|}$ is the nearest-neighbor spacing and

$$s_i(\theta) = \eta_i(\theta) \ln \eta_i(\theta), \quad i = +, 0, - \, . \tag{3.6}$$

For the special case of the maximally kinked orientation, Eqs. (3.4) – (3.6) reduce to

$$a_k \beta(30^\circ) = 2\varepsilon - k_B T \ln 2, \tag{3.7}$$

where $a_k = (\sqrt{3}/2)a_\parallel$ for the {111} surface. This result for the maximally kinked case (including steps at $\theta = 45°$ on a square lattice) was derived earlier from a direct examination of entropy.[53]

For specificity, we recall some established results. For a hexagonal lattice with just nearest-neighbor attractions, the critical temperature T_c is long known:[54]

$$k_B T_c = 2\varepsilon / \ln 3 \approx 1.82\varepsilon \ . \tag{3.8}$$

From the equilibrium shape of islands over a broad temperature range, Giesen *et al.*[17] deduced that the free energy per lattice spacing in the maximally kinked directions is 0.27 ± 0.03eV on Cu{111} and slightly smaller, 0.25 ± 0.03eV, on Ag{111}. Combining these results with Eq. (3.7), we find ε is 0.126eV on Cu{111} and 0.117eV on Ag{111}. In both cases, then, room temperature is somewhere between $T_c/9$ and $T_c/8$.

3.1.3 Main Result: Simple Expression for Low-T Stiffness

As shown just above, the step-stiffness $\tilde{\beta} = \beta(\theta) + \beta''(\theta)$ computed from Eq. (3.5) depends to leading order only on the combinatoric entropy terms s_0 and $s_\pm$ of Eqs. (3.5) and(3.6). Hence,

$$\frac{d^2 s_i}{d\theta^2} \equiv s_i'' \ = \ -\eta_i \ln \eta_i + \frac{\eta_i'^2 - \eta_i^2}{\eta_i}, \tag{3.9}$$

so that[55]

$$\tilde{s}_i \ \equiv \ s_i + s_i'' = \frac{\eta_i'^2 - \eta_i^2}{\eta_i}. \tag{3.10}$$

With this notation, the reduced stiffness is

$$\frac{\tilde{\beta} a_{\|}}{k_B T} = \tilde{s}_0 + \tilde{s}_- - \tilde{s}_+, \tag{3.11}$$

where

$$\tilde{s}_0 = \frac{2}{\sqrt{3}} \frac{\cos 2\theta}{\sin \theta}, \tag{3.12}$$

$$\tilde{s}_\pm = \frac{-2\cos 2\theta \mp 2\sqrt{3}\sin 2\theta}{3\cos\theta \pm \sqrt{3}\sin\theta}. \tag{3.13}$$

Adding these terms together gives our *main* result – a remarkably simple form for the reduced stiffness in the low-temperature ($T \ll \varepsilon/k_B$) limit:

$$\frac{k_B T}{\tilde{\beta} a_{\|}} = \frac{\sin(3\theta)}{2\sqrt{3}} = \frac{3m - m^3}{2\sqrt{3}(1+m^2)^{3/2}}, \tag{3.14}$$

where $m \equiv \tan\theta$.

3.1.4 Synopsis of Exact Results and Application to Range of Breakdown of Low-T Limit Near θ=0

To test how low the temperature should be for Eq. (3.14) to be a good approximation, we compare it to a numerical evaluation of the exact implicit solution of the Ising model. The derivation of this solution, outlined by Zia,[50] gives a 6^{th} order equation for $\beta(\theta)$. In essence, after conversion to our notation, his key result for the step free energy β is given by[56]

$$\frac{\beta a_{\|}}{k_B T} = \eta_0(\theta)\psi_1(\theta, T/T_c) + \eta_-(\theta)\psi_2(\theta, T/T_c), \tag{3.15}$$

where the ψ's are the solutions of the pair of simultaneous equations for the angular constraint,

$$\frac{\sinh\psi_2 - \sinh(\psi_1 - \psi_2)}{\sinh\psi_1 + \sinh(\psi_1 - \psi_2)} = \frac{\eta_-}{\eta_0} = \frac{\sqrt{3}\cot\theta - 1}{2}, \tag{3.16}$$

and the thermal constraint,

$$\cosh\psi_1 + \cosh\psi_2 + \cosh(\psi_1 - \psi_2) = f(z) \equiv \frac{1 + 3z^2}{2(z - z^2)}, \tag{3.17}$$

where $z \equiv \exp(-2\varepsilon/k_BT) = 3^{-T_c/T}$, via Eq. (3.8). The ratio η_-/η_0 of Eq. (3.16) is a monotonically decreasing function which is ∞ at θ=0°, 1 at θ=30°, and 0 at θ=60°.

In these high-symmetry directions, Eqs. (3.16) and (3.17) yield analytic solutions for β and $\tilde{\beta}$:

$$\frac{\beta(0)a_\parallel}{k_BT} = 2\cosh^{-1}\left(\frac{-1 + \sqrt{3 + 2f}}{2}\right) \tag{3.18}$$

$$\frac{\tilde{\beta}(0)a_\parallel}{k_BT} = \frac{2}{3}\frac{\sqrt{2(3 + 2f)(f - \sqrt{3 + 2f})}}{\sqrt{3 + 2f} - 1} \tag{3.19}$$

$$\frac{\beta(\pi/6)a_\parallel}{k_BT} = \frac{2}{\sqrt{3}}\cosh^{-1}\left(\frac{f - 1}{2}\right) \tag{3.20}$$

$$\frac{\tilde{\beta}(\pi/6)a_\parallel}{k_BT} = \frac{2\sqrt{3(f - 3)(f + 1)}}{f + 3}. \tag{3.21}$$

Details are provided in Appendix B.2. Akutsu and Akutsu[57] also derived these equations, in different notation[58] and from the more formal perspective of the imaginary path-weight method. Symmetry dictates that the solution at $\theta = 60° = \pi/3$ is the same solution as that at $\theta = 0°$. Furthermore, at $T = T_c$, $f(z) = 3$, so Eqs. (3.18)-(3.21) all go to 0, as expected.

To find $\tilde{\beta}$ in general directions, we solve Eqs. (3.16) and (3.17) [or, equivalently, Eq. (B.9)] numerically. As Fig. 3.2 shows, once T decreases to nearly $T_c/9$, Eq. (3.14)

more or less coincides with the exact numerical solution for the stiffness. At such low temperatures (compared to T_c), the approximation only fails below some very small, temperature-sensitive critical angle θ_c. Although it might seem easy to determine this angle by eye, estimating it quantitatively turns out to be a subtle and somewhat ambiguous task. We discuss two possible estimation techniques below.

In the first approach, we estimate θ_c to be the angle θ_1 at which the *curvature* of the exact solution changes sign. The points on the solid curve in Fig. 3.3 show θ_1 at several temperatures ranging from $T_c/9$ to $T_c/4$. At temperatures near and above $T_c/4$, θ_1 does not reliably estimate θ_c because there is a sizable curvature-

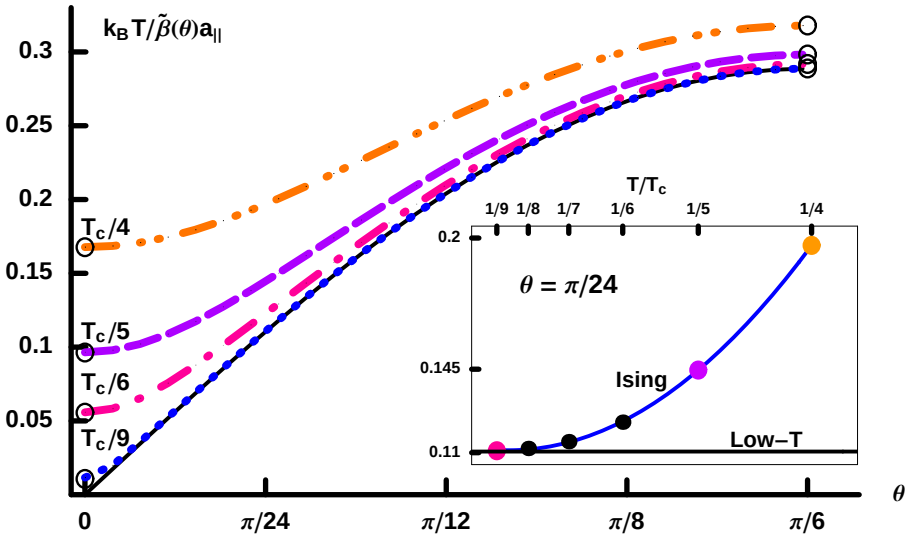

Figure 3.2: As the temperature drops close to $T_c/9$ (just below room temperature for Cu and Ag{111} surfaces), the numerical evaluation of the exact stiffness[50] approaches the solid line representing the low-temperature approximation given in Eq. (3.14). The small circles indicate evaluations using the exact results of Eqs. (3.19) and (3.21). At $T_c/9$, when θ decreases, the exact solution begins to deviate from the approximation when its curvature changes sign near $\theta \approx \pi/100 = 1.8°$. The scale here is linear, in contrast to the logarithmic scale of Fig. 2 of Dieluweit et al.[19] The inset shows more fully how the exact stiffness approaches the low-temperature limit for the particular azimuthal angle $\theta = \pi/24 = 7.5°$.

independent difference between the exact solution and the approximation given in Eq. (3.14) evident even at $\theta = 30°$ (see Fig. 3.2). On the other hand, as the temperature dips below $T_c/5$, this difference fades, and the use of θ_1 to estimate θ_c becomes ever more precise.

A second, more fundamental way to estimate θ_c comes from an examination of the assumptions required to derive the simple expression for the low-T limit Eq. (3.14) directly from the exact solutions Eqs. (3.16) and (3.17). In Appendix B.3 we show that to do so θ must be greater than some θ_2 satisfying

$$\cot\theta_2 \ll \left(\frac{4f-1}{\sqrt{3}}\right). \tag{3.22}$$

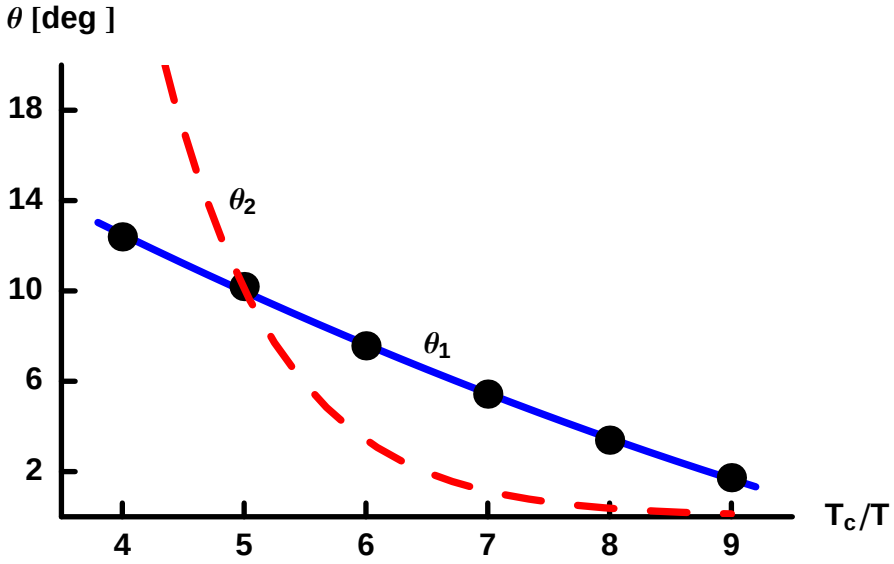

Figure 3.3: Two estimates for the critical angle θ_c, below which the approximation given in Eq. (3.14) begins to fail, as a function of T_c/T. The black dots connected by the solid, blue line represent the first estimate, defined to be the angle θ_1 at which the curvature of the numerically determined inverse stiffness changes sign. The dashed, red line represents the second estimate, $\theta_2 = \cot^{-1}[(4f-1)/(50\sqrt{3})]$. At angles below θ_c, the three theorems of Section 3.2 break down, and higher order terms are required in the expansion of the step partition function. At temperatures between $T_c/9$ and $T_c/8$ (roughly room temperature for Cu and Ag{111} surfaces), θ_c is on the order of a few degrees.

To give definite meaning to this inequality, we estimate θ_c directly from Fig. 3.2 at a single temperature, say $T_c/5$. At that temperature, θ_c is nearly 10°. If θ_2 is to accurately represent θ_c, it should also be around 10° at $T_c/5$. We enforce this by interpreting the '$\ll$' in Eq. (3.22) to mean '$= 1/50$.' The dashed (red online) curve in Fig. 3.3 shows the resulting θ_2 as a function of temperature. Clearly θ_1 and θ_2 are very different estimates for θ_c. While θ_2 is reliable at all temperatures (unlike θ_1), it is less precise than θ_1 at lower temperatures. A combination of θ_1 and θ_2 is therefore the best estimate for θ_c, being closer to θ_1 at lower temperatures, and closer to θ_2 at higher temperatures.

In essence, θ_c is no more than a few degrees between $T_c/9$ and $T_c/8$, regardless

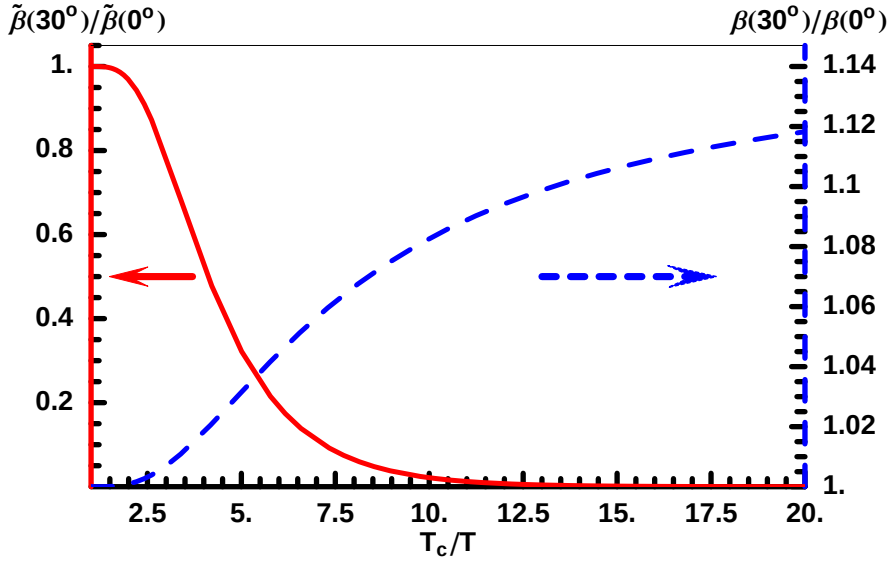

Figure 3.4: Ratio of the stiffness [solid red curve, left ordinate] and the free energy per length [dashed blue curve, right axis] for edges oriented in the maximally zig-zagged ($\theta = 30°$) and close-packed ($\theta = 0°$) directions, based on taking the ratios of Eqs. (3.21) and (3.19) and of Eqs. (3.20) and (3.18), respectively. The line-tension ratio increases slowly but monotonically to the T=0 limit $2/\sqrt{3} \approx 1.15$. In contrast, the stiffness ratio plummets toward 0, the value predicted by Eq.(3.14), providing an indicator how low T must be for this simple low-T formula to be a good approximation at all angles.

of which estimation technique is used. We therefore reach the practical conclusion that Eq. (3.14) is valid for almost all angles at temperatures near and below $T_c/8$, which fortunately happens to be around room temperature for Cu and Ag{111}.

Finally, we emphasize that $\tilde{\beta}$ varies significantly with angle, especially at lower temperatures (where the equilibrium crystal shape (ECS) is hexagonal rather than circular). If one wants to approximate $\tilde{\beta}$ as isotropic rather than using Eq. (3.14), one should not pick its value in the close-packed direction (viz. $\theta = 0°$); Fig. 3.4 provides stunning evidence of this conclusion. From Eq. (3.14) we also see that at low-temperatures the stiffness actually *increases* linearly with temperature. This contrasts with its behavior at high temperatures, where $\tilde{\beta}$ must ultimately decrease as the ECS becomes more nearly circular and the steps fluctuate more easily.

3.2 General Results for Stiffness in Lattice-Gas Models in Low-Temperature Approximation

In this section we present three theorems that are valid under two conditions: First, the energy term in the free energy must be a linear combination of $\cos\theta$ and $\sin\theta$. From Eq. (3.2) and [implicitly] Eq. (2.3) we see that this property holds true in general for lattice-gas models, even when considering next-nearest neighbors and beyond.[20] Second, the temperature must be low enough so that the entropy is adequately approximated by the contribution of the lowest order term, $k_B \ln g(0)$. This entropic contribution is due exclusively to geometry or combinatorics of arranging the fixed number of kinks forced by azimuthal misorientation. Hence, it must vanish

near close-packed directions (0° and 60° in the first sextant). For angles sufficiently close to these directions, in our case less than θ_c, the leading term becomes dominated by higher-order terms, and the three results no longer apply.

3.2.1 No Contribution from Energy to Lowest-Order Stiffness (LOS)

The first theorem is a remarkable consequence of the first condition, that the energy term in the free energy is a linear combination of $\cos\theta$ and $\sin\theta$. Since the stiffness $\tilde{\beta}(\theta) \equiv \beta(\theta) + \beta''(\theta)$ and since $\cos''\theta = -\cos\theta$ and $\sin''\theta = -\sin\theta$, we see that *the lattice-gas energy makes no contribution whatsoever to the low-T limit of reduced stiffness*, as shown explicitly for square lattices long ago.[16,18] Thus, we retrieve the result that the leading term in a low-temperature expansion of the reduced stiffness $\tilde{\beta}(\theta)/k_BT$ depends only on $g(0)$, which is determined solely by geometric (combinatoric) properties. Of course, higher-order terms (which are crucial near close-packed directions) do have weightings of the various configurations that depend on Boltzmann factors involving the characteristic lattice-gas energies. Furthermore, next-nearest-neighbor interactions can (at least partially) lift the $g(0)$-fold degeneracy of the lowest energy paths.[59]

3.2.2 Step Line Tension Not Extractable from LOS

An important corollary is that from the stiffness it is impossible to retrieve the energetic part of the step free energy, the major component of $\beta(\theta)$ at lower temperatures when the islands are non-circular! Thus, contrary to a proposed method

of data analysis,[60] one cannot regenerate $\beta(\theta)$ from $\tilde{\beta}(\theta)$ by fitting the stiffness to a simple functional form and then integrating twice. In this framework, the linear coefficients of $\cos\theta$ and $\sin\theta$ can be viewed as the two integration constants associated with integrating a second-order differential equation.[61]

3.2.3 LOS on fcc{111} Has 6-fold Symmetry

1. General Argument

Another important result is that the leading term in the stiffness at low temperature has the full symmetry of the 2D net of binding sites rather than the possibly lower symmetry associated with the full lattice. Specifically, for the present problem of the {111} face of an fcc crystal, the stiffness $\tilde{\beta}(\theta)$ to lowest order has the full 6-fold symmetry of the top layer rather than the 3-fold symmetry due to symmetry breaking by the second layer. In contrast, the step energy of B-steps ({111} microfacets) differs from that of A-steps ({100} microfacets), leading to islands with the shape of equiangular hexagons with rounded corners, but with sides of alternating lengths (i.e., ABABAB).

To see the origin of the 6-fold symmetry of the stiffness, suppose without loss of generality that steps in the X' direction have energy $\mathcal{E}_A$ per lattice spacing, so that those in the Y' direction have energy $\mathcal{E}_B$. Furthermore, we must make the crucial assumption that any corner energy is negligible. Then all shortest paths to (M', N') have the same energy $M'\mathcal{E}_A + N'\mathcal{E}_B$, with degeneracy still $g_{M',N'}(0)$. Thus, the free energy is $M'\mathcal{E}_A + N'\mathcal{E}_B - k_BT \ln g_{M',N'}(0)$, while that of its mirror point (through

the line at $\theta = 30°$) is $N'\mathcal{E}_A + M'\mathcal{E}_B - k_BT \ln g_{N',M'}(0)$. The crux of the proof is that $g_{N',M'}(0) = g_{M',N'}(0)$. Thus, while the free energies at the pair of mirror points differ, the energy parts are obliterated when the stiffness is computed (since M' and N' are linear combinations of $\cos\theta$ and $\sin\theta$), leaving just the contribution from the entropies, which are the same to lowest order.

2. Orientation-Dependent Part of 3-Atom Interaction

Within lattice-gas models with only pair interactions, there is no obvious way to distinguish A and B steps; the minimalist way to obtain different step energies for A and B steps within the lattice-gas model is to invoke a non-pairwise 3-site "trio" interaction associated with three [occupied] sites forming an equilateral triangle with NN sides. In contrast to the ones considered heretofore,[43,45,62,63] these novel trio interactions must be *orientation-dependent*: If the triangle points in one direction, say up, the interaction energy is positive, while if it points in the opposite direction, it has the opposite sign. (Of course, there could be a standard orientation-independent 3-site term in the Hamiltonian. As in the analogous situation for squares, we expect that such a term would simply shift the pair interactions, at least in the SOS approximation as discussed in Chapter 2.[59]) The contributions from such a symmetry-breaking interaction would cancel in the interior of an island (in the 2D bulk), but would distinguish A and B edges. Specifically, each side of the equilateral triangle is associated with a link, so that 1/3 of its strength can be attributed to each. Each link has a triangle on both sides, one of each orientation.

Hence, the difference between the energy per $a_{\|}$ of A and B steps is 1/3 the difference between the trio interactions in the two opposite orientations.

For the ground-state, minimum-number-of-links configurations, such a term will not lift the degeneracy since each configuration has the same 1) number of horizontal (X') links, 2) number of right-tilted diagonal links (Y'), and 3) *difference* between the number of convex and concave "kinks" (i.e., bends). Since this statement is not true for higher-energy configurations, the 6-fold symmetry is not preserved at higher orders. Nonetheless, at low T it should be a decent approximation for the stiffness (much better than for the island shape).

Thus, our result that the breaking of 6-fold symmetry on an fcc {111} is much smaller for the stiffness than for the free energy, is more general than the nearest-neighbor lattice gas model which underlies Eqs. (3.5) – (3.6) and the resulting Eq. (3.14) derived below. We reemphasize that the necessary assumptions are 1) that the orientational dependence of the step energy be just a linear combination of $\sin\theta$ and $\cos\theta$ and 2) that no interaction break the degeneracy of the shortest path corresponding to orientation θ. As above, for angles near close-packed directions, the higher-order terms become important at lower temperatures than for general directions. This feature is illustrated in Fig. 3.2 and its associated formalism is given in Appendices B.1 and B.3.

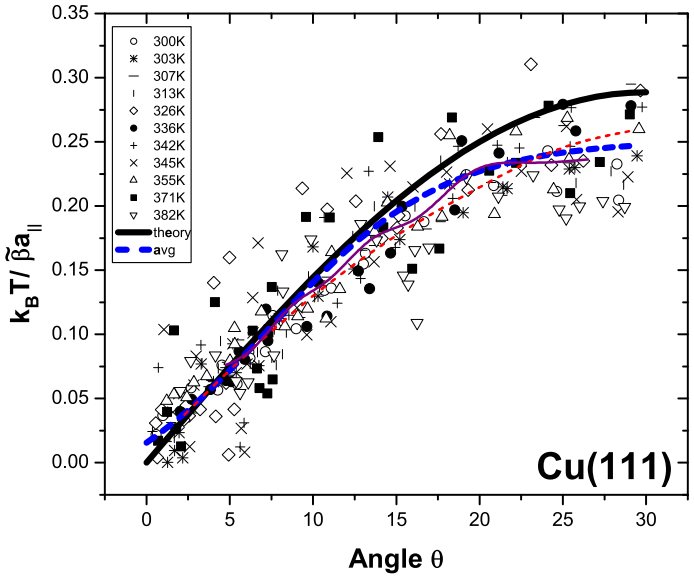

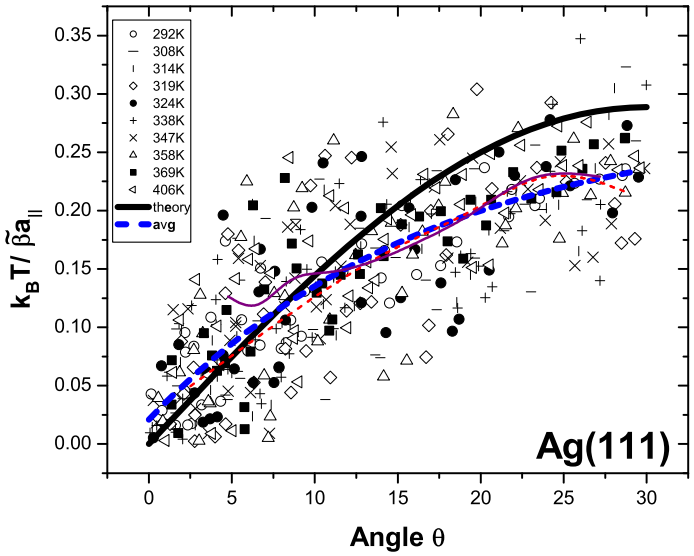

Figure 3.5: A comparison between Eq. (3.14) and experiments on Cu and Ag{111}. Eq. (3.14) appears as a solid black line, while the average of the experimental data is a thick dashed blue line. The agreement is reasonable at all angles. In either case the thin dashed red line is a [smoothed] average of the data for the given angle while the thin solid purple line corresponds to the angle mirror-reflected through a radial at 30°, i.e. at $60° - \theta$.

3.3 Comparison to Experiment

In Fig. 3.5 we compare Eq. (3.14) to measurements on Cu{111} and Ag{111}. The experimental data were derived from the equilibrium shape of 2D islands using the method described by Dieluweit et al.[19] The solid black line corresponds to Eq. (3.14), while the thick dashed blue line corresponds to the average of the experimental measurements. Eq. (3.14) captures the overall trend and is satisfactory at most angles and temperatures. As expected, Eq. (3.14) somewhat overestimates $\tilde{\beta}$ near $\theta = 0°$ (since the $T = 0$ singularity remains). Furthermore, near $\theta = 30°$ Eq. (3.14) somewhat underestimates the experimental $\tilde{\beta}$, but only by a factor of 1/6 for Cu{111} and 1/4 for Ag{111}. This is in striking contrast to the analogous NN theory for Cu{001} near 45°, which underestimates $\tilde{\beta}$ by a factor of 4. Finally, notice there is no clear temperature dependence in the measured data. This is further evidence that $\tilde{\beta}/k_BT$ is a constant at low-temperatures, as Eq. (3.14) suggests.

The agreement between theory and experiment is a pleasant surprise considering analogous comparisons made for Cu{001}[19] found $\tilde{\beta}$ to be four-times larger than the theoretical value at large angles (near $\theta = 45°$). It was later shown[22,23,59] that this discrepancy could be partially accounted for by considering next-nearest-neighbor (NNN) interactions (or right-triangle trio interactions, which turn out to affect $\tilde{\beta}$ at low temperatures in the same way). Clearly, the success of Eq. (3.14) suggests that these interactions are less relevant for {111} surfaces. This is reasonable because the ratio of NNN distance to NN distance is smaller by a factor of $\sqrt{2/3}$ on a triangular lattice compared to on a square lattice. Furthermore, in the close-

packed direction ($\theta = 0°$), for every broken NN-bond there are only one and a half broken NNN bonds on a triangular lattice, compared to two broken NNN bonds on a square lattice. These simple arguments help explain why NNN-interactions may increase $\tilde{\beta}$ by only 20 to 30% on Cu/Ag{111}, as opposed to 400% on Cu{001} surfaces.

3.4 A Novel Application: C_{60}/Ag(111)

In this final Chapter Section, we discuss a novel application of some of the ideas developed in the previous sections. Specifically, we consider the shapes of Ag(111) islands that are fully decorated by a ring of carbon bucky balls, or C_{60}. The growth of C_{60} on metal surfaces has been extensively studied.[64–67] On Ag(111), there is a near perfect lattice match, with C_{60} adlayers forming close-packed hexagonal islands having $2\sqrt{3} \times 2\sqrt{3}$ $R30°$ symmetry with respect to the substrate. C_{60} is relatively inert because all 60 of its constituent carbon atoms form three resonant bonds with their neighbors. In fact, in a recent set of experiments,[68] we showed that mass transport along Ag(111) steps is not affected when C_{60} attaches to them. Specifically, the bare regions of Ag(111) steps decorated by a single layer of C_{60} fluctuated as if the C_{60} were not there! This surprising result means the presence of C_{60} seems to have little effect on the stiffness of Ag(111) steps, a result which may prove useful in future organic electronics components. On the other hand, when a ring of C_{60} fully decorates a Ag(111) adatom or vacancy island, it appears to have a dramatic effect on the equilibrium shape of the island. Our recent experiments at room temperature

show that the equilibrium shape changes from a rounded hexagon to a near-perfect circle. Although this observation seems at first sight to conflict with the earlier one, we will show in the following sections that the two are entirely consistent. In the process, we will derive an accurate expression for the low-temperature line tension of a decorated step and show that the attractive interaction between C_{60} and a close-packed Ag step is roughly -126 meV per molecule, while the NN attraction between two C_{60} is roughly -87 meV. To our knowledge, these are the first experimental estimates of these interactions.

3.4.1 Experimental Observations

At room-temperature ($\sim T_c/8.2$), Ag(111) islands fluctuate about a fairly hexagonal equilibrium shape, as we would expect based on the anisotropy of the step line tension, expressed in Eq. (3.5). When C_{60} is deposited on the surface, however, it preferentially attaches to the corners of the Ag(111) islands, causing them to round, as shown via STM in the left-most image of Fig. 3.6. As more and more C_{60} is deposited, the island decoration becomes more complete, growing outward from the ever-rounding island corners. Eventually, the entire island edge is fully decorated or "coated," and the original hexagonal equilibrium shape is no longer evident, being replaced by a nearly perfect circle. This remarkable shape change is demonstrated in the middle and right images of Fig. 3.6, where a nearly bare, hexagonal island is compared with a fully decorated, circular island. The STM images evoke an analogy between the decorated island and a pearl necklace.

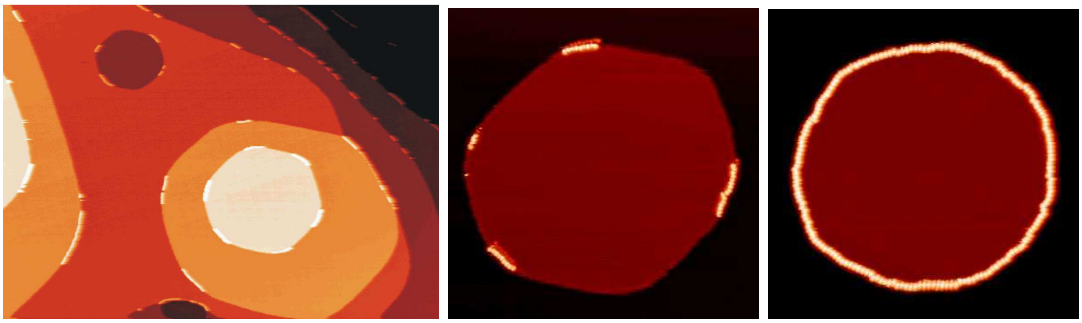

Figure 3.6: At room temperature, deposited C_{60} (bright white dots) decorates the corners of the hexagonal Ag(111) vacancy (dark brown) and adatom (lighter orange) islands, as shown in the left image. In the process, the island corners begin to round. In the middle image, the C_{60} coverage is low, so only the corners of the hexagonal Ag(111) adatom island (darker brown on black surface) are decorated. In the right image, the C_{60} coverage is larger, so the island becomes fully decorated and its equilibrium shape changes from a hexagon to a circle.

Interestingly, if the decorated island is large enough, it continues to fluctuate. Our experimental collaborator C. Tao followed the fluctuations of such an island for roughly 3500s, taking one STM image per 52s. By digitizing each image, we were able to determine the position of each C_{60} and animate their subsequent movement. Fig. 3.7a shows the first frame of the total animation. By averaging all images together, we confirmed the equilibrium island shape is a near circle, as Fig. 3.7b shows. With the positions of each C_{60} in hand, we could do a statistical analysis of their relative placement.

Fig. 3.7c shows the distribution of distance between the C_{60}. It is centered tightly around the C_{60} diameter of 1 nm, confirming their close-packed structure, regardless of step angle. Fig. 3.7d shows the distribution of angles between the C_{60}. To create this histogram, two vectors were drawn from the position of a C_{60}, one to its neighbor on the right and one to its neighbor on the left. The angle between

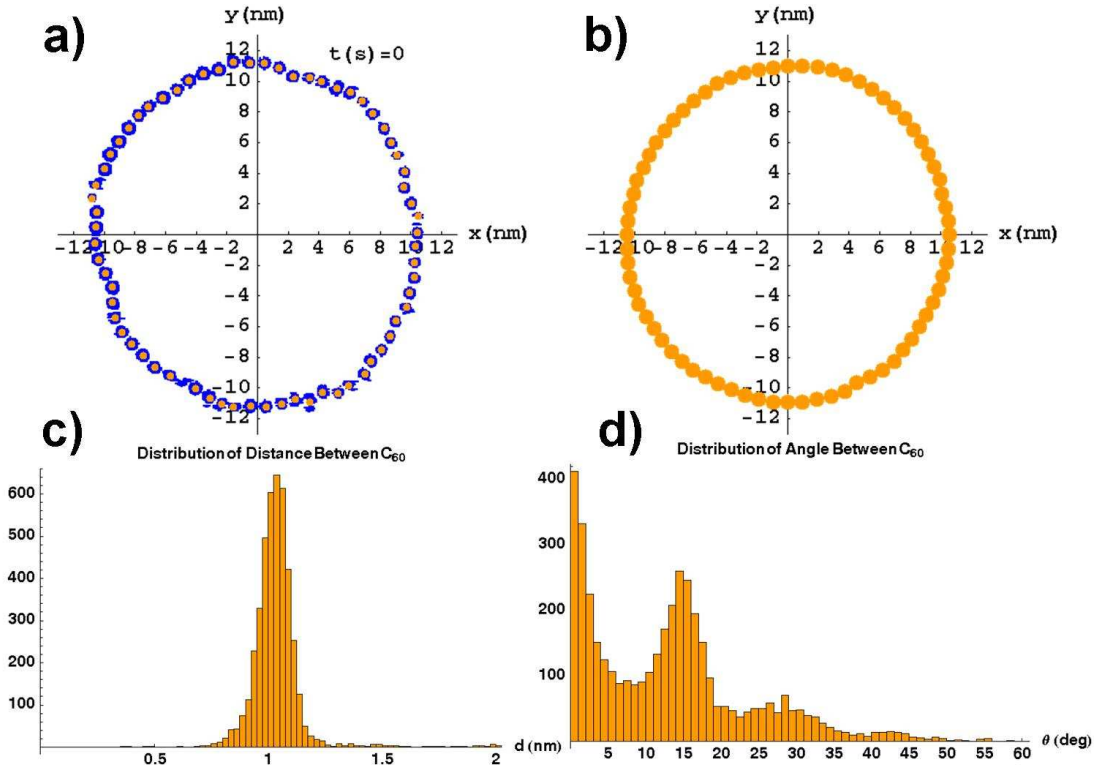

Figure 3.7: The first frame of an animation of a fluctuating Ag(111) step edge at room temperature fully decorated by C_{60} is shown in (a). The darker blue region is the actual STM data where the height cutoff was set so that only the tops of the decorating C_{60} could be seen. The lighter orange dots are the digitized positions of these C_{60}. In (b), all animation images were averaged together to determine the equilibrium island shape, shown here to be nearly circular. In (c), a histogram of the distance between C_{60} shows their close-packed arrangement, while in (d) a histogram of the angles between each C_{60} shows their preference for alignment.

these two vectors was then stored, and the process was repeated for each C_{60}. As the distribution clearly shows, most C_{60} are aligned with one another, but there are differences, typically in multiples of $\sim 15°$, where there is a substantial peak, followed by a smaller peak at $\sim 30°$ and an even smaller peak at $\sim 45°$.

If we are to adequately explain our experimental STM observations of the C_{60} decoration, we must address and/or include the following key features: (1) The C_{60}

prefers Ag steps, so there is obviously an attractive interaction between the C_{60} and the Ag step-edge adatoms. (2) Once C_{60} attaches to the step edge, it likes the corners (or Ag kinked-regions) more than the straighter edges. (3) Regardless of the step angle, C_{60} appears to close-pack along the step-edge, suggesting each step-edge C_{60} is quite mobile and attracted to the other C_{60}. (4) Although there is an attraction between C_{60} molecules, the attraction is weaker than the attraction between C_{60} and the Ag step-edge. If this were not the case, the C_{60} would begin to form a second coating layer before the Ag island is fully coated by the first layer. Likewise, the Ag-Ag adatom attraction is stronger than the Ag-C_{60} attraction, otherwise the C_{60} would tend to permeate into the Ag island, or C_{60} clumps would form on the bare parts of the surface. Thus, in order from strongest to weakest interaction strength, we have Ag-Ag, C_{60}-Ag, and C_{60}-C_{60}. Finally, (5), the C_{60} causes the equilibrium island shape to change from a near hexagon to a near-perfect circle.

In the following section, we propose a simple model which incorporates all of these features. With it, we calculate an estimate for the size of the C_{60}-Ag interaction ϵ^{AC}. We also derive an equation for the decorated step line tension as a function of the NN C_{60}-C_{60} interaction strength ϵ^{CC}. By performing a statistical analysis of the step fluctuations, we solve for the line tension and hence determine ϵ^{CC}. Finally, we show that our model is consistent with the experimental observation that a single layer of C_{60} does not significantly affect the step fluctuations, even though it has a profound effect on island shapes.

3.4.2 Simple Model for Ag(111) Step Edge Decoration by C_{60}

To determine the equilibrium shape of a Ag(111) island decorated by C_{60}, we calculate the anisotropy of the decorated step free energy F^d (here the "d" stands for decorated). Analogous to our earlier discussion for the bare Ag step, we imagine the decorated step connects the origin with the point (M', N') (assumed to be in the first, mirror-symmetric half of the first sextant), as shown in Fig. 3.8. As before, at low temperatures the free energy is well approximated by the first term in an Ising expansion of the decorated step partition function $Z^d \approx g_0^d \; e^{-E_0^d/k_BT}$, where E_0^d is the ground state energy of the decorated step, and g_0^d is the degeneracy of the ground state. In this case, F^d is written

$$F^d \approx E_0^d - k_B T \ln g_0^d \tag{3.23}$$

To determine E_0^d, we need only count bonds, as we did earlier, only now we have the Ag broken bonds as well as the Ag-C_{60} bonds and the C_{60}-C_{60} bonds.

Ground State Energy of a Decorated Step

The ground state energy E_0^d of the decorated step is just the ground state energy of the bare Ag step $E_0^{\triangle} = 2\varepsilon(M' + N')$ [see Eq. (3.2)] plus the interaction energies involving C_{60}. We break these interactions into two parts, one part E_0^{CC} from NN interactions between C_{60} and one part E_0^{AC} from interactions between C_{60} and Ag. Fig. 3.8 illustrates such a ground-state step. Here, the C_{60} forms NN bonds ϵ^{CC} with each of its neighbors. When C_{60} coats a close-packed region of the Ag step, it forms one NN bond ϵ^{AC} per molecule with the Ag atoms. On the other hand,

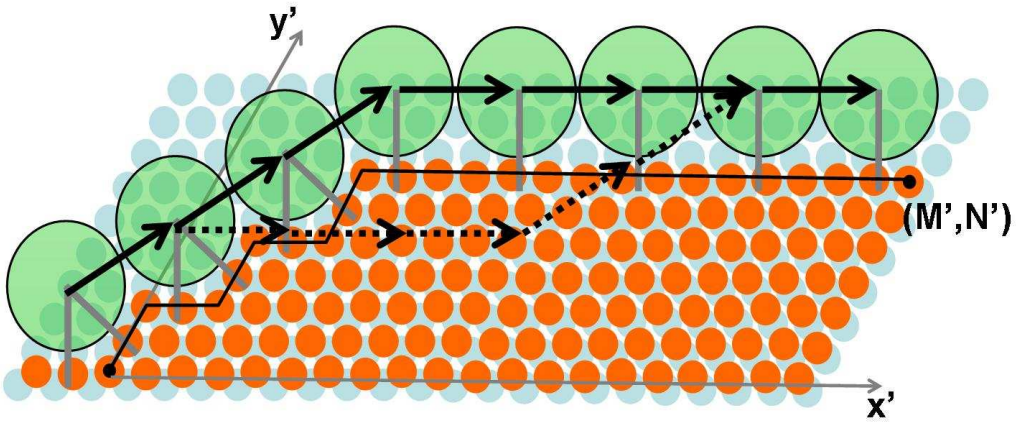

Figure 3.8: A Ag(111) step edge decorated by C_{60} in its ground state connecting the origin with the point (M', N'). The lighter-blue solid dots are the substrate Ag atoms, while the darker-orange solid dots are the Ag adatoms. The step edge is highlighed by a thin, solid line. The larger, see-through dots are the C_{60}. The C_{60} is close-packed and forms not only NN bonds (solid arrows) with each other, but also bonds with the Ag (solid, grey lines). If the bonds between the C_{60} are considered vectors, they come in two types, $N'/2$ pointing diagonally up (U) and $\sqrt{3}(M'-N')/2$ pointing horizontally (H). All steps having the same number of H and U bonds are degenerate. In particular, a degenerate ground state step is shown as a series of dotted vectors.

when C_{60} coats a fully kinked region of the Ag step, we imagine the Ag adatoms rearrange into double-kinks, so the C_{60} forms two NN bonds with the Ag adatoms per molecule while simultaneously remaining in registry with the substrate. (The fully kinked Ag direction is the natural close-packed direction for C_{60}.) This picture clearly explains why C_{60} prefers the kinked regions of the Ag step (or the corners of the Ag islands): it simply forms more bonds with the Ag step-edge atoms there. Summing everything together we have

$$\begin{aligned} E_0^d &= E_0^{\Delta} + E_0^{CC} + E_0^{AC} \\ &= 2\varepsilon(M'+N') + E_0^{CC} + E_0^{AC}. \end{aligned} \tag{3.24}$$

To prove the step shown in Fig. 3.8 is in the ground state, we note it is

the shortest possible step connecting the two endpoints. All longer steps require additional step kinks. Although this lowers the overall energy because of additional C_{60}-C_{60} and C_{60}-Ag bonds, there is a net energy gain because of costly broken NN Ag bonds, which, according to experimental observations, are the strongest. Finally, there are steps with the same microscopic length, but higher energy. These result when the Ag double-kinks combine to form triple and higher-order kinks. Such kinks necessarily cost energy because they cause C_{60} originally lying in the double-kinks to lose one of their 2 NN bonds with the Ag adatoms.

To determine the ground state energy as a function of angle, we need to determine how E_0^{CC} and E_0^{AC} depend on M' and N'. We begin with E_0^{CC}. If we imagine the C_{60} NN bonds are vectors, then they come in two types: $N'/2$ point diagonally up (U-bonds), while $(M'-N')a_{||}/a_C$ point horizontally (H-bonds). Here, $a_{||}$ is the Ag NN distance, while $a_C = 2\sqrt{3}\ a_{||}$ is the C_{60} NN distance. The energy is just the sum of these bond energies:

$$E_0^{CC} = \epsilon^{CC}\left(\frac{N'}{2} + \frac{M'-N'}{2\sqrt{3}}\right). \tag{3.25}$$

By dividing the C_{60} NN bonds into the H and U varieties, it is also easy to find E_0^{AC}. For every H-bond, the C_{60} forms one NN bond to the Ag, while for every U-bond it forms two. Thus,

$$E_0^{AC} = \epsilon^{AC}\left(N' + \frac{M'-N'}{2\sqrt{3}}\right). \tag{3.26}$$

Combining Eqs. (3.24 - 3.26), we have the ground state energy:

$$E_0^d = -\epsilon^{AA}(M'+N') + \epsilon^{CC}\left(\frac{N'}{2} + \frac{M'-N'}{2\sqrt{3}}\right) + \epsilon^{AC}\left(N' + \frac{M'-N'}{2\sqrt{3}}\right), \tag{3.27}$$

where we have rewritten the repulsive Ag-Ag severed bond energy ε (or equivalently the kink energy) as negative 1/2 the attractive Ag-Ag NN bond energy ϵ^{AA} (adding "AA" to remind us that it is an interaction energy between Ag adatoms alone). We now divide by the macroscopic step length L and remember Eq. (3.1), which gives M' and N' in terms of θ: $M' = L\cos\theta - L\sin\theta/\sqrt{3}$ and $N' = 2L\sin\theta/\sqrt{3}$. This gives our desired result

$$\begin{aligned}\frac{E_0^d\, a_{||}}{L} &= -\epsilon^{AA}\left(\cos\theta + \frac{\sin\theta}{\sqrt{3}}\right) + \frac{\epsilon^{CC}}{2\sqrt{3}}\left[\cos\theta + \left(2-\sqrt{3}\right)\sin\theta\right] + \\ &\quad + \frac{\epsilon^{AC}}{2\sqrt{3}}\left[\cos\theta + \left(4-\sqrt{3}\right)\sin\theta\right]. \end{aligned} \tag{3.28}$$

Degeneracy of the Ground State

Calculating the degeneracy of the ground state is relatively easy now that we have introduced the U- and H-bonds. To do so, we take the analogy between the C_{60} and a "pearl-necklace" one step further: we imagine each C_{60} is either an (U)gly pearl or a (H)andsome pearl depending, of course, on whether the bond to the right of the C_{60} is a U-bond or an H-bond. For example, in Fig. 3.8, the step corresponds to the following pearl necklace: UUUHHHH, whereas the other degenerate step corresponds to UHHHUUH. Since all steps with the same number of U- and H-bonds have the same energy in our model, the degeneracy of our ground state step can be reworded as a classic statistics problem: how many unique pearl necklaces can be made from $N'/2$ unique but (U)gly pearls and $(M'-N')/(2\sqrt{3})$ unique and (H)andsome pearls? The answer gives us g_0^d as a function of M' and N':

$$g_0^d = \binom{\frac{1}{2\sqrt{3}}(M'-N') + \frac{N'}{2}}{\frac{N'}{2}}. \tag{3.29}$$

We now take the thermodynamic limit (M',$N' \gg 1$) and use Stirling's approximation to find $\ln g_0^d$:

$$\ln g_0^d \approx \frac{1}{2\sqrt{3}} \Big[(M' - N' + \sqrt{3}N') \ln(M' - N' + \sqrt{3}N') - \sqrt{3}N' \ln(\sqrt{3}N') - \\ -(M' - N') \ln(M' - N') \Big]. \tag{3.30}$$

As we did for the energy, we divide by the macroscopic step length L and rewrite M' and N' in terms of θ to get our desired result:

$$\frac{\ln(g_0^d)\ a_{||}}{L} = \frac{1}{2\sqrt{3}} \Big[\{\cos\theta + (2-\sqrt{3})\sin\theta\} \ln\{\cos\theta + (2-\sqrt{3})\sin\theta\} \\ -(\cos\theta - \sqrt{3}\sin\theta) \ln(\cos\theta - \sqrt{3}\sin\theta) - 2\sin\theta \ln(2\sin\theta) \Big]. \tag{3.31}$$

3.4.3 Main Result: Decorated Step Line Tension Anisotropy

To get the line tension of the decorated step β^d, we divide Eq. (3.23) by L

$$\beta^d\ a_{||} \equiv \frac{F^d\ a_{||}}{L} = \frac{E_0^d\ a_{||}}{L} - k_B T \frac{\ln(g_0^d)\ a_{||}}{L} \tag{3.32}$$

Combining this with Eq. (3.28) and Eq. (3.31), and dividing by the thermal energy $k_B T$, we have an analytic formula for the low-temperature line tension of a decorated step (valid from 0° to 30°, symmetry giving all other angles):

$$\frac{\beta^d(\theta)\ a_{||}}{k_B T} = -\frac{\epsilon^{AA}}{k_B T}\left(\cos\theta + \frac{\sin\theta}{\sqrt{3}}\right) + \frac{1}{2\sqrt{3}}\left(\frac{\epsilon^{CC}}{k_B T}\ \gamma_0 + \frac{\epsilon^{AC}}{k_B T}\ \gamma_+\right) \\ + \gamma_0 \ln\gamma_0 - \gamma_- \ln\gamma_- - (\gamma_+ - \gamma_0)\ln(\gamma_+ - \gamma_0). \tag{3.33}$$

where we define the following:

$$\gamma_\pm \equiv \cos\theta + (2-\sqrt{3})\sin\theta \pm 2\sin\theta, \tag{3.34}$$

$$\gamma_0 \equiv \cos\theta + (2-\sqrt{3})\sin\theta. \tag{3.35}$$

The line tension, as expected, depends on the three interaction energies: ϵ^{AA}, ϵ^{CC}, and ϵ^{AC}. Since we already know $\epsilon^{AA} \sim 234$ meV[17] [see Eq. 3.8], by fitting the experimentally observed equilibrium decorated island shape, we should be able to determine the other two. In our case, this is especially easy since we know the equilibrium islands are circular. Thus, via the Wulff construction, we know that β^d should also be circular, so it should not depend on θ! We can therefore equate the right-hand-side of Eq. (3.33) for any θ. If we do this for the two high-symmetry directions, $\theta = 0$ ($\gamma_\pm = \gamma_0 = 1$) and $\pi/6$ ($\gamma_+ = 2, \gamma_- = 1, \gamma_0 = 1$), then we can actually cancel out ϵ^{CC} and solve for ϵ^{AC} in terms of ϵ^{AA}:

$$\begin{aligned} \beta^d(0)\ a_{||} &= \beta^d(\pi/6)\ a_{||} \\ -\epsilon^{AA} + \frac{\epsilon^{CC} + \epsilon^{AC}}{2\sqrt{3}} &= -\frac{2\epsilon^{AA}}{\sqrt{3}} + \frac{\epsilon^{CC} + 2\epsilon^{AC}}{2\sqrt{3}} \\ \rightarrow \epsilon^{AC} = (4 - 2\sqrt{3})\ \epsilon^{AA} &\approx 0.54\ \epsilon^{AA} \approx -126 \text{ meV}. \end{aligned} \tag{3.36}$$

We show a polar plot of the decorated step line tension β^d in Fig. 3.9 for a variety of different ϵ^{AC}, with $\epsilon^{CC} = (1/2)\ \epsilon^{AC}$. The anisotropy of β^d is a sensitive function of ϵ^{AC}; depending on its strength, the equilibrium island shape can continuously change from a hexagon rotated by 30° with respect to the bare Ag hexagonal island, to a near perfect circle (corresponding to the predicted $\epsilon^{AC} \approx (4-2\sqrt{3})\epsilon^{AA} \approx 0.54\ \epsilon^{AA}$), to a sharpened hexagon with the same orientation as the original bare Ag islands. It is reassuring that the predicted magnitude of ϵ_{AC} is less than that of ϵ_{AA}, as we expected based on our experimental observations.

We can now plug the predicted value of ϵ_{AC} into $\beta^d(\theta)$ to get a one-parameter formula for the decorated line tension in terms ϵ^{CC}. In Fig. 3.10 we plot in po-

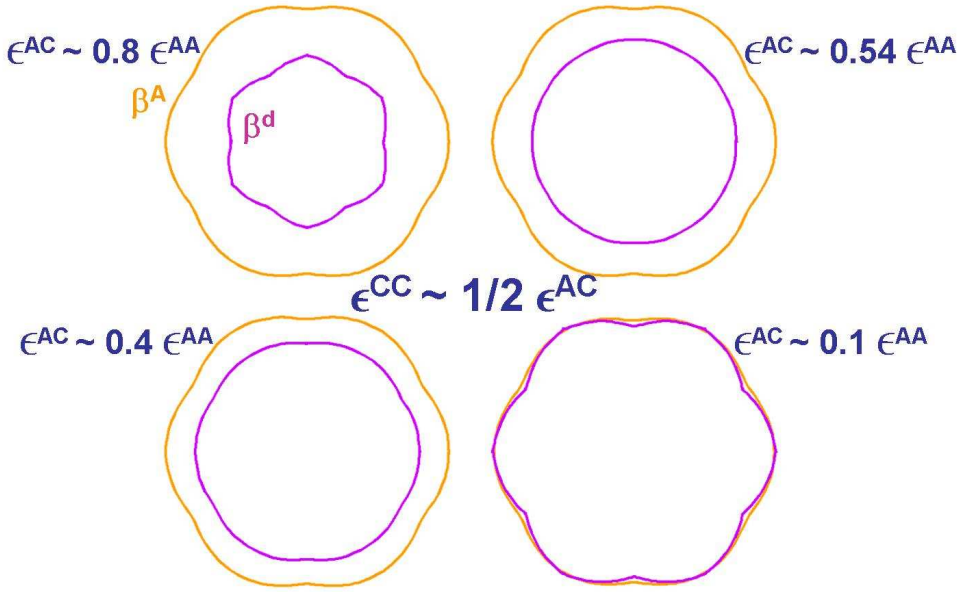

Figure 3.9: Polar plots of the line tension of a bare Ag step β^A (light, orange line) in comparison to the line tension β^d (dark, purple line) of a step decorated by C_{60}, for various values of ϵ^{AC} and $\epsilon^{CC} = 1/2\ \epsilon^{AC}$. If ϵ^{AC} is strong, as in the upper-left figure, it can actually cause the free energy to rotate by 30°, so the expected equilibrium island shape would still be hexagonal, but rotated by 30°. On the other hand, if $\epsilon^{AC} \approx (4 - 2\sqrt{3})\epsilon^{AA} \approx 0.54\ \epsilon^{AA}$, as in the upper-right figure, F^d becomes nearly a perfect circle, which corresponds to the observed circular equilibrium islands. Weaker ϵ^{AC} correspond to non-rotated hexagons, with the weakest interaction actually sharpening the cusps in the free energy, as in the lower-right figure, causing the original hexagonal island to become even more hexagonal.

lar coordinates the resulting line tension for a variety of different ϵ^{CC}. What we immediately notice is that ϵ_{CC} seems to have little affect on the anisotropy of the line tension. For all values tested, the shape is more or less circular. Instead, the contribution from ϵ^{CC} is relatively orientation independent, causing just a net shift in the line tension. We thus cannot determine its size by looking at just the decorated island shape change. Still, we can determine simple restrictions on its size. In

particular, $\beta^d(0)$ should satisfy the following equation:

$$\beta^d(0)\ a_{||} = \beta^d\ a_{||} = \epsilon^{AA}\left(\frac{2}{\sqrt{3}} - 2\right) + \frac{\epsilon^{CC}}{2\sqrt{3}}. \tag{3.37}$$

We can, of course, write similar formulas for any other orientation, but $\theta = 0$ is the simplest, and since β^d is orientation independent, the formula applies for all angles. Thus, if we can measure β^d independently, we can determine ϵ^{CC}. We will discuss such an independent measurement in the next section.

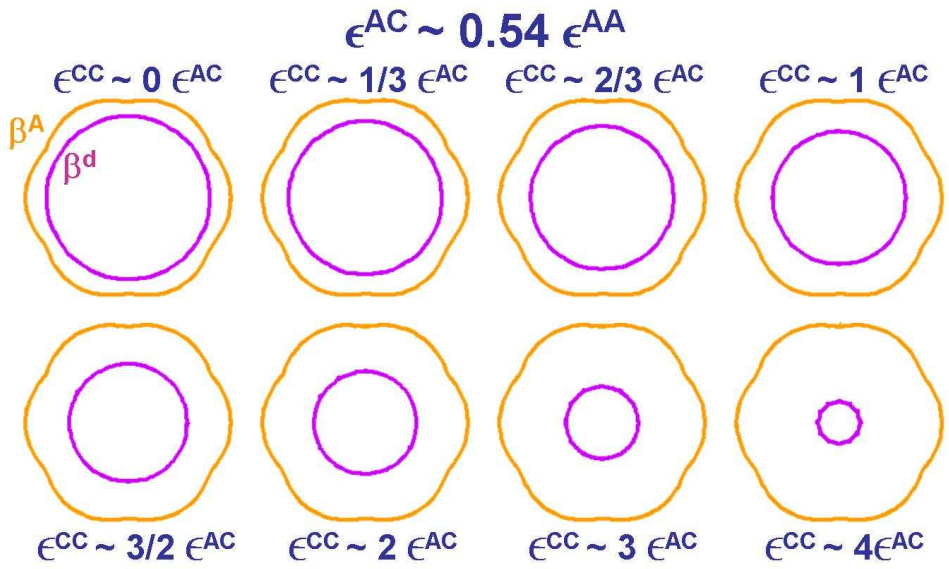

Figure 3.10: Polar plots of the line tension of a bare Ag step β^A (light, orange line) in comparison to the line tension β^d (dark, purple line) of a step decorated by C_{60}, for $\epsilon^{AC} = 0.54\ \epsilon^{AA}$ and various values of ϵ^{CC}. The images are listed in order of increasing ϵ^{CC} strength, with the upper-left corresponding to the weakest, and the lower-right corresponding to the strongest. For all values tested, ϵ^{CC} has little effect on the anisotropy of β^d. For this reason, analysis of the anisotropy of the decorated equilibrium islands is not enough to determine ϵ^{CC}.

3.4.4 Measuring the C_{60}-C_{60} Interaction from Step Fluctuations

Analyzing the fluctuations of islands has proven an effective way to determine the absolute line tension of the island step edge.[12,13,69–71] Here we extend the analysis to the fluctuations of Ag(111) islands decorated by C_{60}. In the usual treatment, the equilibrium island shape is determined by averaging many images together. Once the equilibrium shape is known, the fluctuations of each image island about the determined equilibrium shape are decomposed into their component Fourier modes. Using equipartition of energy, each mode has $(1/2)\ k_BT$. This provides an absolute energy scale from which the step-edge line tension can be determined.

Analyses of this type usually suffer from two problems: First, for pure islands, such as Ag or Cu, the number of modes is the number of atoms around the island perimeter. For modest island sizes, this is a huge number, so it is nearly impossible to experimentally resolve each mode (each atom). Instead, the island edge is under-sampled so that typically a hundred or so points are used to approximate its perimeter. This means that the line tension calculated from a single mode is usually smaller than the true value,[70] because now the total energy is spread among just a hundred or so modes, each of which necessarily shares more than $(1/2)\ k_BT$ of energy. One way to avoid this problem is to sum the line tension calculated from each of the resolved modes together[12,69] and then divide by the true number of modes that should be present. The problem with this approach is that it requires all resolved modes to fluctuate on the time scale of the experiment, but this is usually only satisfied for the longer-wavelength, lower-frequency modes. Including any

other modes will likely skew results. Second, adatom and vacancy islands are usually unstable on surfaces and tend to decay during the observation time. The usual solution is to monitor island fluctuations for decays of less than 10%.[12,69] How this actually affects the analysis is still unknown.

Fortunately, in our case, both of these problems are avoided. The first problem is avoided because we can resolve individual C_{60} decorating the Ag step, so we know exactly how many there are and therefore how many modes we should analyze. The second problem is avoided because the C_{60} prevent the island from decaying, so the total number of Ag and C_{60} remains more or less fixed (one or two C_{60} do occasionally break away).

To do the statistical analysis, our experimental collaborator C. Tao monitored via STM the fluctuations of two Ag(111) islands fully decorated by a single layer of C_{60}. The first data set contained 600 images of a Ag(111) island with a diameter of around 24nm coated by roughly 78 C_{60} (again, occasionally one breaks away) . The second data set contained 300 images of a Ag(111) island with a diameter of around 18nm coated by roughly 60 C_{60}. The image acquisition time was 13.1s for the first data set and 26.2s for the second. In both cases, because the scanning was relatively fast, it was difficult to actually determine the position of each C_{60}. Instead, for each image we determined the edge by setting the height cutoff so only the tops of the C_{60} could be seen. We then approximated the edge by a discrete series $R(\theta_n)$, where $\theta_n = n\pi/N$, with n an integer ranging from $-N+1$ to N, and $2N = 78$ or 60 (one for each C_{60}, depending on the data set). For both data sets, we could then average all $R(\theta_n)$ together to find the equilibrium shape $\langle R \rangle$, which was always a near-perfect

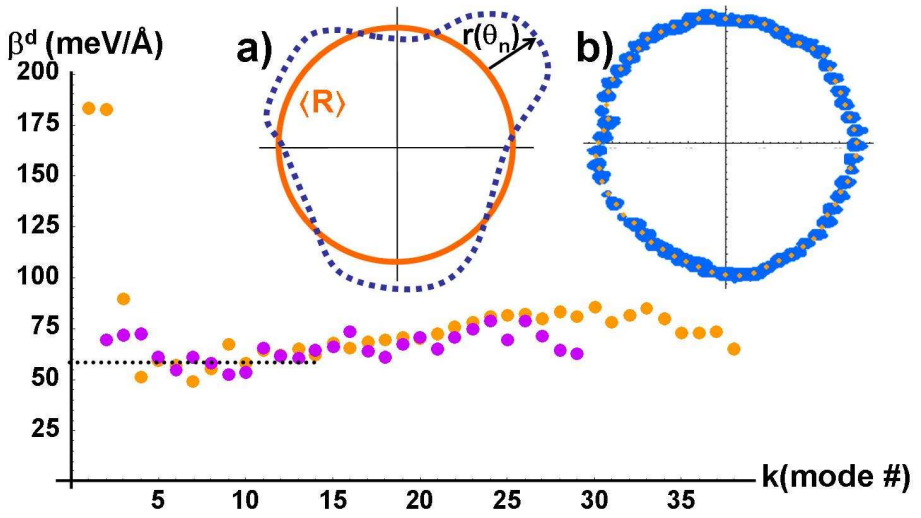

Figure 3.11: The measured decorated step line tension β^d as a function of the Fourier frequency k. The light orange dots correspond to the first data set (with 78 C_{60}), while the dark, purple dots correspond to the second data set (with 60 C_{60}). The best modes for analysis are between 5 and 15, and they give a value of roughly 60 meV/$\AA$. The two insets show how the data was digitized and analyzed. In (a), an island (dotted line) fluctuates about a circular equilibrium shape (solid, orange line labeled $\langle R \rangle$). The magnitude of the fluctuation, exaggerated in the schematic, is stored as a discrete list $r(\theta_n)$, where $\theta_n = n\pi/N$ (n=-N+1 to N) are $2N$ equally spaced angles ranging from -179° to 180°, one for each C_{60}. In (b), the STM data (dark blue) is approximated by a discrete list $R(\theta_n)$ (light, orange dots). By averaging all images together, the equilibrium shape $\langle R \rangle$ is determined, as is $r(\theta_n) = R(\theta_n) - \langle R \rangle$.

circle. To actually do the statistical analysis, we subtracted the equilibrium shape from each digitized island, leaving us with a new series $r(\theta_n) = R(\theta_n) - \langle R \rangle$ which basically gives the size of the island fluctuations as a function of angle. The insets in Fig. 3.11 demonstrate this process.

With $r(\theta_n)$ in hand, we Fourier transform to determine the magnitudes r_k of the component Fourier modes:

$$r_k = \frac{1}{2N} \sum_{n=-N+1}^{N} r(\theta_n) e^{ik\theta_n}, \tag{3.38}$$

where k is a dimensionless number (in contrast to a wavevector) ranging from $-N$ to N. The factor of 2 here is important, since there are a total of $2N$ C_{60} and, hence, $2N$ degrees of freedom. This can easily lead to confusion, however, since Eq. (3.38) is sometimes written with n being strictly positive, so the sum goes from 0 to, say, $N' \equiv 2N$, and the division is by N'. In any event, if Eq. (3.38) is used, and the equilibrium island shape is circular, then according to the equipartition of energy theorem, each degree of freedom has $1/2$ k_BT of energy (assuming the island is isolated, so there is no potential energy in the problem), from which the absolute step line tension β^d can be determined,[70,72]

$$\beta^d = \frac{1}{2} k_B T \frac{\langle R \rangle}{\pi k^2 \langle |r_k|^2 \rangle}, \tag{3.39}$$

where $\langle\rangle$ denotes an average over all images. If β^d is plotted as a function of k, it should be a constant. We show such a plot in Fig. 3.11, where we estimate β^d to be 60 ± 3.4 meV/Å (we only show the positive half of this plot since it is mirror-symmetric about $k = 0$).

We arrive at our estimate for β^d by considering only modes $k = 5$ to 15. We choose these modes because they fluctuate on the time scale of our experimental measurements. This is explicitly shown in Fig. 3.12, where the correlation function $G(t) = \langle [r_k(t) - r_k(0)]^2 \rangle$ is plotted for modes 2 through 9 (mode 1 corresponds to net island movement, which here is zero because we always center the island). Here we see that the $k = 2$ and 3 modes take perhaps 50 images or more to become uncorrelated. Thus, with 300 or 600 images, we have only 6 or 12 independent images, making $\langle |r_k|^2 \rangle$ too small (in other words, these modes do not fluctuate

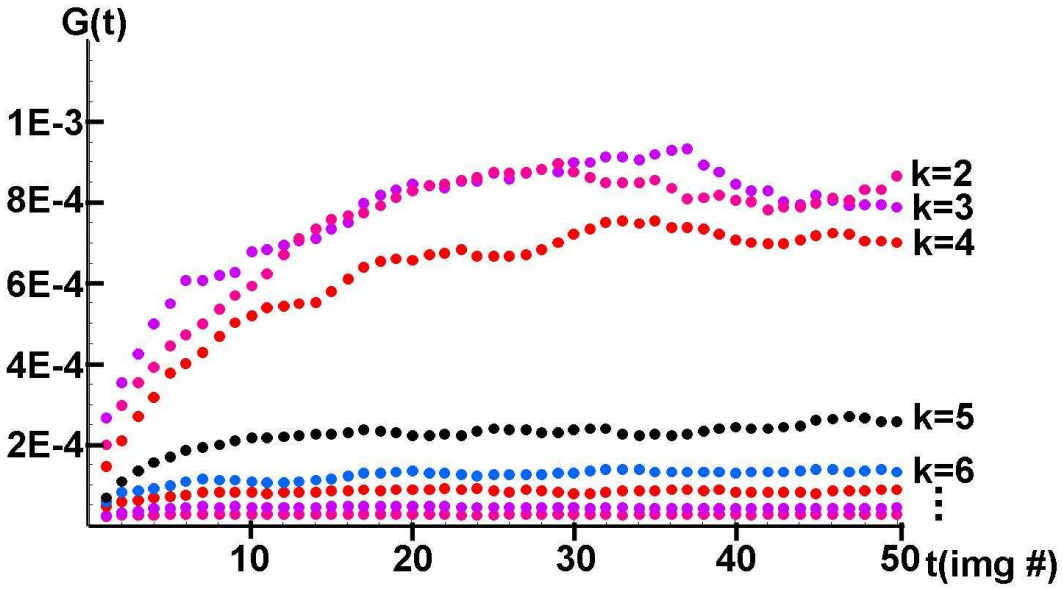

Figure 3.12: The correlation function $G(t) = \langle [r_k(t) - r_k(0)]^2 \rangle$ plotted as a function of time (reported as image number) for the first data set (600 images). The longer the wavelength, the longer it takes for modes to become uncorrelated and $G(t)$ to saturate. When computing averages, modes 5 through 15 are perhaps best because they saturate relatively quickly, but not faster than the image acquisition time.

so much on the time scale of our experiment) and therefore β^d to large, as seen in Fig. 3.11. On the other end of the spectrum, the large k fluctuate too fast, so the average is relatively noisy. The ideal modes, most of which are shown in Fig. 3.12, become uncorrelated after a few images, so there is enough data to get a good average, but the fluctuations are not faster than the image acquisition time.[72] Conservatively, this corresponds to modes $k = 5$ to 15. Using these modes, we find a fairly consistent value for β^d around 60 ± 3.4 meV/Å, as quoted above.

Now that we have an estimate for β^d, we can use Eq. (3.37) to estimate the size of ϵ^{CC}. Plugging in we find

$$\epsilon^{CC} \approx -87 \pm 34 \text{ meV}. \tag{3.40}$$

This estimate is consistent with our experimental observations which suggested $|\epsilon^{AA}| > |\epsilon^{AC}| > |\epsilon^{CC}|$. As seen in the error bar, however, the estimate is quite sensitive to the error in the measurement of β^d.

3.4.5 The Role of the Substrate

Here we briefly touch upon the effect the substrate might have on our calculations. The major concern is how and where the C_{60} sits on the surface. For example, does it rest with a hexagon or a pentagon facing down? Does it sit on fcc, hcp (hexagonal close-packed), or bridge sites? It turns out that incorporating both of these issues into our calculations is fairly straightforward. Basically, the interaction energy ϵ^{AC} can be renormalized to include both effects. Regarding the first question, we simply imagine ϵ^{AC} represents an average C_{60}, one that sits part of the time with a hexagon down and part of the time with a pentagon down. Incorporating *where* the C_{60} sits, however, requires more careful considerations. The problem here is that C_{60} likes the highly kinked region of the step, not only because it can get closer to the Ag step edge, but also because along this direction there is a perfect lattice-match between the C_{60} and Ag, allowing the C_{60} to always sit in the preferential hcp site[73] (or perhaps fcc, which according to DFT calculations[73] has nearly the same energy). On the other hand, C_{60} sitting on close-packed Ag steps cannot always sit in the preferential hcp site. Instead, because of the lattice-mismatch in this direction, it will likely sit in an average of all sites, hcp, fcc, and bridge (probably rarely bridge). As before, we incorporate this effect into ϵ^{AC}. In-

stead of the difference in energy between C_{60} sitting along a close-packed step and a fully kinked step only being one ϵ^{AC} bond per molecule, it is now one plus the difference in the hcp energy and the average of the hcp, fcc, and bridge energies. This will likely only be a small effect, something on the order of 30 meV, as estimated from the DFT calculations.[73] On the other hand, the C_{60} may continue to prefer the hcp site. If this is the case, it may adjust itself slightly to always reside there. This will induce small kinks in the decorated step which we calculate to be around 15°, perhaps explaining the histogram of C_{60} angles shown in Fig. 3.7d. This effect tends to minimize the role of the substrate, and the slight rearrangements will not have a profound effect on our calculations. Note, however, that a lattice-gas model is still appropriate, since at this temperature the fcc and hcp sites are far more favorable then other sites.

3.4.6 Why C_{60} Does Not Affect Ag Step Fluctuations

Before concluding, we return to the original puzzle presented in the introductory paragraph of this section: if C_{60} significantly affects the equilibrium island shape of a decorated step, why does it not also affect the step fluctuations? The key to this question is, again, the step stiffness. The stiffness, after all, is the parameter controlling step fluctuations, not the line tension. As we discussed in the theorem in section 3.3.1, there is no contribution to the lowest-order stiffness from the ground-state energy. Just like bare Ag steps, the energetic contribution to the low-temperature decorated step line tension is a linear combination of sines and

cosines, as Eq. (3.33) demonstrates. Thus, when calculating the decorated step stiffness, this portion cancels out. Even though ϵ^{AC} and ϵ^{CC} are significant, they do not affect the step fluctuations. Instead these are controlled by entropic effects alone. For steps that are only partially decorated, the result remains valid. Here, however, the entropic effects are also reduced. In fact, the only obvious effect seems to be the rearrangement of Ag step kinks into double-kinks to accommodate the C_{60}. This would only remove the highest-frequency oscillations, though, so it is not surprising that partially decorated steps seem to fluctuate in virtually the same way as bare ones.

3.5 Concluding Discussion

By generalizing the low-temperature expansion of the nearest-neighbor square lattice-gas (Ising) model to a triangular lattice, we have found a remarkably simple formula for the orientation dependence of the {111} surface step stiffness. This formula, unlike its square lattice analog, fits experimental data well at general angles, suggesting that NNN-interactions are relatively unimportant on {111} surfaces.

To corroborate this picture and explain the success of Eq. (3.14), we have used the VASP package[39] to perform first-principle calculations. In particular, Chapter 4 discusses calculations of the ratio of the NNN to NN interaction strength. Results[38] suggest that this ratio is roughly an order of magnitude smaller on Cu{111} than on Cu{001}, and essentially indistinguishable from zero. This tentative finding is consistent with expectations from the semiempirical embedded atom method, which

predicts that indirect interactions are insignificant/negligible between atoms sharing no common substrate atoms.[43] In Chapter 4 we also discuss the difference in trio interactions between oppositely oriented triangle configurations.

We expect that our formula, as well as the general 6-fold symmetry of the stiffness (except in close-packed directions), should be broadly applicable to systems in which multisite or corner energies are small and for which the bond energies are considerably higher than the measurement temperature. Studies which ignore the 3-fold symmetry breaking on metallic fcc {111} substrates, such as a recent investigation of nanoisland fluctuations on Pt{111},[70] should be good representations. Many recent investigations[74,75] focus on the larger asymmetry of the kinetic coefficient,[76] taking the stiffness to be isotropic. In such cases, this stiffness should not be characterized by its value in close-packed directions.

Finally, using the ideas developed in this Chapter, we have modeled the decoration of Ag(111) steps by C_{60}. Our model is consistent with experimental observations and helps explain not only the remarkable shape change decorating C_{60} induce in Ag islands, but also their surprisingly small effect on the island step-edge fluctuations. Using our model, we predict that the attractive Ag-C_{60} interaction is -126 meV per molecule and the NN C_{60} attraction is -87 meV. We believe this model is the first of its kind and should be extendable to a wide variety of decorated stepped surfaces, allowing a better understanding of how such decoration can be used to alter and/or control the evolution of microstructures.

Chapter 4

Extended Lattice Gas Interactions of Cu on Cu(111) and Cu(001): Ab-Initio Evalution and Implications

Lattice-gas models provide a powerful and convenient route to explore how microscopic energies influence the statistical mechanics of mesoscopic structures on crystalline surfaces. Such models underlie most Monte Carlo (and transfer matrix) simulations. They assume that overlayer atoms (or other adsorbed units) sit at particular high-symmetry sites of the substrate, an intrinsic assumption of epitaxial growth, for example. The parameters of the model are then the interaction energies between such atoms and/or the barriers associated with hops between the high-symmetry positions.

Lattice-gas models are generally used in two generic ways. In the first approach, one selects a few energies that are likely to dominate the physics of interest and then computes with Monte Carlo simulations the desired equilibrium or dynamic properties. The dangers of this approach are: a) the properties of interest may be relatively insensitive to the specific interactions and b) there may be other interactions that are non-negligible, so that the deduced energies are effective rather than actual.

The second approach[35,77–79] begins by actually computing the (many) energies of importance, a task that is now possible with efficient density-functional-theory

packages such as VASP (the Vienna Ab-initio Simulation Package).[39–42] This process can be used to compute interaction energies between relatively distant neighbors. One should also compute multi-atom interactions, which can also be significant.[43,45,62,63] This approach is appealing because the calculated interaction energies can be self-consistently checked for completeness, thereby diminishing the risk discussed in (b) above. Assuming that one has sufficient computational power to compute all the interactions that contribute at the level of the desired precision, there is still the danger that the interactions depend sensitively on the local environment, making a simple lattice gas description inadequate.

These caveats notwithstanding, lattice gas models have been extensively used in the realm of surface physics to describe such diverse phenomena as phase transitions, concentration-dependent diffusion, and growth. In Chapters 2 and 3, we used such a model to compute the orientation dependence of step stiffness—the inertial parameter for steps in the step continuum model[5]—for the (001) and (111) faces of Cu.[59,80] This work illustrates both successes and some shortcomings of using a lattice-gas model with just nearest-neighbor (NN) interactions: whereas the step stiffness on Cu(111) is well described by NN interactions alone, the step stiffness on Cu(001) requires the inclusion of next-nearest neighbor (NNN) and perhaps even trio interactions. In this case, a firm understanding of the adatom interactions would be an ideal way to construct an appropriate theory.

With this goal in mind, we have performed ab-initio calculations to determine the strengths of interactions between Cu adatoms on Cu(001) and Cu(111). For these systems we have tested the applicability of a lattice-gas model and have

determined which interactions are essential and which can be ignored.

Fig. 4.1 shows a summary of the calculated interactions between Cu adatoms on Cu(111); the corresponding interactions on Cu(001) are analogous. The first row shows the pairwise interactions of interest. Besides NN interactions (of energy E_1), we have also considered n^{th} nearest-neighbor interactions (of energy E_n) out to n=4. Based on our work in the previous two Chapters,[59,80] as described above, we expect NNN interactions to be negligible on Cu(111), but significant on Cu(001).

The second row of Fig. 4.1 shows the trio-interactions of interest. These interactions are the non-pairwise part of the interaction among three nearby adatoms.[43,62] These include the trios ($E_{a/b}$) for three NN adatoms forming an equilateral triangle (for which no Cu(001) counterparts exist), the trio (E_c) for three collinear adatoms, and the trio (E_d) for three adatoms forming a NN-isosceles triangle with apex angle 90° on Cu(001) and 120° on Cu(111) (the 'd' stands for 'dent'). Based on our work

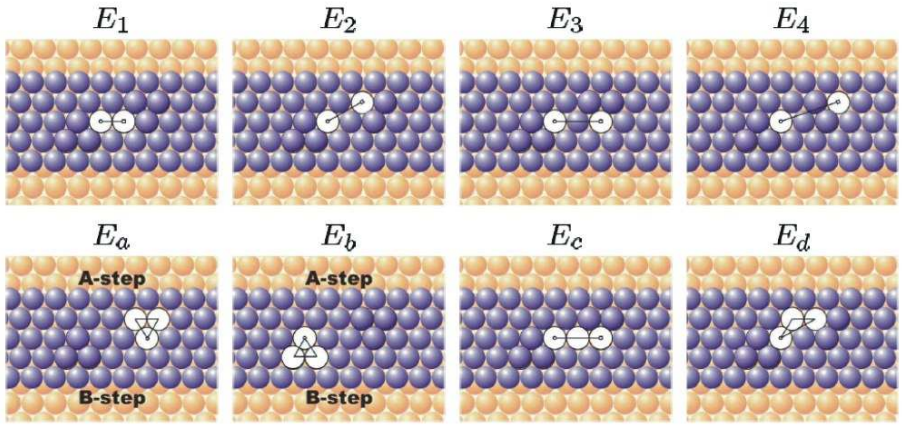

Figure 4.1: Interactions of interest (only shown for Cu(111); the interactions on Cu(001) are analogous). Dark blue spheres represent adatoms, lighter orange spheres represent substrate atoms, and white spheres represent adatoms involved in the interactions of interest. Pair interactions are shown in the top row, and trio interactions are shown in the bottom row.

in Chapter 2,[59] we expect E_d to affect the step stiffness on Cu(001) in the same way as E_2 (so that the effective NNN interaction is $E_2 + E_d$).

As illustrated in the two lower-left sub-figures of Fig. 4.1, when one includes the substrate layer upon which adatoms are adsorbed, the 6-fold symmetry of the adsorption layer is reduced to 3-fold. One should then, at least in principle, distinguish between the trio interactions E_a and E_b. Whereas E_a triangles are made from A-microfacets, E_b triangles are made from B-microfacets. As we noted in Chapter 3,[80] the difference between E_a and E_b provides the simplest way to account for the difference between energies of A- and B-steps within a lattice gas framework.

The remainder of this Chapter is divided into three sections. In the next section we describe the details of our calculations. In Section 4.2 we present and discuss our results and the implications. Finally, we summarize and offer concluding remarks in Section 4.3. The attached Appendix C provides details related to the error analysis of our computations.

4.1 Method

To accurately gauge the relative size of the Cu adatom-interactions of interest within the framework of density functional theory,[81,82] we used VASP,[39] together with the supplied Cu ultrasoft-pseudopotential (with a basis energy cut-off of 17.2 Ry), and the Perdew-Wang '91 generalized gradient approximation[83,84] (GGA). To speed up electronic relaxation, we used the method of Methfessel and Paxton[85] with a width of 0.2 eV.

We modeled the surfaces of Cu(001) and Cu(111) by constructing two large supercells for each surface, one containing up to $(14 \times 3 \times 2)$ atoms, the other containing up to $(14 \times 4 \times 2)$ atoms; we refer to these, respectively, as (3×2) and (4×2). Using the (3×2) cell, fourth-neighbor pair interactions and beyond were assumed to be negligible and therefore ignored, whereas using the (4×2) cell, for self-consistency, fourth-neighbor pair interactions were included (and ultimately verified to be negligible). To assure energy convergence to within a few meV, we sampled the Cu(111) (4×2) supercell using a $(6 \times 12 \times 1)$ mesh of **k**-points, and the Cu(001) (4×2) supercell using a $(5 \times 10 \times 1)$ mesh. A similar density of **k**-points was used for the (3×2) cells. (Because we never directly compared energies between cells, maintaining the same density of **k**-points between cells was irrelevant.)

We began all calculations by filling the first seven layers of the supercell, thereby producing—when periodically repeated in the three orthonormal symmetry directions— a series of seven-layer-thick, parallel slabs buffered by seven layers of vacuum. Here, as in all calculations, the slab lattice parameter was fixed at 3.64 Å—the value obtained from a bulk GGA calculation for a $(1 \times 1 \times 1)$ supercell sampled using an $(11 \times 11 \times 11)$ mesh of **k**-points. We then computed the slab energy in two ways: first with constrained relaxation normal to the surface alone, and second with full relaxation. In both cases, we held the inner three layers of atoms fixed at their calculated bulk positions, while the outer-layer atoms relaxed until the net force on them was less than 0.01 eV/Å.

Next we placed adatoms on the top and bottom of the slab. The 7-layer thickness of the slab sufficiently reduced interactions through the slab between opposite

sides[86] (see Appendix C for details). An alternative would be to put adatoms on just one side of the slab,[78,87,88] which would allow thinner slabs to be used for the substrate. (Since we are considering homoepitaxy, presumably there would be minimal charge-transfer effects requiring correction.[86]) We then recomputed the total energy in the same ways as before, allowing for both full and constrained relaxation. We repeated this procedure for a variety of adatom arrangements. This allowed us to construct a set of independent equations that we could solve to obtain the various interaction energies of interest.

To illustrate our technique, Fig. 4.2 depicts all Cu(001) calculations. The figure shows the top (001) surface of the aforementioned seven-layer slab (the [yellow] boxed region representing the top of the supercell); the lighter gray spheres represent surface atoms while the darker [orange] spheres represent adatoms. Although the bottom of the cell is not shown, we constructed it to be identical to the top.

The upper-left subfigure shows the arrangement of adatoms used in our first calculation. For this arrangement, the top and bottom surface of each supercell contains one adatom, so that the energy per supercell — after subtracting off the slab energy—is $E_0 + E_3$, where E_0 is the energy of introducing and adsorbing an atom on a clean substrate. Even though interactions beyond third-neighbors are not accounted for, interactions between supercell images up to third-neighbors are included.

The top-middle subfigure shows the arrangement of adatoms used in our second calculation. Here, the top and bottom of each supercell contains two NN adatoms. Summing over all intra- and inter-supercell interactions as before, the

energy of this configuration (again minus the slab energy) s $2E_0 + E_1 + 3E_3$.

Continuing in this way, we generated six more equations with the introduction of just three more unknowns: E_2, E_c and E_d. In total, then, we were left with eight independent equations, of which we could choose any six to solve simultaneously for the six interaction energies of interest. By comparing solutions from different sets of

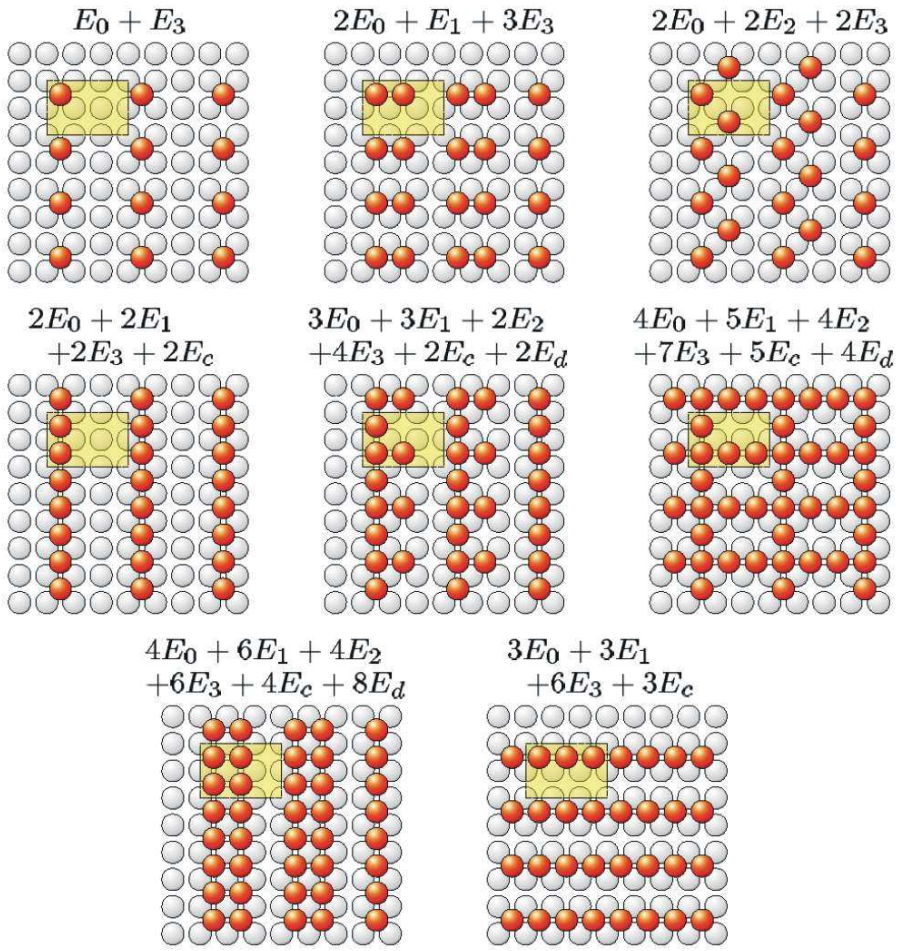

Figure 4.2: A summary of calculations performed for Cu(001) using the (3×2) cell. Each sub-figure corresponds to a different arrangement of adatoms (dark-orange spheres) on the substrate (light-gray spheres) with total energy given by a different linear combination of adatom interaction energies, and each small rectangle represents the top of the (3×2) cell. When taken together, any six equations can be solved to determine the six energies of interest.

equations, we could self-consistently check our energies and also roughly estimate—by noting the variation in values—the error in the calculations. (See Appendix C for more details.)

In much the same way—as illustrated in Fig. 4.3—we calculated adatom in-

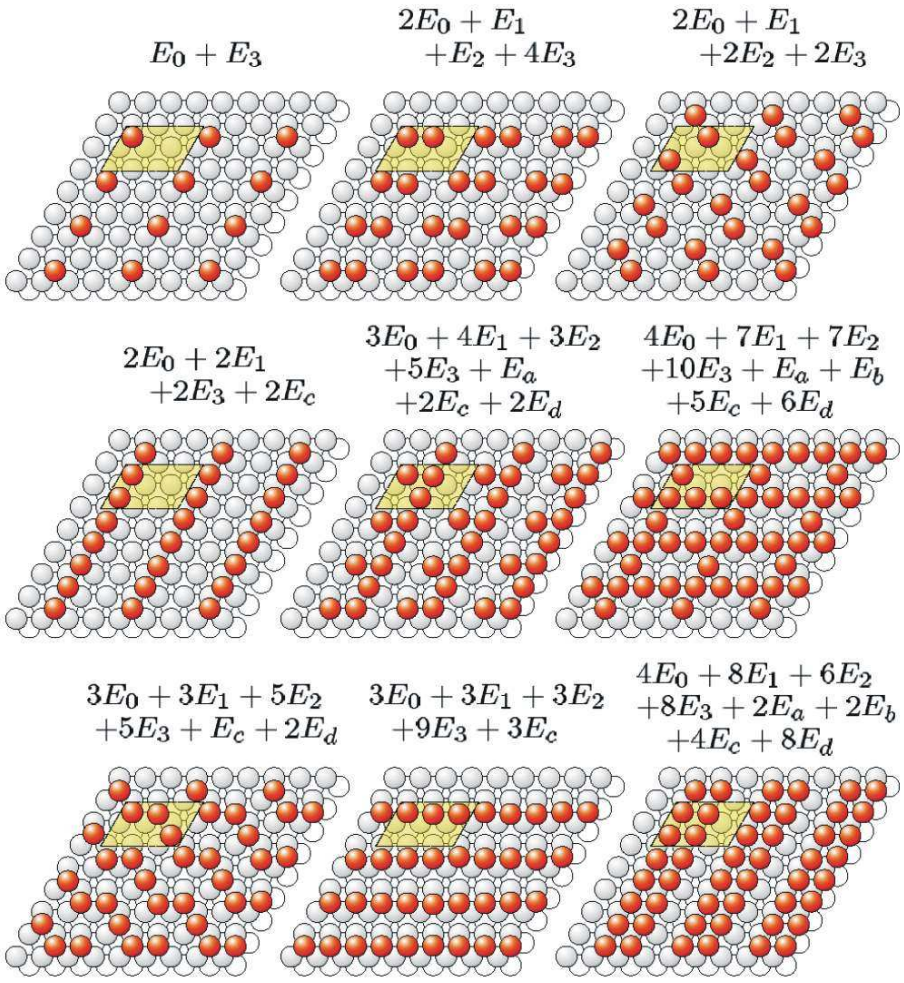

Figure 4.3: A summary of calculations performed for Cu(111) using the (3×2) cell. As in Fig. 4.2, each sub-figure corresponds to a different arrangement of adatoms (dark-orange spheres) on the substrate (light-gray spheres) with total energy given by a different linear combination of interaction energies, and each small parallelogram represents the top of the (3×2) cell. Here, however, because the triangle trio interactions depend on orientation, there is an interaction energy E_a for down-pointing triangles and E_b for up-pointing triangles. When taken together, any eight equations can be solved to determine the eight energies of interest. (Note that the up-pointing trio arrangement is not shown above.)

teraction energies for the Cu(111) (3×2) cell, the only noteworthy difference being the evaluation of the NN-trio interaction energies, $E_{a/b}$. Instead of eight, there were now ten independent equations (only nine are shown in Fig. 4.3—the missing configuration is identical to the middle subfigure with up-pointing triangles instead of down-pointing, so that E_a is replaced with E_b), of which we could choose any eight to solve for the eight interaction energies of interest.

Finally, the entire process was repeated for the (4×2) cells. Although most of the configurations remained unchanged, the inclusion of E_4 required a few additions and minor modifications in order to obtain the proper number of independent equations.

4.2 Results and Discussion

The results of our calculations are listed in Table 4.1. Only data for full relaxation are shown because data for constrained relaxation do not differ in any significant way: Specifically, data for the fully relaxed Cu(001) (3×2) cell differed from their vertically relaxed counterparts by no more than 13 meV, and often by less than 5 meV (the differences typically in proportion to the size of the interaction). Provided the system is not in a metastable state, this observation has powerful consequences: it validates the description of Cu surface energetics using a lattice gas model, where one assumes atoms sit at preferential, high-symmetry positions. In other words, while relaxation from these preferred positions inevitably occurs, the amount of relaxation negligibly changes the various interaction energies of impor-

tance. We therefore only require a finite number of 'typical' or 'average' interactions to fully describe the system, making a lattice-gas model appropriate.[89]

Besides the interaction energies discussed earlier, estimates for E_0, the energy of introducing and adsorbing an atom on a clean substrate, and E_s, the surface energy per atom, on both Cu(001) and Cu(111) are included (E_s was calculated by comparing slab energies of varying thickness, as discussed in the literature.[90]) The surface energies compare well with previous results; in particular, Spišák[91] found the surface energy of Cu(001) to be 606 meV/atom, while Wang *et al.*[92] found it to be 582 meV/atom. Our estimate of 600 meV/atom agrees with both. Similarly, Wang[92] estimated the surface energy of Cu(111) to be 462 meV/atom, in nearly exact agreement with our result.

The accuracy of our calculations is further confirmed by the excellent overall agreement between results using the (3×2) and (4×2) cells, where energies

E(meV)	**Cu(001)**		**Cu(111)**	
	(3×2)	(4×2)	(3×2)	(4×2)
E_s	600	600	462	465
E_0	-3149±16	-3146±14	-2922±15	-2920±12
E_1	-332±16	-335±12	-314±19	-323±11
E_2	-47±9	-43±6	4±12	1±12
E_3	-3±9	-13±8	5±6	3±3
E_4	–	2±4	–	-1±3
E_a	–	–	117±23	101±23
E_b			83±23	79±23
E_c	-14±11	-16±18	-22±11	-25±13
E_d	51±11	54±11	-11±11	9±23

Table 4.1: Calculated adatom interaction energies (in meV) on Cu(001) and Cu(111). Here E_0 is the energy of introducing an adsorbed adatom on an empty substrate, and E_s is the surface energy per atom, with corresponding units of meV/atom. See Appendix C for a discussion of error bars.

would typically differ because of a difference in **k**-point sampling. Furthermore, the agreement between cells suggests that longer-range interactions are negligible: a different cell size means that adatoms are arranged in a different geometry, which implies that a different number of long-range interactions are ignored. If the long-range interactions are significant, the calculated energies should differ from one cell size to the other. Because they do not differ, the long-range interactions are most likely negligible (unless they happen to cancel each other), confirming our original assumption.

4.2.1 Pair Interactions of Interest

We begin the discussion of our computed lattice-gas energies with the pair interactions. We find E_1 to be the most attractive on both surfaces. This result could be anticipated, since stable adatom islands are often experimentally observed on these surfaces. Furthermore, the strength of the interaction is stronger on Cu(001) than on Cu(111). This result is consistent not only with bond-order-bond-strength arguments[93] applied to the direct part of the interaction (adatoms have six nearest neighbors on Cu(111) compared to four on Cu(001)), but also with the general result for the semiempirical embedded atom method (EAM) formalism that the leading contribution to the indirect (substrate-mediated) part of the interaction is attractive (negative) and proportional to the number of shared NN substrate atoms: two for Cu(001) and one for Cu(111).[43]

Moving on to higher-order interactions, we find E_2 to be a negligible fraction

of E_1 on Cu(111), whereas it is a significant $(1/7)E_1$ on Cu(001). As before, this is consistent with EAM findings; after all, NNN share no substrate atoms on Cu(111), while they share a single substrate atom on Cu(001). Furthermore, this explains why the NN lattice-gas model does not adequately describe the orientation dependence of the step stiffness on Cu(001), as discussed in Chapter 2, but successfully describes the same property on Cu(111).[59,80] In essence, whereas NNN interactions can be ignored in the latter case, they cannot be in the former.

Rounding out our analysis of the pair interactions, we find E_3 and E_4 to be very small on both surfaces, consistent with the agreement between the (3×2) and (4×2) results. (Recall that we did not include E_4 in the (3×2) calculations. Earlier calculations[35] also found E_3 to be essentially negligible on (111).) Notice, however, that even though these interactions are quite small, the general trend $|E_n| > |E_{n+1}|$ is predominantly preserved.

In the only systematic semiempirical investigation of Cu/Cu(001) (or, for that matter, Cu/Cu(111)) pair interactions of which we are aware, Levanov *et al.*[94] found values in remarkably decent agreement: E_1 = -0.32 eV, E_2 = -0.04 eV, and E_3 = +0.01 eV.

4.2.2 Trio Interactions of Interest

We next consider the trio interactions, beginning with the observation that the largest trio interactions E_a and E_b are equilateral triangular in geometry and repulsive in nature, a result which agrees with a similar study on Ag(111)[78]. The

collinear trio, E_c, on the other hand, is attractive and not as significant, being of moderate to small size on both surfaces.

As we discussed earlier, the difference between E_a and E_b can account for the difference in the formation energies of A- and B-steps. Here we find $E_b < E_a$, implying B-steps are energetically more favorable than A-steps. If we further assume, as our calculations suggest, that only E_1, $E_{a/b}$, and E_c are non-negligible interactions (specifically, interactions having a magnitude greater than 5 meV when averaged between the two cell sizes), then from bond breaking arguments, the formation energies per atom of A- and B-steps, E_A and E_B, can be written:

$$E_A = -E_1 - \frac{1}{3}E_a - \frac{2}{3}E_b - 2E_c \tag{4.1}$$

$$E_B = -E_1 - \frac{2}{3}E_a - \frac{1}{3}E_b - 2E_c. \tag{4.2}$$

Notice that $E_A + E_B = -2E_1 - E_a - E_b - 4E_c$, that is, to form an A- and B-step pair, two NN bonds must be broken per atom, along with six trio bonds: one E_a, one E_b, and four E_c (see Fig. (4.4)). Combining Eqs. (4.1) and (4.2) with our results [where we average between the (3×2) and (4×2) cell calculations], we find $E_A \simeq 277 \pm 23$ meV/atom, while $E_B \simeq 267 \pm 23$ meV/atom, so their ratio is $1.04 \pm .12$. These estimates agree with previous results of 0.27 and 0.26 eV, respectively, by Feibelman using a much larger cell.[36] Within error, these estimates also agree with recent semiempirical EAM calculations that found the two values to be 263 and 265 meV,[95] with a ratio consistent with earlier EAM deductions.[96] All these calculations are consistent with measurements by Giesen,[12] who reports ratios of 1.011 and 0.98; controversy remains as to whether the ratio is marginally larger

or smaller than unity. As a whole, this simple lattice gas model appears to be quite successful, then.

We now consider the calculated strengths of the remaining interactions E_d. Although they are relatively small on Cu(111), they are fairly sizable and repulsive on Cu(001). Based on our theory from Chapter 2,[59] we expect E_d to renormalize E_2 on Cu(001) so that $E_2 + E_d \simeq 1/4\ E_1$. Surprisingly, though, we find $E_2 + E_d \simeq 0$! Thus, whereas the inclusion of our calculated attractive E_2 interactions help explain the discrepancy between theory and experiment with regards to the orientation dependence of step-stiffness, the inclusion of our calculated repulsive E_d interactions actually magnify the discrepancy.

Beyond the tabulated interactions, we also estimated the size of more distant

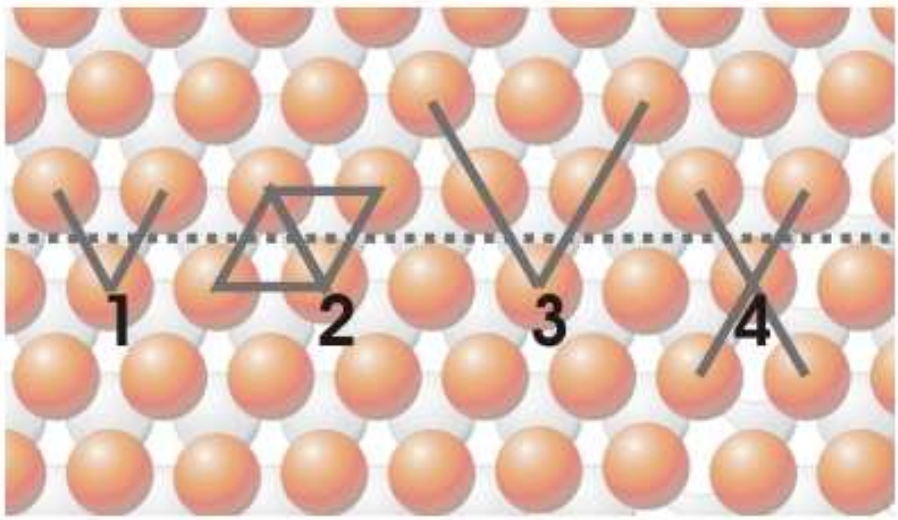

Figure 4.4: When the atoms (dark orange spheres) are separated along the dashed line to create an A- and B-step pair, a number of bonds are broken. In the process, atom 1 shows that two NN bonds (E_1) are broken per atom, atom 2 shows that two NN trio bonds ($E_{a/b}$) are broken per atom, and atoms 3 and 4 show that four collinear trio bonds (E_c) are broken per atom.

neighbor triangular trio interactions on Cu(001) (interactions we could easily include because we calculated the energies of more configurations than unknowns for self-consistency). In particular, we looked at the isosceles triangle trio composed of two NNN legs and a third-nearest-neighbor hypotenuse and the right-triangle trio with one NN leg and one third-nearest-neighbor leg. In both cases, the interaction strengths were nearly zero.

4.2.3 Bulk Energy Per Atom: A Self-Consistency Check

We can obtain the bulk energy per atom E_{bu} from the calculated lattice-gas interaction energies. To do so, we note that an extra layer of atoms in the slab can be thought of as the addition of a bulk layer or an adsorbed layer. In the first case, the additional energy is just the number of atoms N in the new layer times E_{bu}. In the second case, the energy is N times E_0 plus the sum of all significant lateral lattice-gas interaction energies (again, interactions having a magnitude greater than 5 meV when averaged between the two cells). Equating these and dividing by N gives

$$E_{bu} \simeq E_0 + 2E_1 + 2E_2 + 2E_3 + 2E_c + 4E_d, \tag{4.3}$$

for Cu(001) and

$$E_{bu} \simeq E_0 + 3E_1 + E_a + E_b + 3E_c, \tag{4.4}$$

for Cu(111). How well these estimates of E_{bu} agree provides a stringent gauge of self-consistency. Not only are the right-hand-sides of both equations independently equal, but they are independently equal to E_{bu}: a quantity that was, itself,

independently calculated when we determined the slab lattice parameter [using a $(1 \times 1 \times 1)$ supercell sampled with $(11 \times 11 \times 11)$ **k**-points]. There we found E_{bu}=-3763 meV/atom. This agrees quite well (considering the error) with Eqs. (4.3) and (4.4), which give, respectively, E_{bu}=-3741 $\pm$ 48 meV/atom and E_{bu}=-3760 $\pm$ 35 meV/atom [averaged between (3×2) and (4×2) cells]. The self-consistency of these calculations corroborates the general success of the lattice-gas model.

4.2.4 Sensitivity of Trio Interactions to Step Edge Environment

Considering the overall success of our lattice-gas interactions, the repulsive nature of E_d on Cu(001) was unexpected. When this interaction is included into a theory of the orientation dependence of step stiffness, it renormalizes E_2 to zero, effectively making both interactions irrelevant. This leaves the discrepancy between the NN-Ising theory and experiment unresolved.

One possible explanation is that, near steps, adatoms relax out of their well defined lattice-gas positions, thus altering their interactions. Accounting for this would require other significant many-body interactions that make the calculated E_d effective rather than actual. It is interesting to note, for example, that E_{bu} is slightly underestimated by the Cu(001) lattice-gas interactions, suggestive of a too-repulsive E_d.

To further probe this possibility, we systematically recalculated E_d using a larger supercell with a realistic step edge.[47] Our work, described below, shows that trio interactions—unlike their pairwise counterparts—are especially sensitive to their

local environment, complicating a simple lattice-gas description of the surface energetics. In particular, the relaxation of adatoms along steps is large enough to alter the trio interaction strength. We are thus forced to distinguish between "step-edge" trios (with energy E_d^s) and "bulk" trios (with energy E_d^b), as shown in Fig. 4.5a. This distinction is especially important when calculating step properties from a lattice-gas perspective, as we did when calculating the step formation energies and stiffness, as described earlier. For these properties, we count broken step-edge bonds, which, for the trios of interest here, necessarily correspond to E_d^s, not E_d^b. Because relaxation did not play a dominant role in our calculations up to this point, the tabulated E_d must correspond to E_d^b.

To determine the energy difference between E_d^b and E_d^s, we calculated the energies of four distinct adatom configurations, as depicted in Figs. 4.5(b)-(e). In these calculations, we used a relatively large supercell ($4\times4\times14$) and placed adatoms in equivalent positions on the top and bottom of a 5 layer thick slab. Although the slab thickness was smaller than before, we only considered energy differences, so through-substrate interactions always cancelled out. For configurations (b)-(c), we did not allow for lateral relaxation, so the adatoms were fixed in their bulk lateral positions. In this way, the energy difference Δ_1 between the two configurations allowed us to write an estimate for E_d^b in terms of the relevant interactions found in Table 4.1 (where now we replace the tabulated E_d with E_d^b).

$$\Delta_1 = 2(E_0 + E_1 + 2E_2 + 2E_3 + 2E_a + 2E_d^b). \tag{4.5}$$

In a similar way, we calculated E_d^s, but now we allowed all adatoms to fully

relax, as Figs. 4.5(d)-(e) illustrate. Here, arrows give the directions and relative magnitudes of adatom relaxation. Both of these configurations contained a two adatom wide stripe to simulate the local environment of a step edge. When an adatom attaches to such a step, the trio formed relaxes in a fundamentally different way than trios within the step "bulk," as the arrows clearly suggest. As before, the energy difference Δ_2 between the two configurations allowed us to write an estimate

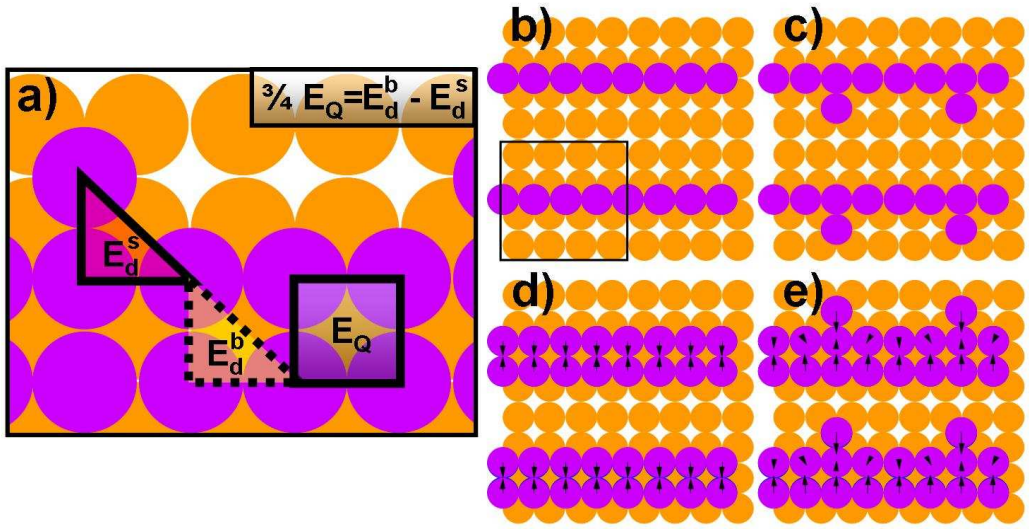

Figure 4.5: In (a), a step-edge trio having energy E_d^s (solid triangle) is distinguished from a bulk trio having energy E_d^b (dashed triangle). Within a lattice-gas framework, these two location-dependent interactions can be replaced by a general $E_d = E_d^s$ and a non-pairwise quarto interaction between four adatoms having energy $E_Q = 4/3(E_d^b - E_d^s)$ (thick, solid square). In (b)-(e), the energy of four adatom configurations were calculated to find E_d^b, E_d^s, and thus, E_Q. The top of the $(4 \times 4 \times 5)$ supercell is shown as a thin, solid line in (b). In (b) and (c), adatoms were laterally fixed in their bulk positions, so E_d^b could be determined by subtracting the energy of configuration (b) from (c). In (d) and (e), on the other hand, adatoms were allowed to fully relax (the arrows give the direction and relative magnitude of the relaxation). Here, the two adatom wide stripe served as a minimal step, so E_d^s could be determined by subtracting the energy of configuration (d) from (e).

for E_d^s in terms of the relevant interactions found in Table 4.1:

$$\Delta_2 = 2(E_0 + E_1 + 2E_2 + 2E_3 + 6E_a + E_c + 2E_d^s). \tag{4.6}$$

By subtracting Eq. (4.5) from Eq. (4.6), we can eliminate the most significant interactions (and thus minimize our error):

$$\Delta_2 - \Delta_1 = 2(E_d^b - E_d^s) + 2E_3 + 4E_4 + E_c. \tag{4.7}$$

Solving this for $E_d^b - E_d^s$ and using our tabulated energies together with our newly calculated energies from configurations (b)-(e) (which, as before, we assume have an associated error of ± 30 meV) , we find

$$E_d^b - E_d^s \approx 40 \pm 8 \text{ meV} \longrightarrow E_d^s \approx 12.5 \pm 10 \text{ meV}. \tag{4.8}$$

We therefore clearly see that trio interactions near step edges have a significantly different interaction than those in the step bulk.

Interactions like E_d^b and E_d^s do not obey the rules of a lattice-gas model because they depend on the local environment. Fortunately, there is a way to distinguish these interactions within a lattice-gas framework. The idea is illustrated in Fig. 4.5a, where we introduce a non-pairwise "quarto" interaction between four adatoms with energy E_Q. Such an interaction would only be a factor for bulk adatoms, distinguishing them from step-edge adatoms. To see how this works, we calculate the energy difference between (1) the three step adatoms connected by the solid triangle and (2) the three bulk adatoms connected by the dashed triangle in Fig. 4.5a. Of course, if we ignore the quarto interaction and distinguish step-edge trios from those in the bulk, then the energy difference is just $E_d^b - E_d^s$. On the other hand, if we

assume there is a general trio interaction $E_d = E_d^s$, then in (1) the energy is just the pairwise interactions plus E_d, while in (2) it is the same pairwise interactions plus $(3/4)E_Q$ (since three adatoms each share 1/4 of the quarto interaction). Equating these two, we have

$$\frac{3}{4}E_Q = E_d^b - E_d^s \;\longrightarrow\; E_Q \approx 53 \pm 11\text{meV}. \tag{4.9}$$

This is a substantial interaction that should not be blithely ignored in future calculations. If we incorporate E_Q into our theory for the (001) step stiffness as described in Chapter 2, then just as we found E_d renormalizes the NN and NNN interactions, we find E_Q only renormalizes the NN interaction. This means that the ratio of the effective NNN interaction E_2^{eff} to the effective NN interaction E_1^{eff} is

$$\frac{E_2^{eff}}{E_1^{eff}} \;=\; \frac{E_2 + E_d}{E_1 + 2E_d + E_Q} \;\leq\; \frac{1}{7}. \tag{4.10}$$

This ratio is actually closer to experimental expectations based on Fig. 2.4 than one would expect based on just the tabulated E_2 and E_1 alone, lending credence to the reality of E_Q.

4.3 Conclusions

We have calculated from first principles a variety of different Cu adatom interaction energies on both Cu(001) and Cu(111). For the most part, our calculations have confirmed our expectations. For the configurations tested, the computed interactions proved robust with respect to small, lateral relaxations of the adatoms: an important requirement for a successful lattice-gas theory. We find E_2 interactions

to be negligible on Cu(111) but significant on Cu(001), explaining why the NN lattice gas model successfully describes the orientation dependence of the Cu(111) step stiffness, but fails for Cu(001) (see Chapters 2 and 3 for details). We have also used our calculated lattice-gas interaction energies to determine the formation energies of Cu(111) A- and B-steps. The resulting estimates for the formation energies agree well with the literature. As expected, we have shown that for Cu on Cu, adatom pair interactions drop off quickly with distance, and only the geometrically smallest trio interactions are relevant. Finally, we have shown that our calculations for the lattice-gas interaction energies are self-consistent and, when taken together, can be used to accurately find the bulk energy per atom E_{bu}.

Among the tabulated results, only E_d seemed to conflict with experimental expectations. It turns out that these interactions (and we might expect other trio interactions as well) are quite sensitive to the lateral relaxation of adatoms near step edges, so extra care was required to determine their strength. Although these kinds of relaxations can confound a simple lattice-gas description of the surface, we have shown that the introduction of a four-adatom, non-pairwise "quarto" interaction can realign experiment and theory.

In closing, first-principle calculations such as the ones described here should prove useful in determining the limits of lattice gas models applied to all sorts of systems. Although we began with expectations based on previous theory and experiment, the consistency of our results shows the problem can be worked in reverse; that is, based on first-principle calculations, we can determine what interactions need to be included in the system to make a successful lattice-gas model.

Chapter 5

Analytic Formulas for the Full Orientation Dependence of Step Stiffness and Line Tension: Key Ingredients for Numerical Modeling

Numerical study of the shape and evolution of layered island structures on surfaces has become an active field.[60,75,97–100] These investigations typically focus on the motion of the island boundaries, which amount to variously oriented single-layer-high steps. Here, as we know well by now, a crucial ingredient in determining the velocity and evolution of steps is the step stiffness $\tilde{\beta}(\theta)$.

If one assumes that step adatoms interact with only nearest-neighbors (NN) or next-nearest-neighbors (NNN), then it is possible to derive exact solutions for the line tension based on the Ising or solid-on-solid (SOS) models. These solutions are implicit [see Eqs. (2.14-2.16) for example], making their implementation into numerical simulations time-consuming and computationally demanding, particularly when dealing with the stiffness, which requires two additional derivatives of the implicit line tension. For simplicity, then, numerical studies often[97–99] (though by no means always[100]) assume an isotropic line tension and stiffness. Except at high temperatures where an island structure is nearly circular, this approximation turns out to be poor, especially near facet orientations. The next simplest approximation assumes a sinusoidal variation reflecting the substrate symmetry.[60] Again, there are shortcomings to this procedure, especially near facet orientations. Such

temperature-independent simplifications allow for only qualitative comparisons with experiment.

In this Chapter we construct expressions for $\beta(\theta)$ and $\tilde{\beta}(\theta)$ that are well behaved analytically, being continuous and twice differentiable, and that give an accurate accounting at all orientations and relevant temperatures. While not especially simple, they are straightforward to construct and easy to implement in numerical codes such as used in finite-element investigations,[101,102] making quantitative comparisons with dynamic experiments possible. We thus expect our results to be widely applicable.

Our approach begins with the simple, low-temperature formulas for the orientation dependence, on face-centered-cubic (fcc) surfaces, of the {001} and {111} stiffness and line tension that we derived in Chapters 1 and 2[59,80] (This approach is rooted in the lattice-gas perspective, so is complementary to Shenoy and Ciobanu's study of stiffness anisotropy based on elasticity theory.[48]) Our formulas assume the step fluctuations are dominated by the rearrangement of geometrically forced kinks—kinks that are not thermally activated. At temperatures low compared to the surface roughening temperature (for noble metal surfaces, such as Ag and Cu, room temperature is considered "low"), the formulas only fail for steps having a negligible number of forced kinks; that is, steps oriented very close to the high-symmetry direction. When the step angle is exactly 0° (aligned with the high-symmetry direction), the formulas predict a cusp in the line-tension and an infinite step stiffness, which is strictly only true at $T = 0$ for two-dimensional islands. Here we correct for the non-analytic behavior by splicing our simple, low-temperature formulas with

small-angle expansions of the exact, implicit solutions based on the Ising and SOS models.

In the following section, we describe the details of a general expansion for the stiffness and line tension that is continuous and twice-differentiable. In sections 5.2 and 5.3, we apply this expansion to fcc {111} and {001} surfaces, respectively, to derive surface-specific formulas for the stiffness and line tension. In section 5.4 we test the derived formulas in state-of-the-art finite-element simulations and in section 5.5 apply them to a simulation of a relaxing Ag step measured via STM. In the final section, we offer concluding remarks as well as a synopsis of the derived expressions.

5.1 Explicit Analytic Approximation

At the microscopic level, the step stiffness and line tension arise from the energy and rearrangement of step edge kinks. It is therefore natural to decompose $\tilde{\beta}(\theta)$ and $\beta(\theta)$ into two contributions: one part originating from geometrically forced kinks and one part from thermally activated kinks (see Chapter 1 for a thorough review). Geometrically forced kinks, depicted in the inset of Fig. 5.1, are present at all temperatures, and give the step an overall orientation θ. The further θ is from the high symmetry direction, the greater the number of geometrically forced kinks. Thus, at lower temperatures, as long as the orientation angle of a step is *greater* than some small, temperature-dependent cross-over angle θ_c, there are many geometrically forced kinks and relatively few thermally activated kinks, suggesting $\tilde{\beta}(\theta)$ and $\beta(\theta)$ can be well described by formulas based on geometrically forced kinks

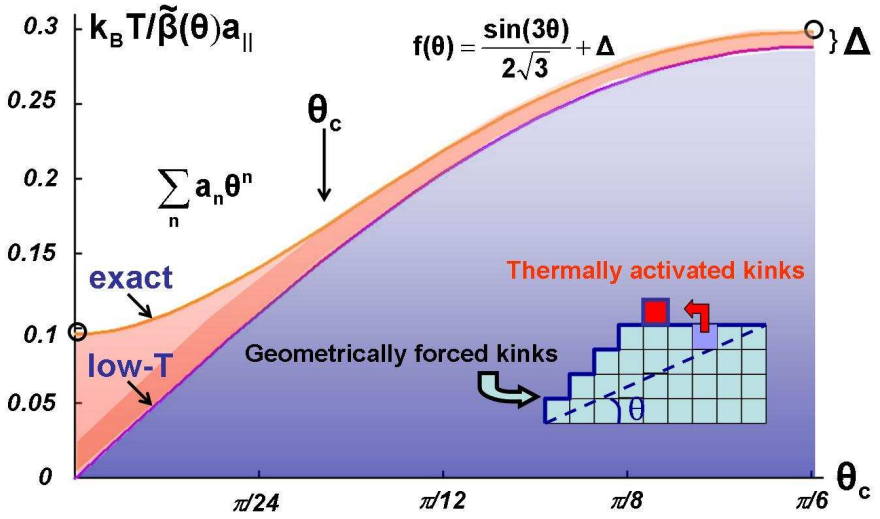

Figure 5.1: The contributions to the step stiffness can be decomposed into parts originating from geometrically forced kinks (lower blue region bounded from above by the line labeled "low-T") and thermally activated kinks (the remaining red region, bounded from above by the line labeled "exact"). At relatively low-temperatures, the {111} step stiffness is well approximated at angles greater than θ_c by a relatively simple, explicit function $f(\theta)$, since the thermal part is evidently insensitive to angle. To account for all angles, the formula can be spliced with a small-angle expansion of the exact NN Ising model solution (from which explicit forms for the stiffness can be obtained at $\theta = 0$ and at $\pi/6$, depicted here by hollow circles). The solution at $\pi/6$ is used to determine Δ. The expansion coefficients a_n are obtained by matching the solutions at $\theta = 0$ and θ_c. The inset depicts a step edge from above. Each square represents an adatom which is part of the step edge. The upper-most square represents a thermally excited adatom, which forms four thermally-activated kinks. The remaining kinks are geometrically forced—they must be present to give the step edge an overall angle θ.

alone.

As an example, in Chapter 3 we derived[59] a remarkably simple, low-temperature formula for the {111} step stiffness assuming only NN adatom interactions and geometrically forced kinks:

$$\frac{k_B T}{\tilde{\beta}(\theta)} \approx \frac{\sin(3\theta)}{2\sqrt{3}}. \tag{5.1}$$

At sufficiently low (but experimentally relevant) temperatures, the formula

works well for steps at nearly all angles, but predicts an infinite stiffness when $\theta = 0$. Fortunately, the exact, implicit solution based on the NN Ising model can be explicitly written for steps having this orientation. We can therefore expand the exact solution about $\theta = 0$ and splice it with our low-temperature solution at θ_c, thereby producing an explicit form for $\tilde{\beta}(\theta)$ valid at all angles. This idea is illustrated in Fig. (5.1). Here, an additional orientation-dependent contribution to the stiffness from thermally activated kinks Δ is also included for completeness. Similar to high-symmetry steps, the stiffness of maximally kinked steps ($\theta = \pi/6$) can be exactly obtained from the NN Ising model, so that Δ can be determined explicitly.

To generalize this approach, we assume $\tilde{\beta}(\theta)$ and $\beta(\theta)$ are well described at angles *greater* than θ_c by simple, analytic functions representing contributions from geometrically forced kinks. Explicit forms for these functions[59,80] will be discussed later. For now, to be general, we simply write them as $f(\theta)$.

At sufficiently low temperatures, θ_c is small, so we may accurately represent $\beta(\theta)$ and the inverse stiffness $\tilde{\beta}^{-1}(\theta)$ at angles *less* than θ_c using small-angle expansions. (We expand the inverse stiffness because, in the θ=0 limit, it vanishes at low temperatures, making it mathematically better behaved than the stiffness itself, which diverges). Specifically, we construct an approximant $X(\theta)$ to represent the dimensionless form of the function we wish to expand—either $\beta(\theta)a_{||}/(k_BT)$ or $k_BT/(\tilde{\beta}(\theta)a_{||})$, where $a_{||}$ is the close-packed distance between atoms (i.e. the atomic

diameter), and k_BT is the Boltzmann energy—we define

$$X(\theta) \;:=\; \begin{cases} \sum_{n=0}^{2N-1} a_n\, \theta^n & \text{if } \theta < \theta_c \\ f(\theta) & \text{if } \theta \geq \theta_c \end{cases}, \tag{5.2}$$

where n is a non-negative integer between zero and an odd integer $2N-1$. To fully specify this function, we must find the appropriate expansion coefficients, a_n. We obtain their values by matching Eq. (5.2) and its higher order derivatives with the exact solutions at θ=0 (which can be systematically obtained) and the approximate (yet accurate) solutions obtained from f(θ) at $\theta = \theta_c$, analogous to performing a spline fit.[103] Specifically, for the boundary conditions at $\theta = 0$, we have

$$a_n \;=\; \frac{\partial_\theta^n X(0)}{n!}, \qquad n < N \tag{5.3}$$

where $\partial_\theta^n X(0) \equiv \partial^n X(\theta)/\partial\theta^n|_{\theta=0}$. The remaining N coefficients are found from the boundary conditions at $\theta = \theta_c$, which form a set of N coupled linear equations:

$$\sum_{n=N}^{2N-1} \frac{n!}{(n-m)!} a_n \theta_c^{n-m} \;=\; \partial_\theta^m f(\theta_c), \tag{5.4}$$

where m is a non-negative integer less than N.

For use in continuum models, $\tilde{\beta}(\theta)$ should be continuous and twice-differentiable. To ensure the second derivative remains continuous at $\theta = \theta_c$, this requires, at minimum, $N = 3$. In this case, Eqs. (5.4) are simultaneously solved to give:

$$a_3 \;=\; \frac{20(f-X) - 8f'\,\theta_c + (f'' - 3X'')\,\theta_c^2}{2\,\theta_c^3} \tag{5.5}$$

$$a_4 \;=\; \frac{-30(f-X) + 14f'\,\theta_c - (2f'' - 3X'')\,\theta_c^2}{2\,\theta_c^4} \tag{5.6}$$

$$a_5 \;=\; \frac{12(f-X) - 6f'\,\theta_c + (f'' - X'')\,\theta_c^2}{2\,\theta_c^5}, \tag{5.7}$$

where the prime represents differentiation with respect to θ; for brevity we write $f \equiv f(\theta_c)$ and $X \equiv X(0)$. Note we have also used Eq. (5.3), which implies $a_0 = X$, $a_1 = X'$, and $a_2 = X''/2$. Because both the line tension and the stiffness are continuous and symmetric about θ=0, we know that $a_1 = X' = 0$. In the remaining sections we apply this approximation to specific cases where explicit forms for X and f can be obtained.

5.2 {111} Surfaces with NN Interactions

For {111} surfaces with only NN adatom interactions, Zia found an implicit form for the full orientation dependence of the step line tension [written earlier in Eq. (3.15)]:[50]

$$\frac{\beta a_{||}}{k_B T} = \eta_0(\theta)\psi_1(\theta, T/T_c) + \eta_-(\theta)\psi_2(\theta, T/T_c), \tag{5.8}$$

where $\eta_0(\theta) \equiv (2/\sqrt{3})\ \sin(\theta)$, $\eta_\pm(\theta) \equiv \cos(\theta) \pm (1/\sqrt{3})\ \sin(\theta)$. Here T_c is the critical temperature of the NN lattice-gas model. The ψ's are solutions of the pair of simultaneous equations for the angular constraint,

$$\frac{\sinh(\psi_1 - \frac{1}{2}\psi_2)\cosh(\frac{1}{2}\psi_2)}{\sinh(\psi_2 - \frac{1}{2}\psi_1)\cosh(\frac{1}{2}\psi_1)} = \frac{\eta_0}{\eta_-}, \tag{5.9}$$

and the thermal constraint,

$$\cosh\psi_1 + \cosh\psi_2 + \cosh(\psi_1 - \psi_2) = \frac{y^2 - 3}{2}, \tag{5.10}$$

where $y \equiv \sqrt{(3z+1)/z(1-z)}$ and $z \equiv 3^{-T_c/T}$. These formulas are, in fact, the same as Eqs. (3.16) and (3.17), only here we modify them slightly for our convenience.

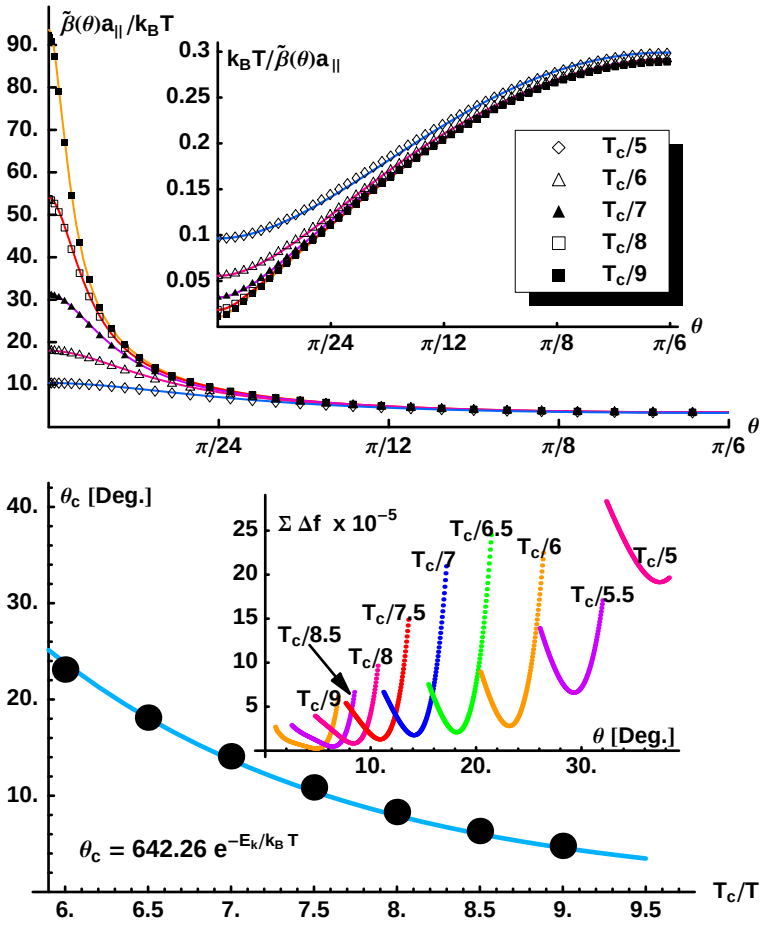

Figure 5.2: In the upper plot, the orientation dependence of our explicit approximation for the {111} step stiffness (solid lines) and its inverse (inset, solid lines) are compared to the exact, implicit solutions (shapes). Because of the six-fold symmetry of the solution, only the positive half of the first sextant is shown (the negative half is mirror-symmetric). The lower plot shows the values used for θ_c (solid dots) in the construction of the left figure and the corresponding exponential fit (solid line), good over the temperature range of interest. The fit is expressed in terms of the kink energy ε_k, which is related to T_c by Eq. (5.11). The inset shows the sum of errors ($\sum \Delta f^2$) versus angle in the least square fit for θ_c. At each temperature, θ_c is the angle that minimizes this sum.

The latter can be rewritten $z \equiv \exp(-2\varepsilon_k/k_BT)$, where ε_k is the energy of a kink on a close-packed step and

$$\frac{\varepsilon_k}{k_BT_c} = \ln\sqrt{3} \tag{5.11}$$

From Eqs. (5.9) and (5.10) it follows that

$$\psi_1(0) = \frac{1}{2}\psi_2(0) = \cosh^{-1}\left(\frac{y-1}{2}\right). \tag{5.12}$$

With $\psi_1(0)$ and $\psi_2(0)$ in hand, we can differentiate the constraints, Eqs. (5.9) and (5.10), set $\theta = 0$, and systematically solve for all the higher order derivatives of the ψ's, which, according to Eq. (5.8), are sufficient to find the higher order derivatives of β. We will utilize these higher order derivatives to derive explicit, analytic approximations for the stiffness and line tension.

5.2.1 Step Stiffness

In this case, $X(\theta) \equiv k_B T/(\tilde{\beta}(\theta) a_{||})$, which is six-fold symmetric for {111} surfaces with only NN adatom interactions. To utilize our explicit analytic approximation, we require $f(\theta)$—the contribution to the reduced stiffness from geometrically forced kinks—which we showed in Chapter 3 takes a relatively simple form in the first sextant ($-\pi/6$ to $\pi/6$):[80]

$$f(\theta) = \frac{1}{2\sqrt{3}}\left(\sin(3\theta) + \frac{3+y^2}{\sqrt{y^4 - 10y^2 + 9}} - 1\right). \tag{5.13}$$

The last two terms, called Δ in Fig. 5.1, are included to ensure $f(\theta)$ matches the exact solution for steps with orientation angle $\theta = \pi/6$. The physical origin of the Δ terms is the thermal fluctuations of a maximally kinked step. Such fluctuations are relatively inexpensive in terms of energy. They dominate the fluctuation contribution while a significant fraction of the step is not close-packed, so that the thermal contribution for such orientations is relatively independent of orientation. Since only the first term has any θ dependence, f' and f'' are simple to calculate.

Now only X and its first two derivatives need to be determined. As mentioned in the preceding section, these can be systematically determined. In particular, we find [see Eq. (3.19) for a derivation of X],

$$X \equiv \frac{k_B T}{a_{||}\tilde{\beta}(0)} = \frac{3(y-1)}{2y\sqrt{y^2-2y-3}}, \tag{5.14}$$

$$X' = 0, \tag{5.15}$$

$$X'' = \frac{y^3-2y^2-15y+36}{2(y-1)\sqrt{y^2-2y-3}}. \tag{5.16}$$

Of course, based on symmetry, we already knew that $X' = 0$.

By combining the functional forms for f and X and their derivatives with Eqs. (5.2-5.7), we can plot the stiffness and compare it to the numerically evaluated exact solution. We show this comparison in Fig. 5.2, where θ_c was determined at a variety of temperatures by doing least square fits to the exact solution. The agreement shown in Fig. 5.2 is very good at low-temperatures and is quite reasonable at temperatures all the way up to $T_c/5$. (This behavior is remarkable since slightly above $T_c/5.5$, θ_c becomes greater than 30°, i.e., the power series is used for the entire range of orientations. Once $|\theta_c| > 30°$, the slope of $k_B T/a_{||}\tilde{\beta}(\theta)$ no longer vanishes at 30°.) At higher temperatures, the angular dependence becomes negligible, so $\tilde{\beta}(\theta)$ become isotropic.

The lower plot in Fig. 5.2 shows the values used for θ_c, along with an exponential fit:

$$\theta_c(T) \approx 642.26(\sqrt{3})^{-T_c/T} = 642.26\exp(-\varepsilon_k/k_B T). \tag{5.17}$$

The Arrhenius decay reflects the importance of thermally-activated kinks for $|\theta| <$

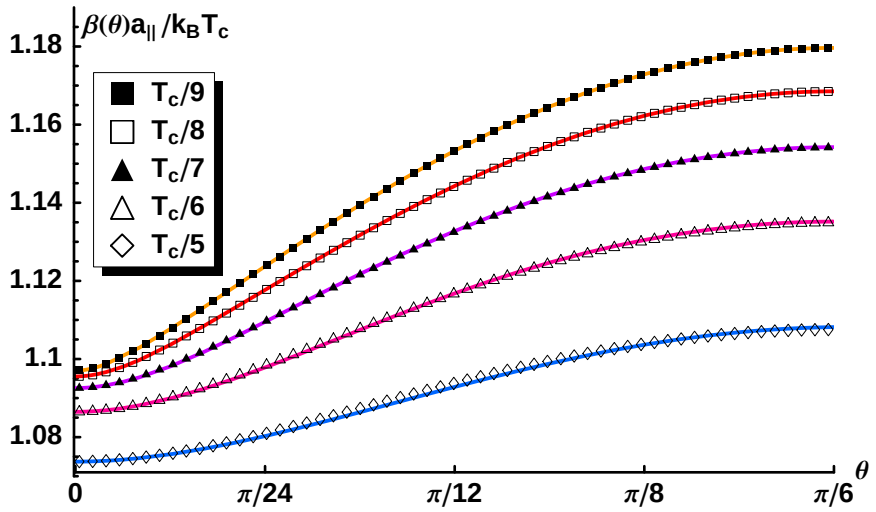

Figure 5.3: The orientation dependence of the explicit approximation for the {111} line tension (solid lines) is compared with the numerically evaluated exact result (shapes). Because of the six-fold symmetry, only the positive half of the first sextant is shown. (The negative half is mirror symmetric.)

θ_c.

5.2.2 Step Line Tension

We follow the same procedure for the line tension. In this case $X(\theta) \equiv \beta(\theta)a_{||}/k_BT$. In Chapter 3 we derived [See Eq. (3.5)] the contribution (in the first sextant) to the line tension from geometrically forced kinks:[59]

$$f(\theta) = -\eta_+ \ln z - \eta_+ \ln \eta_+ + \eta_- \ln \eta_- + \eta_0 \ln \eta_0. \tag{5.18}$$

Just as for the stiffness, we systematically determine X and its first two derivatives

by differentiating the exact solution, Eqs. (5.8-5.12),

$$X \equiv \frac{a_{||}\beta(0)}{k_B T} = 2\cosh^{-1}\left(\frac{y-1}{2}\right), \tag{5.19}$$

$$X' = 0, \tag{5.20}$$

$$X'' = \frac{2y\sqrt{y^2-2y-3}}{3(y-1)} - X. \tag{5.21}$$

The last equation can be rearranged to find the reduced stiffness at $\theta = 0$, as expressed earlier in Eq. (5.14). With these parameters in hand, we compare our approximation for the full orientation dependence of the reduced line tension with the exact, numerically evaluated solution in Fig. 5.3. For the critical angle, we use Eq. (5.17). As before, the fit works remarkably well at temperatures as high as $T_c/5$.

5.3 {001} Surfaces with NN and NNN Interactions

For {001} surfaces with just NN interactions, an exact, explicit form for the full orientation dependence of the line tension was first determined by Abraham and Reed.[49] As we saw in Chapter 2 for Cu(001), however, NNN interactions are often significant,[59] so it is desirable to find a solution including their effects. We denote by R the ratio of NNN to NN adatom interaction strengths; the latter is assumed to be attractive (negative), so a positive R indicatives that the NNN interaction also is.

As in Chapter 2, we rely on the solid-on-solid (SOS) model, which provides an excellent approximation for the line tension and stiffness at reasonable temperatures ($\sim T_c/2$ based on our comparisons with the imaginary path weight random-walk method developed by the Akutsus[21]). In that Chapter, we solved the SOS

model exactly,[59] yielding the following implicit form for the reduced line-tension [just multiply Eq. (2.14) by $\cos\theta$]:

$$\frac{\beta(\theta)a_{||}}{k_BT} = \rho_0(\theta)\sin\theta + g(\rho_0(\theta))\cos\theta, \tag{5.22}$$

where $\rho_0(\theta)$ is found by inverting

$$\tan\theta = \frac{2\sinh\rho_0\sinh S}{(\cosh S - \cosh\rho_0)\left[2\sinh S - (\cosh S - \cosh\rho_0)(y+1)\right]}, \tag{5.23}$$

while $g(\rho_0)$ is

$$g(\rho_0) = S - \ln\left(\frac{y+1}{y-1} + \frac{2}{1-y}\frac{\sinh S}{\cosh S - \cosh\rho_0}\right). \tag{5.24}$$

These last two equations are just Eqs. (2.16) and (A.6) rewritten with $y \equiv 1 - 2z^R$, $S \equiv -(R+1/2)\ln z$, $z \equiv (1+\sqrt{2})^{-2T_c/T} = \exp(-\varepsilon_k/k_BT)$, while T_c is the critical temperature for $R = 0$ (just NN interactions):

$$\frac{\varepsilon_k}{k_BT_c} = \ln(1+\sqrt{2}), \tag{5.25}$$

where the kink energy ε_k now refers to a close-packed step on an {001} surface. We will utilize the exact, implicit solution Eqs. (5.22-5.24) to determine the parameters required to find an explicit approximation for the stiffness and line tension below.

5.3.1 Step Stiffness

To begin, we again let $X(\theta) \equiv k_BT/(\tilde{\beta}(\theta)a_{||})$. The symmetry of {001} surfaces require $X(\theta)$ be four-fold symmetric. We showed in Chapter 2 that the contribution from geometrically forced kinks to the reduced inverse stiffness is well approximated

in the first quadrant ($-\pi/4$ to $\pi/4$) for $|\theta| > \theta_c$ by the following function [see Eq. (2.20)]:[59]

$$f(\theta) = \frac{\sin(2\theta)}{2}\sqrt{1 - y\sin(2\theta)}. \tag{5.26}$$

By differentiating Eq. (5.26), f' and f'' are easily obtained.

To determine X, X', and X'' (and, potentially, any higher order derivatives), we utilize the exact solution of the NNN SOS model. Eq. (5.23), for example, implies that $\rho_0 = 0$ when $\theta = 0$. With some effort, it can be shown that

$$X = \frac{2\sinh S}{(\cosh S - 1)\left[2\sinh S - (\cosh S - 1)(y+1)\right]} \tag{5.27}$$

$$X' = 0 \tag{5.28}$$

$$X'' = \frac{1}{X}\frac{2\cosh S + 1}{\cosh S - 1} - 4\left[\frac{\cosh S - 1}{\sinh S}\frac{y+1}{2} + X\right]. \tag{5.29}$$

As required by symmetry, $X' = 0$.

Combining the functional forms for f, X, and their derivatives with Eqs. (5.2-5.7), we can plot the inverse step stiffness and compare it to the numerically evaluated exact solution, just as before. We show this comparison in Fig. 5.4, where θ_c was determined by doing least square fits to the numerically evaluated exact solution (with $R = 1/5$). The agreement shown in Fig. 5.4 is excellent at low-temperatures and is very reasonable at temperatures all the way up to $T_c/5$, as was the case for the $\{111\}$ solution.

Although it was not initially obvious, the relative size of the NNN interaction R has little effect on θ_c. This fortuitously implies that a single θ_c works for all values of R, as depicted in the lower plots of Fig. 5.4.

With this in mind, the values used for θ_c were determined just as they were

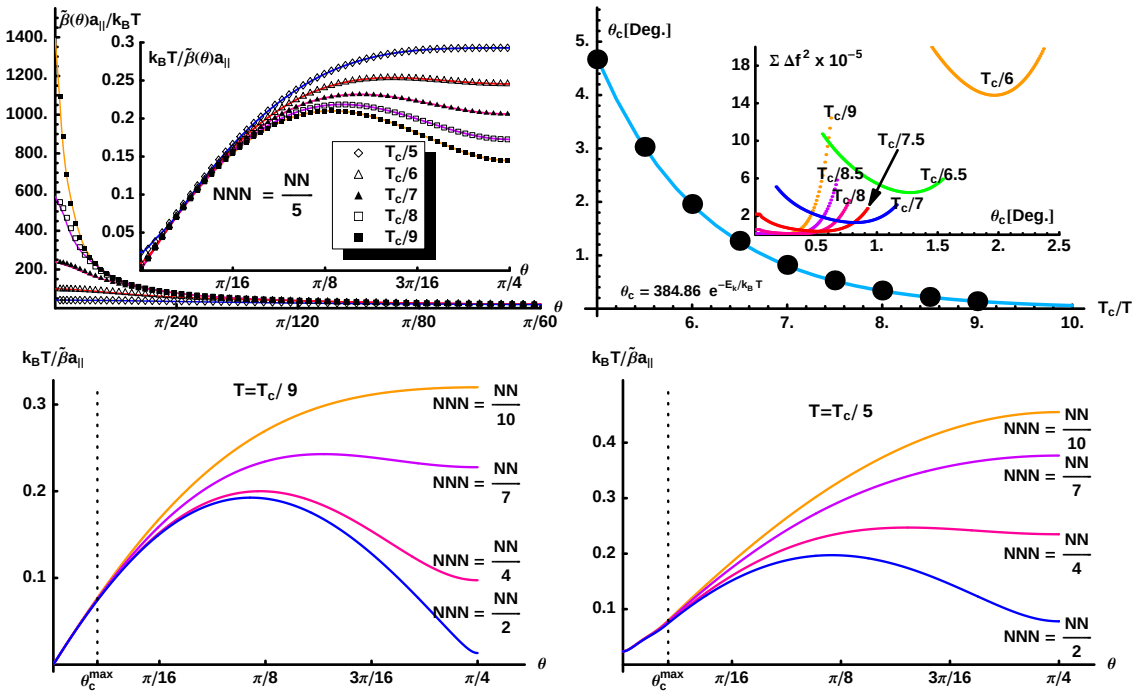

Figure 5.4: In the upper-left plot the orientation dependence of the explicit approximation for the {001} step stiffness (solid lines) and its inverse (inset, solid lines) are compared to the exact, implicit solutions (shapes). Because of the four-fold symmetry of the solution, only the positive half of the first quadrant is shown (the negative half is mirror-symmetric). The upper-right plot shows the values used for θ_c (solid dots) in the construction of the upper-left figure and the corresponding exponential decay fit (solid line) good over the temperature range of interest. The fit is expressed in terms of the kink energy ε_k which is related to T_c by Eq. (5.25). The inset shows the sum of errors ($\sum \Delta f^2$) versus angle in the least square fit for θ_c. At each temperature, θ_c is the angle that minimizes the sum of error. The two lower plots show the {001} inverse stiffness for a variety of different R at two temperatures, $T_c/9$ and $T_c/5$ (the extremum of the temperature range of interest). Notice that for a given temperature, all curves align at an angle greater than the largest critical angle θ_c^{max}. This behavior means θ_c, practically speaking, does not depend on R at these temperatures.

for the {111} case, but with $R = 1/5$. These are shown in the upper-right plot of Fig. 5.4, as well as a simple fit that is accurate over the temperature range of interest:

$$\theta_c(T) \approx 384.86 e^{-\varepsilon_k/k_B T} = 384.86(1+\sqrt{2})^{-T_c/T}. \tag{5.30}$$

Again, the Arrhenius decay is anticipated since θ_c represents the angle below which thermally activated kinks on close-packed segments become important.

Finally, we point out that the {001} step stiffness is much more anisotropic than its {111} counterpart. In fact, at $T_c/6$ the anisotropy is as large as the {111} anisotropy at $T_c/9$. Furthermore, θ_c is less sensitive to temperature than its {111} counterpart. This follows from the relative ease of thermally activating kinks on {111} steps, requiring only the breaking of one NN bond, as compared to two for {001} steps. For {111} steps, then, the angle θ_c below which thermally activated kinks become important is larger than for {001} steps.

5.3.2 Step Line Tension

We proceed as usual, letting $X(\theta) \equiv \beta(\theta) a_{||}/k_B T$. The contribution from geometrically forced kinks is found by solving the low-temperature form of Eq. (5.23), which becomes quadratic in $e^{\rho_0 - S}$. Solving gives

$$e^{\rho_0 - S} = \frac{\sqrt{1 - y\sin(2\theta)} + y\sin\theta - \cos\theta}{(1+y)\sin\theta}. \tag{5.31}$$

Plugging this into Eq. (5.22) yields an excellent approximation $f(\theta)$ for the reduced line tension $X(\theta)$ valid in the first quadrant ($-\pi/4$ to $\pi/4$) for $|\theta| > \theta_c$:

$$f(\theta) = \cos\theta \left[S + \ln \frac{(1-y)\left(\sin\theta + \cos\theta - \sqrt{1-y\sin(2\theta)}\right)}{(1+y)\left(\sin\theta - \cos\theta + \sqrt{1-y\sin(2\theta)}\right)} \right] + \tag{5.32}$$
$$\sin\theta \left[S + \ln \frac{\sqrt{1-y\sin(2\theta)} + y\sin\theta - \cos\theta}{(1+y)\sin\theta} \right]$$

Differentiating twice straightforwardly gives f' and f''. Eq. (5.32) can be written more compactly by defining and inserting $w(\theta, y) \equiv \left[\cos\theta - \sqrt{1 - y\sin(2\theta)}\right] / \sin\theta$, as done in Table 5.1.

This leaves X and its derivatives. They too can be explicitly determined from the exact solution. Setting both $\theta = 0$ and $\rho_0 = 0$ (as Eq. (5.23) demands) in Eq. (5.22), we find X:

$$\begin{aligned} X &= g(0) \\ &= S - \ln\left(\frac{y+1}{y-1} + \frac{2}{1-y}\frac{\sinh S}{\cosh S - 1}\right). \end{aligned} \tag{5.33}$$

Similarly, it can be shown that

$$X' = 0, \tag{5.34}$$

$$X'' = \frac{(\cosh S - 1)[2\sinh S - (\cosh S - 1)(y+1)]}{2\sinh S} - X. \tag{5.35}$$

This last equation can be rearranged to give the reduced step stiffness, as previously written in Eq. (5.27).

By combining the functional forms for f and X and their derivatives with Eqs. (5.2-5.7), we can plot the reduced line tension and compare it to the numerically evaluated exact solution. We show this comparison in Fig. 5.5, where θ_c was determined from Eq. (5.30) and $R = 1/5$ (other values yield equally good agreement). As before, the approximation works well at temperatures up to $T_c/5$ (and, in this case, perhaps even higher).

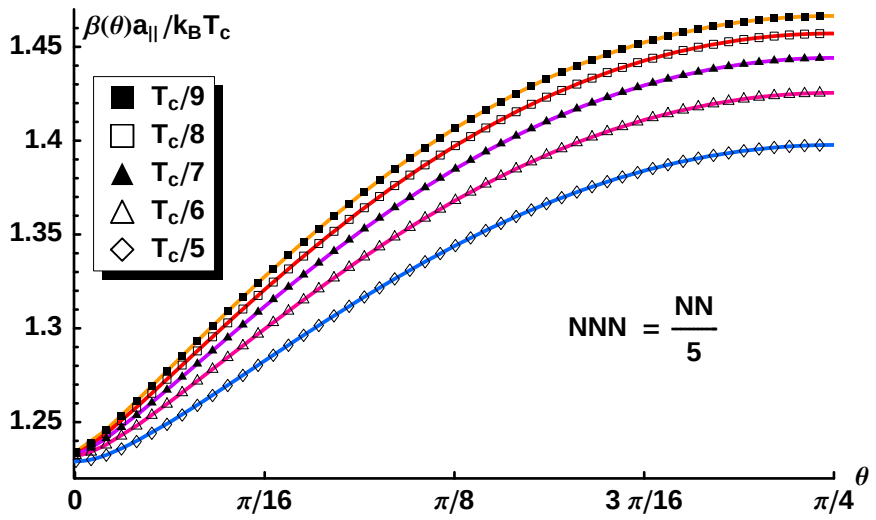

Figure 5.5: The orientation dependence of the explicit approximation for the {001} line tension (solid lines) is compared with the numerically evaluated exact result (shapes). Because of the four-fold symmetry, only the positive half of the first quadrant is shown (the negative half is mirror symmetric).

5.4 Implementation into Simulations

We have recently implemented our formulas into state-of-the-art finite-element simulations.[101,102,104] Here, the equilibrium shape of adatom and vacancy islands was found numerically by determining the surface of constant chemical potential [see Eq. (1.37)]:

$$\mu(\theta, t) = \mathcal{K}(\theta)\ \tilde{\beta}(\theta), \tag{5.36}$$

where $\mathcal{K}(\theta)$ is the step edge curvature. In all simulations, the step stiffness $\tilde{\beta}(\theta)$ was approximated using our derived analytic solutions. Fig. 5.6, for example, shows a variety of simulated islands, both for (111) and (001) surfaces. The first column shows the equilibrium shapes of islands when either the temperatures or the ratios R of NNN to NN interaction strengths is varied. As we expect, based on our

theoretical considerations from Chapter 1, lower temperature islands have sharper corners, whereas higher-temperature islands become ever-more isotropic. Also, for (001) islands, as R approaches unity, the initially rounded squares develop into rounded truncated-squares, reflecting the fact that at $T = 0$ the equilibrium island develops an additional stable facet oriented along fully-kinked directions.

Beyond equilibrium phenomenon, we have also simulated step dynamics. In all such runs, we chose the dominant mass-transport mechanism to be step-edge diffusion. Steps therefore evolved according to Eq. (1.30):

$$v_n(\theta) = \frac{\partial}{\partial s}\left[\frac{\Gamma}{k_B T}\,\frac{\partial \mu(\theta)}{\partial s}\right] = \frac{\Gamma}{k_B T}\frac{\partial^2}{\partial s^2}\left[\mathcal{K}(\theta)\tilde{\beta}(\theta)\right]. \tag{5.37}$$

where v_n is the normal velocity of the step, s is the direction tanget to the step, and Γ is the step-edge adatom mobility, assumed here to be isotropic. The second column of Fig. 5.6 shows sample simulations of island relaxation from initial out-of-equilibrium configurations. Again, the dynamics are consistent with our theoretical expectations. The upper-right figure, for example, illustrates fast relaxation from high-curvature portions of the step.

5.5 A Novel Application: Ag(111) Depinning

Finally, to once again connect our theoretical work with experiment, we are using our simulations to describe the non-equilibrium relaxation of a Ag(111) step recently observed in a novel STM experiment. This step was initially pinned by surface contaminants in a configuration that would normally be highly unfavorable (Fig. 5.7a). During STM scanning, the uppermost pinning point was removed,

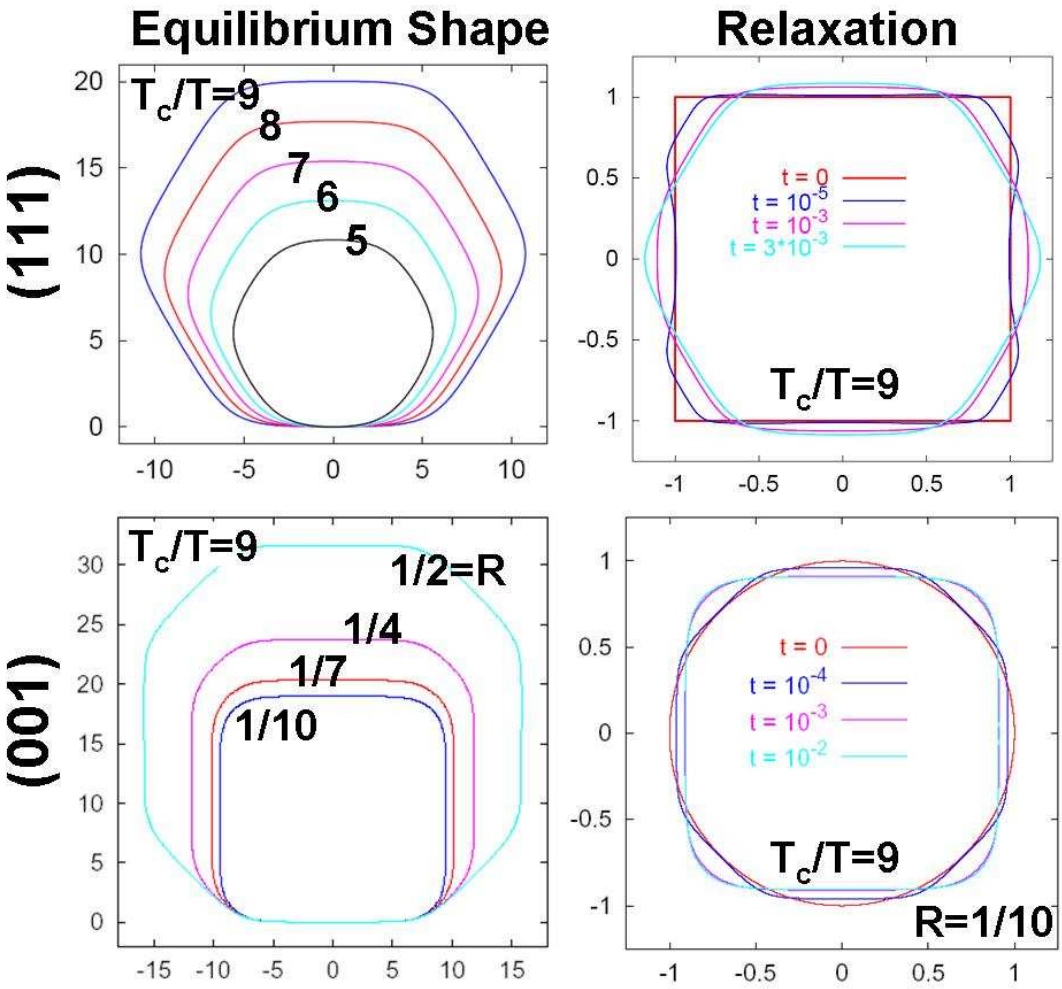

Figure 5.6: Testing the analytic formulas for step stiffness: The top row corresponds to (111) steps, while the bottom row corresponds to (001) steps. In the first column, simulated equilibrium shapes are shown at different temperatures and—for (001) steps—different values of R (the ratio of NNN to NN interaction strength). The island areas are scaled for illustration purposes. In the second column, simulated islands at $T_c/9$ are shown as they relax from initially out-of-equilibrium configurations. The upper island starts as a square, while the lower island starts as a circle.

and the step was thereafter observed to relax to an energetically more favorable configuration (Figs 5.7b-d). At the temperature of observation (413 K, or roughly Tc/6.2), the step kinetics are dominated by the diffusion of adatoms along the step

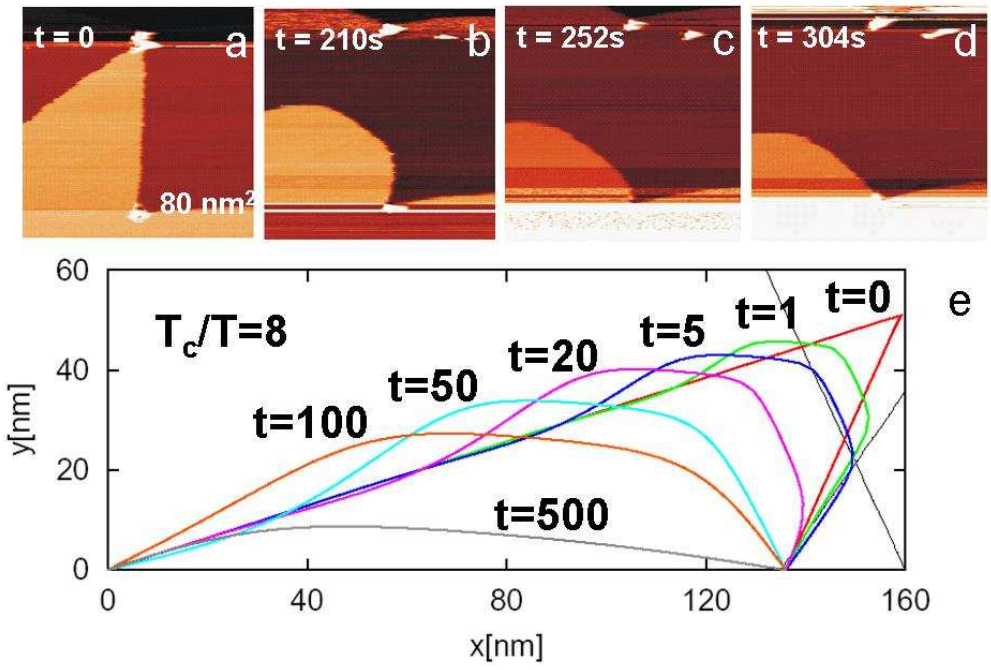

Figure 5.7: The top row shows STM images of a relaxing Ag(111) step initially pinned. In (a) two pinning points (bright white) are shown. As the scanning continued, the top pinning point was removed, and the step was allowed to relax to a new equilibrium configuration (b-d). In (e) preliminary simulation results show qualitative similarities, though, in this case, the adatom mobility was assumed to be isotropic.

edge, so the relaxation is predominantly area preserving. With this in mind, the relaxation can be theoretically described with just two parameters: the step stiffness and the adatom mobility along the step edge, as Eq. (5.37) shows. As discussed in Chapter 1, the higher-order derivates make the step velocity very sensitive to the step stiffness anisotropy, so our derived analytic formulas are especially apt here. In particular, their use will allow us to isolate the effects due to mobility anisotropy.

To date, not much is known about the adatom mobility. Although it was originally believed to be no more anisotropic than the stiffness,[105] recent experiments[68] suggest otherwise. Specifically, analysis of fluctuating Ag(111) steps at

room temperature (Tc/8.2) revealed adatom mobility to be perhaps ten times more anisotropic than step stiffness. To further explore this possibility, we are systematically varying the degree of mobility anisotropy in our simulations to fit the STM measurements of the relaxing Ag(111) step. In the process, we hope to determine (1) the relative degree of stiffness and mobility anisotropy; (2) how step relaxation is affected by this anisotropy; and (3) the origin of mobility anisotropy. Preliminary results, shown in Fig. 5.7e, look promising.

5.6 Summary and Concluding Remarks

We have constructed explicit, twice-differentiable approximants for the full anisotropy of step stiffness and line tension on both {001} and {111} surfaces of fcc crystals. These expressions are accurate over a broad range of experimentally relevant temperatures; they fail only when the stiffness is nearly isotropic, i.e., when their use is no longer required. Implementation into continuum simulations is straightforward and efficient. They are much more usable than numerically extracting solutions from the underlying 6th-order equations, and more flexible and convenient than constructing immense look-up tables as functions of angle and temperature from such a procedure. Our expressions are greatly superior to conventional explicit formulas for step stiffness and line tension, which usually take the form of simple sinusoidal variation that neither carry temperature dependence nor accurately capture the anisotropy (extreme for the step stiffness) observed at lower temperatures. For clarity and convenience, we summarize our results in Table 5.1.

We have implemented these formulas into state-of-the-art finite-element simulations and are currently using them to compare with recent experiments monitoring the relaxation of depinned steps on Ag(111).[106]

EXPLICIT APPROXIMATION FOR STIFFNESS AND LINE TENSION

$$X(\theta) := \begin{cases} \sum_{n=0}^{2N-1} a_n\, \theta^n, & \theta < \theta_c \\ f(\theta), & \theta \geq \theta_c \end{cases}$$

$$a_0 = X \qquad a_3 = \frac{20(f-X)-8f'\ \theta_c+(f''-3X'')\ \theta_c^2}{2\ \theta_c^3}$$

$$a_1 = 0 \qquad a_4 = \frac{-30(f-X)+14f'\ \theta_c-(2f''-3X'')\ \theta_c^2}{2\ \theta_c^4}$$

$$a_2 = \frac{X''}{2} \qquad a_5 = \frac{12(f-X)-6f'\ \theta_c+(f''-X'')\ \theta_c^2}{2\ \theta_c^5}$$

↓	**{111} Surfaces with NN Interactions** $\theta_c = 642.26\ e^{-\varepsilon_k/k_BT}, \quad z = 3^{-T_c/T} = e^{-2\varepsilon_k/k_BT}, \quad y = \sqrt{(3z+1)/z(1-z)}$	
	Stiffness $(X(\theta) \approx k_BT/a_{\|\|}\tilde{\beta})$	**Line Tension** $(X(\theta) \approx a_{\|\|}\beta/k_BT)$
X	$\frac{3(y-1)}{2y\sqrt{y^2-2y-3}}$	$2\cosh^{-1}(\frac{y-1}{2})$
X''	$\frac{y^3-2y^2-15y+36}{2(y-1)\sqrt{y^2-2y-3}}$	$\frac{2y\sqrt{y^2-2y-3}}{3(y-1)} - X$
$f(\theta)$	$\frac{1}{2\sqrt{3}}\left(\sin(3\theta) + \frac{3+y^2}{\sqrt{y^4-10y^2+9}} - 1\right)$	$-\eta_+ \ln(z\eta_+) + \eta_- \ln \eta_- + \eta_0 \ln \eta_0$ *
X	$\frac{2\sinh S}{(\cosh S-1)[2\sinh S-(\cosh S-1)(y+1)]}$	$S - \ln\left(\frac{y+1}{y-1} + \frac{2}{1-y}\frac{\sinh S}{\cosh S-1}\right)$
X''	$\frac{1}{X}\frac{2\cosh S+1}{\cosh S-1} - 4\left[\frac{\cosh S-1}{\sinh S}\frac{y+1}{2} + X\right]$	$\frac{(\cosh S-1)[2\sinh S-(\cosh S-1)(y+1)]}{2\sinh S} - X$
$f(\theta)$	$\frac{\sin(2\theta)}{2}\sqrt{1-y\sin(2\theta)}$	$\cos\theta\left[S+\ln\frac{(1-y)(1+w(\theta,y))}{(1+y)(1-w(\theta,y))}\right]+\sin\theta\left[S+\ln\frac{y-w(\theta,y)}{(1+y)}\right]$ †
↑	**{001} Surfaces with NN and NNN (= R×NN) Interactions** $\theta_c = 384.86\ e^{-\varepsilon_k/k_BT},\ z = e^{-2\varepsilon_k/k_BT} = (1+\sqrt{2})^{-2T_c/T},\ S = (1+2R)\ \varepsilon_k/k_BT,\ y = 1-2z^R$	

*$\eta_\pm \equiv \cos\theta \pm \frac{1}{\sqrt{3}}\sin\theta,\ \eta_0 \equiv \frac{2}{\sqrt{3}}\sin\theta$ †$w(\theta,y) \equiv \cot\theta - \csc\theta\sqrt{1-y\sin(2\theta)}$

Table 5.1: Summary of results for approximants of dimensionless inverse stiffness and line tension. $X \equiv X(0)$, while $f \equiv f(\theta_c)$. The upper part of the table (dark red) refers to the steps on the hexagonal-lattice face, with just NN interactions. The lower part (blue) refers to the square-lattice face; by setting R=0, one retrieves the simpler formulas for just NN interactions.

Chapter 6

Final Summary and Outlook

In this thesis, we have carefully analyzed the origin and nature of step stiffness anisotropy. Although we have approached the subject theoretically, we have consistently relied on experiment for verification. We have furthermore striven to make our results practical, especially for use in simulations, which we hope will ultimately be used to predict and model novel systems. In what follows, we outline some of our key results, as well as discuss remaining questions that should be addressed in future studies.

6.1 Overview

In Chapter 1 we showed that step stiffness is a crucial parameter describing the fluctuations of mesoscopic surface steps within the continuum step model. By focusing on steps, this model provides a natural link between the microscopic movement of atoms and macroscopic surface evolution. The anisotropy (or orientation dependence) of step stiffness reflects the underlying crystalline structure of the surface. At high temperatures, adatoms move in all directions more or less equivalently, so stiffness anisotropy is not significant. At temperatures low with respect to the kink-formation energy, however, adatom movement is easier in some directions than in others, so stiffness anisotropy becomes important. At these relatively low tem-

peratures, the equilibrium shape of adatom and vacancy islands develop nearly flat, faceted edges close to high-symmetry orientations, where the line tension develops sharp peaks that are nearly cusps (see Fig. 1.5). Since the stiffness is related to the line tension through two angular derivatives, as expressed in Eq. (1.1), the stiffness anisotropy is extreme at these temperatures. For many practical solids, such as the noble metals, this is true even at room temperature, because the kink-formation energy is relatively large. When modeling the surfaces of these solids, we must properly treat the inherent anisotropy, especially when working with step stiffness.

In Chapter 1 we also discussed in detail how step stiffness can be conceptually understood from three perspectives. First, the stiffness is a measure for how easily a step thermodynamically bends or fluctuates. This is perhaps the most straightforward way of thinking about step stiffness since, as the name suggests, stiffer steps bend less. This interpretation is summarized in Eqs. (1.5) and (1.14), where we showed that, regardless of the overall step angle, the stiffness is proportional to the energy required to reorient (bend) the step by a small amount.

Alternatively, the step stiffness can be thought of as the "inertia" or "diffusivity" of a step. In both cases, the step itself is considered the time-evolved path of an imaginary particle constrained to move in one dimension. In the first case, the particle is treated classically, and the path is considered continuous. Here, the stiffness is analogous to mass when writing the step free energy per unit length, as Eq. (1.16) demonstrates. From this perspective, just as a very massive particle responds little to driving forces, so too do stiffer steps, regardless of whether the forces originate from other steps or from external sources. Similarly, in the second

case, the particle is treated as a discontinuous random-walker. Here, the stiffness is analogous to the inverse diffusion coefficient, or more traditionally the inverse diffusivity, as Eq. (1.23) demonstrates. Thus, just as a particle with a large diffusion constant moves about quickly, so too does a step with a small stiffness.

In the last part of Chapter 1, we discussed the role of step stiffness within the continuum step model. There we showed that the normal velocity of a step whose movement is driven by the diffusion of adatoms along its edge (periphery diffusion) is proportional to the angular curvature of the step stiffness [see Eq. (1.24)]. Periphery diffusion is dominant at lower temperatures, when adatom detachment from steps is negligible. At these temperatures the stiffness is already extremely anisotropic, so Eq. (1.24) implies the step velocity is even more anisotropic! Again, intimate knowledge of step stiffness anisotropy is crucial.

With this in mind, in Chapters 2-5 we derived and analyzed accurate and practical formulas for the anisotropy of step stiffness. In Chapters 2 and 3 we relied on lattice-gas models to derive remarkably simple formulas for the low-temperature step stiffness on fcc {001} and {111} surfaces, respectively [see Eqs. (2.20) and (3.14)]. On {001} surfaces we showed that the theoretical stiffness anisotropy requires next-nearest-neighbor (NNN) interactions to match experiments on Cu(001). Here we also showed that three adatom, non-pairwise "trio" interactions could significantly affect the stiffness anisotropy and should not be ignored. Interestingly, in Chapter 3 we showed that such higher-order interactions are not required to describe the experimental stiffness anisotropy on Ag and Cu(111) surfaces. In large part, this is because NNNs on {111} surfaces are relatively further apart then they

are on {001} surfaces, thus reducing the direct part of the interaction. Furthermore, unlike their {001} counterparts, NNNs on {111} surfaces do not share any substrate atoms, reducing the indirect part of the interaction as well.

In the second section of Chapter 3, we also derived three low-temperature "theorems." The first states that the derived, low-temperature step stiffness is solely an entropic effect, regardless of the pair interactions (or even the strongest {111} trio interaction) included in the model. This remarkable result even holds true for decorated steps, as we showed at the end of the Chapter. As a consequence, we have our second "theorem," which states that the low-temperature line tension cannot be derived from the stiffness, since the line tension depends on both entropic and energetic effects. Finally, the third "theorem" states that the low-temperature step stiffness can have a higher symmetry then the line tension. Again, this follows from the first theorem, since the energetic component of the line tension—the part that cancels when calculating the stiffness—can have a different symmetry than the entropic component.

To further validate our low-temperature formulas for step stiffness, we used VASP to calculate from first principles the absolute size of a variety of different adatom interactions in Chapter 4. Fig. 4.1 depicts the calculated interactions and Table 4.1 summarizes the results. In particular, we verified the insignificance of NNN interactions on Cu(111) and their significance on Cu(001), providing a consistent picture of step stiffness from a theoretical, experimental, and computational perspective.

Beyond pairwise interactions, we also looked at trio interactions, which turned

out to be significant on both surfaces. Specifically, on Cu(111) we calculated the strengths of the orientation dependent A- and B-trios composed of three NN adatoms. In Chapter 3, we showed how these trios could distinguish between the formation energies of A- and B-steps within a lattice-gas framework. Our calculations [Eqs. (4.1) and (4.2)] are consistent with this conjecture and with the experimentally observed difference between the A- and B-step formation energies. (Although for Cu(111) the difference is too small to distinguish within error. We are currently extending our work to Pt(111),[47] where the experimentally observed difference is larger.)

On Cu(001) we calculated the strength of the trio composed of three adatoms forming a NN hypotenuse triangle. As we discussed in Chapter 2, this trio can renormalize the NN and NNN interactions, and therefore significantly affect the step stiffness, as Eq. (2.27) shows. Surprisingly, our original calculations yielded a repulsive trio that renormalized the NNN interaction to zero, leaving the discrepancy between the theoretical and experimental step stiffness unresolved. More careful analysis, however, revealed the trio interaction is sensitive to adatom relaxation. In particular, trios near step edges, which are the relevant ones when calculating the step stiffness from lattice gas broken bonds, are less repulsive than those within the step "bulk." Of course, this description is inconsistent with a lattice-gas framework, where one assumes adatoms always sit in high-symmetry positions. We therefore introduced a non-pairwise, four-adatom "quarto" interaction that could distinguish step-edge trios from "bulk" trios, as Eq. (4.9) demonstrates.

In Chapter 5, we extended our low-temperature formulas for step stiffness so

that they can be used efficiently within simulations. Because our low-temperature formulas were derived by considering the action of geometrically forced kinks alone, they always failed below a small, temperature-dependent critical angle θ_c. (Steps below this angle have virtually no forced kinks, so their movement is dominated by thermal kinks.) To compensate for this shortcoming, we combined our formulas (via a spline fit) with small-angle expansions of the exact solutions based on the Ising or SOS models. The end result was a set of continuous, twice-differentiable, analytic formulas for both the line-tension and stiffness, summarized in Table 5.1. These formulas were furthermore tested in finite-element simulations, as illustrated in Fig. 5.6. Most recently, we have used these simulations to model a depinned Ag(111) step at room-temperature, where the dominant mass-transfer mechanism is periphery diffusion. For such a system, the simulation only requires two parameters: the step stiffness and the step-edge mobility. By matching simulations to experiment and utilizing our accurate formulas for step stiffness, we hope to isolate the mobility and determine its anisotropy, which intriguingly has recently been measured to be roughly ten times that of the stiffness.[68]

In short, we have derived many useful formulas for the anisotropy of step stiffness. Of the derived results, perhaps the most promising is the formula for the line tension of Ag(111) steps decorated by C_{60}, as expressed in Eq. (3.33). To derive the formula, we focused on the possible positions the C_{60} could sit along the step edge. The decorated step free energy was then just a function of these positions. This idea should be extendable to many other heteroepitaxial systems. In our case, it allowed us to determine the equilibrium shape of decorated islands, from which we

estimated the size of the C_{60}-Ag interaction energy [see Eq. (3.36)]. With this, we could write the line tension as a function of a single variable: the C_{60}-C_{60} interaction energy. This interaction had little effect on the shape of the decorated islands, so we estimated its magnitude by studying the island fluctuations [see Eq. (3.40)]. To our knowledge, these are the first estimates of their kind.

6.2 Outlook for the Future

In our analysis of step stiffness anisotropy, we have always assumed that steps are in equilibrium, at least locally. (Equilibrium concepts, such as step chemical potential and the thermodynamic limit may apply, for example, to a small yet macroscopic piece of a larger system not fully in equilibrium.) Of course, this assumption is not always true. For example, our formulas are most applicable at low temperatures, but at these temperatures it may take a long time for systems to fully relax. Impurities can also complicate matters, as we saw at the end of Chapter 5 when modeling Ag steps initially pinned in what would normally be far-from-equilibrium positions. When applying our derived formulas to such non-equilibrium systems, care should therefore be taken. For these systems, even formulas connecting step velocity and step stiffness, such as Eq. (1.24), are potentially problematic. After all, these formulas are all based on the Gibbs-Thompson relation linking the step chemical potential with the local adatom concentration [see Eq. (1.37)]. When such a system is pushed far from equilibrium, the relationship will at some point fail, as will our formulas for step stiffness. Exactly how and under what conditions the

failure occurs should be more carefully addressed and quantified in the future.

Another issue that deserves more attention is how long-range interactions originating from surface strain affect step stiffness anisotropy. Our formulas were all derived using lattice-gas models containing, at most, interactions involving nearest and next-nearest-neighbors (this includes the trio and quarto interactions we discussed). Step-step interactions are long-range, however, and become very significant when the density of steps increases. These interactions will certainly modify our formulas. For heteroepitaxial systems, lattice-mismatch induced strain will further modify our formulas. As spearheaded by Ciobanu and Shenoy,[48] future work should study the relative size of these effects and quantify their importance.

Finally, more work should be done extending the ideas presented in this thesis to other, more novel systems, such as the Ag steps decorated by C_{60} discussed at the end of Chapter 3. Quantifying how molecules such as C_{60} alter surface step properties can provide more than just energetic information; it can also link the symmetry of a molecule with its effect on the shapes of surface features. Further quantifying effects like these will undoubtedly prove useful when engineering microscopic surface structures in the future.

Appendix A

{001} Stiffness: Calculational Details

A.1 Leading Term in Low-Temperature Expansion

In this appendix we discuss the lowest-order correction to the ground state entropy of the step running from the origin to an arbitrary particular point. We can rewrite Eq. (2.2) as

$$Z_\theta = g_{M,N}(0)e^{-E_0/kT}\left[1+\frac{g_{M,N}(1)}{g_{M,N}(0)}e^{-\Delta E/kT}+...\right]. \tag{A.1}$$

Then, assuming the exponential is small, we have

$$F \approx E_0 - k_BT\left\{\ln[g_{M,N}(0)]+\frac{g_{M,N}(1)}{g_{M,N}(0)}e^{-2\varepsilon/k_BT}\right\}. \tag{A.2}$$

A combinatorial analysis[16,18,107] shows that

$$g_{M,N}(1) = \binom{M+N}{M-1}(M+1)+\binom{M+N}{N-1}(N+1) \tag{A.3}$$

Then Eq. (2.4) generalizes to

$$\begin{aligned} F &\approx E_0 - k_BT\left[(M+N)\ln(M+N) - M\ln M - N\ln N\right. \\ &\quad \left. +e^{-2\varepsilon/k_BT}\frac{M^3+N^3}{MN}\right]. \end{aligned} \tag{A.4}$$

A.2 Partition Function

To carry out the sum in Eq. (2.8), we consider the Fourier transform of $Z(Y)$:

$$\begin{aligned} W(\mu) &\equiv \int_{-\infty}^{\infty} dY\ e^{i\mu Y} Z(Y) \\ &= \sum_{\{\Delta\}} \exp \sum_{j=1}^{L} \left(i\mu\Delta_j - K(\Delta_j)\right) \\ &= \left[\sum_{\Delta=-\infty}^{\infty} \exp\left(i\mu\Delta - K(\Delta)\right)\right]^L, \end{aligned} \tag{A.5}$$

where $K(\Delta) \equiv (V + H|\Delta| + U|\Delta - 1| + D|\Delta + 1|)$ is the energy in Eq. (2.7), associated with adjacent columns with height difference Δ. Carrying out the summation in Eq. (A.5) gives

$$\frac{g(i\mu)}{k_B T} \equiv -\frac{1}{L} \ln W(i\mu) = V + U + D - \ln B(i\mu), \tag{A.6}$$

where

$$B(i\mu) \equiv 1 + \frac{e^{2D}}{e^{H+U+D+i\mu} - 1} + \frac{e^{2U}}{e^{H+U+D-i\mu} - 1}. \tag{A.7}$$

Thus, the original partition function $Z(Y)$ is:

$$\begin{aligned} Z(Y) &= \frac{1}{2\pi} \int_{-\infty}^{\infty} d\mu\ e^{-i\mu Y} W(\mu) \\ &= \frac{1}{2\pi} \int_{-\infty}^{\infty} d\mu\ \exp\left[L\left(-i\mu \tan\theta - \frac{g(i\mu)}{k_B T}\right)\right] \end{aligned} \tag{A.8}$$

For $L \gg 1$, we can evaluate this inverse transform by steepest decent approximation. The saddle point occurs on the imaginary axis ($\mu = -i\rho$), at the value ρ_0 given by the stationary-phase condition:

$$-\frac{g'(\rho_0)}{k_B T} = m \equiv \tan\theta. \tag{A.9}$$

Calculating the derivative from Eqs. (A.6) and (A.7), we find

$$m = B'(\rho_0)/B(\rho_0), \tag{A.10}$$

where prime stands for ∂_ρ. The leading contribution to this integral (A.8) is just the integrand evaluated at this point:

$$Z(Y) \approx \exp\left[-L\left(m\rho_0 + \frac{g\left(\rho_0\right)}{k_B T}\right)\right]. \tag{A.11}$$

A.2.1 Analysis of $g''(\rho)$ and specialization to $U = D$

From Eqs. (A.6), we find

$$\frac{g'\left(\rho\right)}{k_B T} = -B'(\rho)/B(\rho) \tag{A.12}$$

and

$$\frac{g''\left(\rho\right)}{k_B T} = -B''(\rho)/B(\rho) + \left[B'(\rho)/B(\rho)\right]^2. \tag{A.13}$$

This can be simplified, by Eq. (A.10), to

$$\frac{g''\left(\rho_0\right)}{k_B T} = -mB''(\rho_0)/B'(\rho_0) + m^2, \tag{A.14}$$

the quantity needed for computing the stiffness as a function of m. While straightforward, computing the derivatives with the general form for B (Eq. (A.7) with $\rho = i\mu$) is quite tedious. A slight simplification emerges if we specialize to the physically relevant case $U = D$. Then, with $S \equiv H + 2D$, we have

$$\begin{aligned} B(\rho) &= 1 + \frac{e^{2D}}{e^{S+\rho} - 1} + \frac{e^{2D}}{e^{S-\rho} - 1} \\ &= 1 - e^{2D} + \frac{e^{2D}\sinh S}{\cosh S - \cosh \rho} \\ &\equiv 1 - e^{2D} + \frac{e^{2D}\sinh S}{C(S,\rho)}, \end{aligned} \tag{A.15}$$

so that

$$B'(\rho) = e^{2D} \sinh S \frac{\sinh \rho}{C^2(S,\rho)}, \tag{A.16}$$

and

$$B''(\rho) = e^{2D} \sinh S \left[\frac{\cosh \rho}{C^2(S,\rho)} + \frac{2 \sinh^2 \rho}{C^3(S,\rho)} \right]. \tag{A.17}$$

Inserting these expressions into Eq. (A.10), we have

$$m = \frac{\sinh \rho_0 \sinh S}{C(S,\rho_0) \left[\sinh S - C(S,\rho_0) \left(1 - e^{-2D} \right) \right]}. \tag{A.18}$$

Similarly, with Eq. (A.14), we find

$$\frac{g''(\rho_0)}{k_B T} = -m \left[\frac{2 \sinh \rho_0}{C(S,\rho_0)} + \coth \rho_0 \right] + m^2. \tag{A.19}$$

Appendix B

{111} Stiffness: Calculational Details

B.1 Leading Term in Low-Temperature Expansion

For the triangular lattice we find important differences from the square lattice for the higher-order terms. Specifically, we consider how $g(1)$ changes. In contrast to $g(0)$, we cannot simply replace M and N with M' and N'. There is no one-to-one correspondence between paths of energy $\mathcal{E}_1$ on a square lattice and those of energy $\mathcal{E}_1^{\Delta}$ on a triangular lattice. This failed correspondence for higher terms follows from the observation that $\mathcal{E}_1^{\Delta}$-configurations are only one link longer than $\mathcal{E}_0^{\Delta}$-steps, whereas E_1-configurations are two links longer than $\mathcal{E}_0$-steps: $\mathcal{E}_{n+1}^{\Delta} - \mathcal{E}_n^{\Delta} \equiv \Delta\mathcal{E}^{\Delta} = \varepsilon$, or

$$\mathcal{E}_n^{\Delta} = \varepsilon \left(\frac{2N}{\sqrt{3}} + 2M + n \right), \; n = 0, 1, 2, ..., \tag{B.1}$$

Hence, we require a separate combinatorial analysis.

We imagine a step of energy $\mathcal{E}_1$ in the first sextant. Such a step (see Fig. B.1) will have either: (1) $(M'+1)$ links oriented at $0°$ (denoted "X-links"), $(N'-1)$ links oriented at $60°$ (denoted "Y-links"), and one link oriented at $120°$ (denoted "Υ-links"), or (2) $(M'-1)$ links oriented at $0°$, $(N'+1)$ links oriented at $60°$, and one link oriented at $-60°$. In the first case, the problem can be reworded as follows: how many ways to arrange an $(M'+N'+1)$-lettered word with $(M'+1)$ X's, $(N'-1)$ Y's, and one Υ. In the second case, the problem is the same, only with M and N switched. Thus, the solution of this traditional combinatorial problem gives the

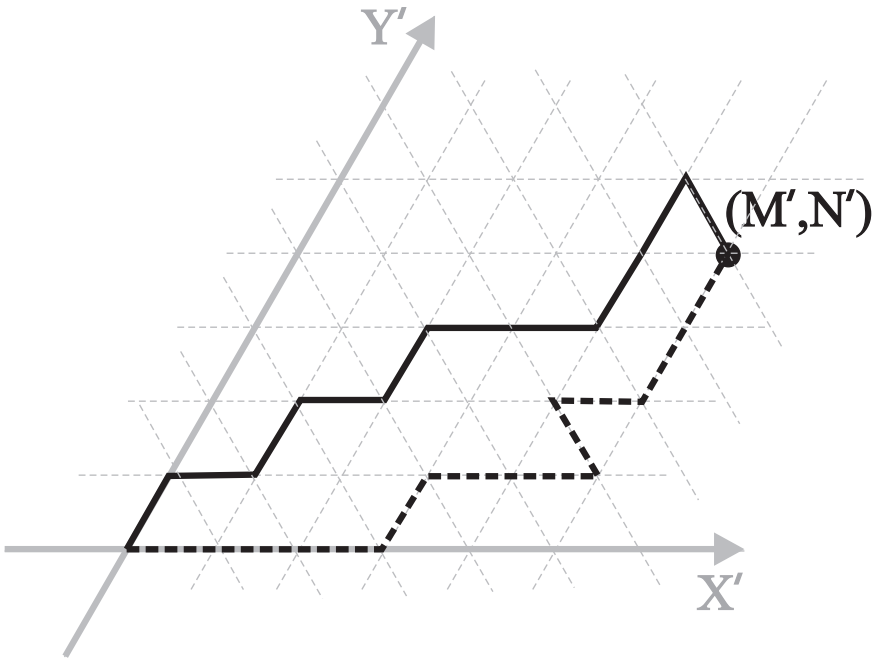

Figure B.1: Two equivalent steps having energy $\mathcal{E}_1^{\triangle}$. The dashed step contains $(M'+1)$ X-links, $(N'-1)$ Y-links, and one Υ-link, while the solid step contains $(M'-1)$ X-links, $(N'+1)$ Y-links, and one Υ-link.

total number of next-to-shortest paths $g^{\Delta}(1)$:

$$g^{\Delta}(1) = \binom{M'+N'+1}{M'+1} N' + \binom{M'+N'+1}{N'+1} M'. \tag{B.2}$$

With $g^{\Delta}(0/1)$ and $\mathcal{E}_n^{\Delta}$ in hand, we can write the low-temperature partition function expansion for a triangular lattice. Using Eq. (2.3) and expanding the logarithm as in Eq. (A.2), we have

$$F \approx \mathcal{E}_0^{\Delta} - k_B T \left\{ \ln[g(0)] + \frac{g^{\Delta}(1)}{g(0)} e^{-\Delta\mathcal{E}^{\Delta}/k_B T} \right\}. \tag{B.3}$$

Taking the thermodynamic limit (M', $N' \gg 1$) and using Stirling's approximation gives

$$\begin{aligned} \ln M\!F &\approx E_0^{\Delta} - k_B T \left[(M'+N') \ln(M'+N') - M' \ln M' - N' \ln N' \right. \\ &+ \left. e^{-\varepsilon/k_B T} \frac{M'^3 + N'^3 + M'N'^2 + N'M'^2}{M'N'} \right]. \end{aligned} \tag{B.4}$$

The pair of cross-factors in the last coefficient are absent in Eq. (A.4) for the square lattice.

The correction term becomes non-negligible when the final term in Eq. (B.4) becomes of order unity. At low T this occurs only near close-packed directions, so for small values of θ. In this regime, to lowest order in θ, $N' = (2L/\sqrt{3}) \sin\theta \to 2L\theta/\sqrt{3}$ and $M' = L\cos\theta - N'/2 \to L$. Then the critical value of θ is

$$\theta_c^{(\beta)} \approx \tfrac{\sqrt{3}}{2} e^{-\varepsilon/k_B T} = \tfrac{\sqrt{3}}{2} z^{1/2}. \tag{B.5}$$

Specifically, based on Eq. (B.5) and using $\varepsilon \approx 0.12$ eV for Cu{111}, we find that $\theta_c^{(\beta)}$ is 0.353°, 3.18°, and 5.51° for T/T$_c$ of 1/9, 1/5, and 1/4, respectively. As clear from Fig. 3.3, this criterion turns out to underestimate the values for θ_c obtained

in Section II.D, mainly because Eq. (B.5) was derived from an expression for $\beta(\theta)$ instead of $\tilde{\beta}(\theta)$ (which should depend more sensitively on θ). over the plotted thermal range.

B.2 Exact Formulas for Line Tension and Stiffness in Mirror Directions

B.2.1 General results for all orientations

In this appendix, we derive Eqs. (3.18) – (3.21) for the mirror-line directions $\theta = 0°$ and $\theta = 30°$ from Zia's implicit exact solution.[50]

To begin, because $\tilde{\beta} = \beta + \beta''$ (where the prime represents differentiation with respect to θ), it follows from Eq. (3.15) that

$$\frac{\tilde{\beta} a_{||}}{k_B T} = 2\eta_0' \psi_1' + 2\eta_-' \psi_2' + \eta_0 \psi_1'' + \eta_- \psi_2''. \tag{B.6}$$

We can simplify Eq. (B.6) by finding relationships between the various derivatives of the ψ's. Differentiating Eq. (3.17) with respect to θ, regrouping, and using Eq. (3.16), we get

$$\psi_1' \eta_0 + \psi_2' \eta_- \;\; = \;\; 0. \tag{B.7}$$

Differentiating again yields

$$\psi_1'' \eta_0 + \psi_2'' \eta_- + \psi_1' \eta_0' + \psi_2' \eta_-' \;\; = \;\; 0. \tag{B.8}$$

Using Eq. (B.8), we rewrite the last part of Eq. (B.6) (containing ψ_1'' and ψ_2'') in terms of just ψ_1' and ψ_2'. Then, using Eq. (B.7) we eliminate ψ_2' in favor of ψ_1'. We

are then left with an equation relating $\tilde{\beta}$ to only ψ_1':

$$\frac{\tilde{\beta} a_{||}}{k_B T} = \left(\eta_0' - \eta_-' \frac{\eta_0}{\eta_-} \right) \psi_1' = \frac{2\psi_1'}{\sqrt{3}\cos\theta - \sin\theta}. \tag{B.9}$$

For general angle, we must evaluate ψ_1' numerically. However, for the two high-symmetry directions we can obtain analytic results that allow us (with the aid of Eq. (3.15) for β) to write explicit expressions for $\tilde{\beta}$, as presented in the next two subsections.

B.2.2 Results for $\theta = 0°$

At $\theta = 0°$, Eq. (3.15) reduces to

$$\frac{\beta a_{||}}{k_B T} = \psi_2(0), \tag{B.10}$$

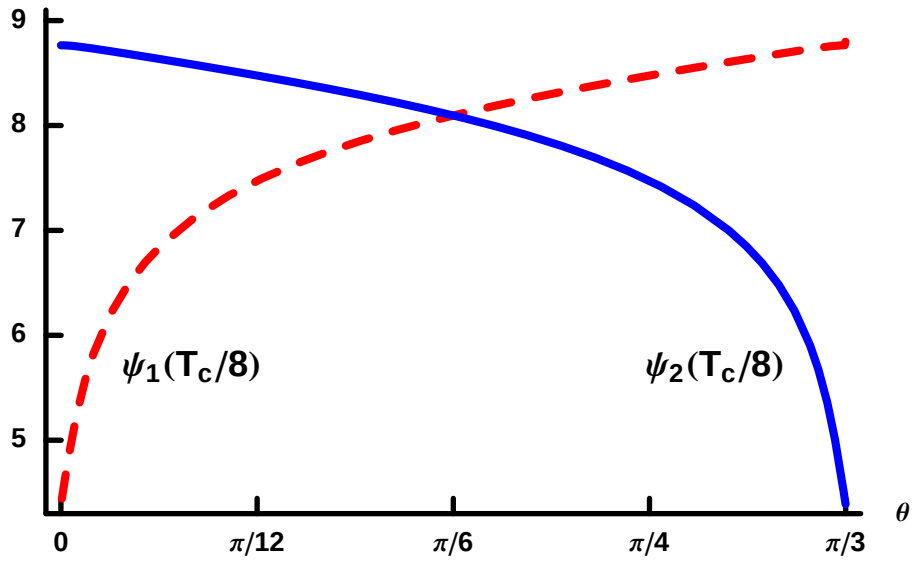

Figure B.2: Numerical evaluation of ψ_1 (dashed red curve) and ψ_2 (solid blue curve) as functions of angles at temperature $T_c/8$ equivalent to room temperature for the experimental systems Cu and Ag {111}. Note that the linear behavior near one limit and the divergent slope near value zero at the other. At higher temperatures the curves are qualitatively similar but progressively smaller in magnitude.

assuming that $\psi_1(0)$ is finite. Furthermore, near $\theta = 0°$, Eq. (3.16) can be inverted and the sinh's combined to get

$$\frac{\sinh(\psi_1 - \frac{1}{2}\psi_2)\cosh(\frac{1}{2}\psi_2)}{\sinh(\psi_2 - \frac{1}{2}\psi_1)\cosh(\frac{1}{2}\psi_1)} = \frac{2}{\sqrt{3}}\,\theta. \tag{B.11}$$

For Eq. (B.11) to hold at $\theta = 0°$,

$$\psi_2(0) = 2\psi_1(0). \tag{B.12}$$

Eq. (3.17) therefore becomes:

$$2\cosh\psi_1(0) + \cosh(2\psi_1(0)) = f. \tag{B.13}$$

Solving this for $\cosh\psi_1(0)$ and taking the positive root, we find:

$$\cosh\psi_1(0) = \cosh(\tfrac{1}{2}\psi_2(0)) = \tfrac{1}{2}(-1 + \sqrt{3 + 2f}), \tag{B.14}$$

consistent with the assumption of finite $\psi_1(0)$. Solving for $\psi_2(0)$ and combining with Eq. (B.10) yields Eq. (3.18).

Correspondingly for $\tilde{\beta}$, at $\theta = 0°$ Eq. (B.9) becomes

$$\frac{\tilde{\beta}(0)a_{\|}}{k_B T} \;=\; \frac{2}{\sqrt{3}}\psi_1'(0), \tag{B.15}$$

while Eq. (B.7) becomes

$$\psi_2'(0) = 0, \tag{B.16}$$

provided $\psi_1'(0)$ is finite. We obtain $\psi_1'(0)$ by differentiating Eq. (B.11) with respect to θ and then setting $\theta = 0°$ so that Eqs. (B.12) and (B.16) apply. This give

$$\psi_1'(0) = \tfrac{1}{\sqrt{3}}\tanh\psi_1(0)[1 + 2\cosh\psi_1(0)]. \tag{B.17}$$

By combining this with Eq. (B.14) for $\cosh\psi_1(0)$, we see that $\psi_1'(0)$ is indeed finite, as we earlier assumed. Thus, Eq. (B.15) becomes Eq. (3.19), as desired.

B.2.3 Results for $\theta = 30^\circ$

At $\theta = 30^\circ = \pi/6$, Eq. (3.15) becomes

$$\frac{\beta(\pi/6)a_{\|}}{k_B T} = \frac{1}{\sqrt{3}}\left[\psi_1(\pi/6) + \psi_2'(\pi/6)\right]. \tag{B.18}$$

Furthermore, near $\theta = \pi/6$, $\eta_0/\eta_- \approx 1 + 2\sqrt{3}\ \Delta\theta$, where $\Delta\theta \equiv \theta - \pi/6$. Inverting Eq. (3.16) we therefore have

$$\frac{\sinh\psi_1 + \sinh(\psi_1 - \psi_2)}{\sinh\psi_2 - \sinh(\psi_1 - \psi_2)} \approx 1 + 2\sqrt{3}\ \Delta\theta, \tag{B.19}$$

By inspection, at $\theta = \pi/6$ ($\Delta\theta = 0$), one solution to this equation is just

$$\psi_2(\pi/6) = \psi_1(\pi/6). \tag{B.20}$$

Plugging this result into Eq. (3.17) and solving for $\psi_2(\pi/6)$ gives,

$$\cosh\psi_2(\pi/6) = \frac{f-1}{2}. \tag{B.21}$$

Combining this with Eq. (B.18) (where we now know $\psi_1(\pi/6) = \psi_2(\pi/6)$) results in Eq. (3.20).

As for $\tilde{\beta}$, at $\theta = \pi/6$, Eq. (B.9) becomes

$$\frac{\tilde{\beta}a_{||}}{k_B T} = 2\psi_1'(\pi/6), \tag{B.22}$$

while Eq. (B.7) becomes

$$\psi_1'(\pi/6) = -\psi_2'(\pi/6). \tag{B.23}$$

Like before, we can find $\psi_1'(\pi/6)$ by differentiating Eq. (B.19) with respect to θ. Taking the result and setting $\theta = \pi/6$, so that Eqs. (B.20) and (B.23) apply, gives

$$\psi_1'(\pi/6) = \frac{\sqrt{3}\sinh\psi_1}{\cosh\psi_1 + 2}. \tag{B.24}$$

Finally, we combine this result with Eq. (B.21) for $\cosh\psi_2(\pi/6) = \cosh\psi_1(\pi/6)$ and Eq. (B.22), to get Eq. (3.21), as desired.

B.3 Rederivation of Eq. (3.14) from exact solution

In this appendix, we re-derive Eq. (3.14) directly from the exact solution for $\beta(\theta)$ given in Eqs. (3.16) and (3.17). To do so, we just assume $\cosh\psi_2 \gg \eta_-/\eta_0$ (remember that η_-/η_0 decreases from ∞ at $\theta = 0°$ to 1 at $\theta = 30°$, so that, between these angles, this condition also implies that $\cosh\psi_2 \gg 1$). In this case, Eq. (3.16) can be solved to give

$$\cosh\psi_1 \approx \frac{\eta_0}{\eta_-}\cosh\psi_2. \tag{B.25}$$

Thus, if $\cosh\psi_2 \gg \eta_-/\eta_0 > 1$, then $\cosh\psi_1 \gg 1$. We show here that these assumptions for $\cosh\psi_{1,2}$, together with the low-temperature replacement of $f(z)$ by $1/(2z)$ in Eq. (3.17), are enough to derive Eq. (3.14).

When $\cosh\psi_{1,2} \gg 1$, then $\cosh\psi_{1,2} \approx \sinh\psi_{1,2} \approx e^{\psi_{1,2}}/2$. With these approximations, Eqs. (3.16) and (3.17) become remarkably simple:

$$e^{\psi_1} + e^{\psi_2} = 2f(z), \tag{B.26}$$

$$e^{\psi_2} = \frac{\eta_-}{\eta_0}e^{\psi_1}. \tag{B.27}$$

Solving this pair of equations for e^{ψ_1} and e^{ψ_2} gives

$$e^{\psi_1} = \frac{2f(z)\eta_0}{\eta_0+\eta_-}, \qquad e^{\psi_2} = \frac{2f(z)\eta_-}{\eta_0+\eta_-}. \tag{B.28}$$

If we then replace $f(z)$ by its low-temperature limit, $1/(2z)$, Eq. (3.15) becomes

$$\frac{\beta a_{||}}{k_B T} = \eta_0 \ln\left[\frac{\eta_0}{z(\eta_0+\eta_-)}\right] + \eta_- \ln\left[\frac{\eta_-}{z(\eta_0+\eta_-)}\right]. \tag{B.29}$$

By noting $\eta_0 + \eta_- = \eta_+$, and using the definition for z, Eq. (B.29) can be easily simplified to Eq. (3.5), from which Eq. (3.14) for $\tilde{\beta}$ was derived.

By deriving the approximation given in Eq. (3.5) (and thus Eq. (3.14)) in this way, we can determine when the approximation becomes invalid. Specifically, we require $\cosh\psi_{1,2} \gg 1$. As we showed, the more restrictive of these inequalities is the one involving $\cosh\psi_1$, since $\cosh\psi_1$ is necessarily smaller than $\cosh\psi_2$ in the first sextant by a factor of η_0/η_- (which is less than 1). Thus, the main assumption is $\cosh\psi_1 \gg 1$, which, from Eq. (B.28), is just

$$\frac{2f(z)\eta_0}{\eta_0+\eta_-} \gg 1. \tag{B.30}$$

The solution to this equation, which we call θ_2, is given by the following inequality:

$$\cot\theta_2 \ll \frac{4f-1}{\sqrt{3}}. \tag{B.31}$$

Because $\cot\theta$ decreases from ∞ at $\theta = 0$ to $1/\sqrt{3}$ at $\theta = \pi/6$, we know that angles in the first sextant that are greater than θ_2 will also satisfy the inequality in Eq. (B.31).

Thus, Eqs. (3.5) and (3.14) are valid in the first sextant at all angles above θ_2.

Appendix C

Evaluating Lattice Gas Interactions: Numerical Details

In Table 4.1 energies are listed with error bars. Here, the source of error was predominantly due to interactions between adatoms through the substrate. Whereas increasing the slab thickness would have reduced this error, the required computational time would have increased significantly.[86] Instead, we effectively reduced error by averaging results over a set of self-consistent calculations. More precisely, we calculated the energies of more adatom arrangements than were necessary to solve for the interaction energies of interest. By choosing different sets of arrangements to solve for the same interaction energies, we could self-consistently check our results while at the same time estimate error. Typically, interaction energies changed little from one set of arrangements to another, though differences could be on the order of 10-30 meV. We therefore assumed each total energy calculation carried an error of 30 meV. With this assumption, the propagation of error was easily calculated.

As an example, using the first six adatom arrangements shown in Fig. 4.2, we could simultaneously solve the corresponding six equations for the six interaction energies of interest. Assuming the six configurations correspond to energies $\xi_i \pm 30$ meV, i=1,2,. . .6, then, for example, E_1 is

$$E_1 = \frac{1}{12}(5\xi_0 - 10\xi_1 + 2\xi_2 + \xi_4 + 4\xi_5 + 2\xi_6), \tag{C.1}$$

where ξ_0 corresponds to the energy of the slab without any adatoms. The error in

this estimate is therefore

$$\triangle E_1 = \frac{1}{12}\sqrt{5^2 + 10^2 + 2^2 + 1 + 4^2 + 2^2}\ \triangle E \tag{C.2}$$

$$= 1.02\ \triangle E, \tag{C.3}$$

where $\triangle E \equiv 30$ meV. Similarly, solving for E_2 gives

$$E_2 = \frac{1}{4}(\mathcal{E}_0 - 2\mathcal{E}_1 + \mathcal{E}_4), \tag{C.4}$$

with corresponding error

$$\triangle E_2 = \frac{1}{4}\sqrt{1 + 2^2 + 1}\ \triangle E \tag{C.5}$$

$$= 0.61\ \triangle E. \tag{C.6}$$

Continuing in this way, we estimated the error of all the calculated interaction energies of interest. We then repeated the process for different sets of six arrangements of adatoms. Of course, different sets yield different errors. By averaging over results from sets of arrangements with the least error (which inevitably agreed the most), we reduced the error even further.

One potential danger of using this method of error analysis is the presence of systematic error that doesn't average to zero. Of course, were this the case, we would expect all calculated interaction energies to be systematically renormalized by an error-dependent, fixed amount. Considering we have calculated many interaction energies to be approximately zero, we know that the systematic error is most likely negligible. Furthermore, we estimated E_{bu} in two ways: first, using Eqs. (4.3) and (4.4), and, second, using a single-atom, bulk supercell that contains neither adatoms nor a substrate. Because the two ways of calculating E_{bu} are so dissimilar, we can

safely assume systematic error, if any exists, is different between the two. Because the two estimates agree remarkably well, the systematic error again is most likely negligible.

Appendix D

Notation Guide

θ: angle between step tangent and step high-symmetry, close-packed direction

θ_c: critical step angle below which thermal kinks are important

T: temperature

T_c: NN Ising model critical temperature

k_B: Boltzmann's constant

t: time

Ω: adatom projected area

$a_{||}$: distance between adatoms parallel to step edge

m: step slope

ρ: step "torque", or conjugate variable to m

$F(\theta)$: step free energy

$\beta(\theta)$: step line tension, or step free energy per unit length

$\tilde{\beta}(\theta)$: step stiffness

$G(\rho)$: Andreev step free energy

$g(\rho)$: Andreev step free energy per unit length

$x(y)$: Maryland notation for step position.

$\Gamma(\theta)$: adatom mobility

$\mathcal{K}(\theta)$: step curvature

$c(\theta)$: adatom concentration

$v_n(\theta)$: normal step velocity

$\mathcal{E}$: step energy

ε: Ising parameter, or energy of severed half of lattice-gas NN bond

ϵ: lattice-gas bond energy

$E_i, i = 1, 2, 3...$: VASP calculated adatom pairwise interaction energy

$E_x, x = a, b, c, d$: VASP calculated adatom trio interaction energy

E_Q: VASP calculated adatom quarto interaction energy

Appendix E

Mathematica Notebooks

Here we provide images of two mathematica notebooks created to analyze the C_{60} data presented at the end of Chapter 3. The first notebook, surfacePhysicsModules.nb, includes a number of useful surface physics programs, including code for finding the step correlation function. The second notebook, c60fluxForThesis.nb, relies on the first. It includes code for determining the position of individual C_{60} from STM images, as well as code for performing the analysis of island step-edge fluctuations. The actual files are available upon request.

Useful Surface Physics Modules

This notebook contains functions useful in surface physics.

FUNCTIONS

■ Step Auto-Correlation Function

■ Definition:

```
AutoCor::usage = "AutoCor[{x1,x2,x3,...xn}] returns the
    step auto-correlation function G(j) = <(x(i+j)-xi)^2>, where <>
    denotes an average over i, and both i and j are between 1 and n.";
AutoCor[peri : {_?NumericQ..}] := Module[
  {i, j, cor = 0, corList = {}},
  For[j = 1, j ≤ Length[peri], j++,
   For[i = 1, i ≤ Length[peri] - j, i++, cor = (peri[[i + j]] - peri[[i]])^2 + cor;
   ];
   If[Length[peri] - j ≠ 0,
    cor = cor/(Length[peri] - j)];
   corList = Append[corList, cor];
  ];
  corList
 ];
```

■ Sample Usage:

To see how the function works, simply type:

```
? AutoCor
```

```
AutoCor[{x1,x2,x3,...xn}] returns the step auto-correlation function G(j) = <(xi+j-
  xi)^2>, where <> denotes an average over i, and both i and j vary between 1 and n.
```

The function will only work on a list of numerical values, as shown below:

```
AutoCor[1]
```

```
AutoCor[1]
```

```
Clear[a, b, c];
AutoCor[{a, b, c}]
```

```
AutoCor[{a, b, c}]
```

Here we test the function on a few simple lists:

```
AutoCor[{1, 1, 1, 1, 1, 1, 1}]
```

```
{0, 0, 0, 0, 0, 0, 0}
```

```
AutoCor[Table[i, {i, 0, 100}]] // LogLogListPlot;
```

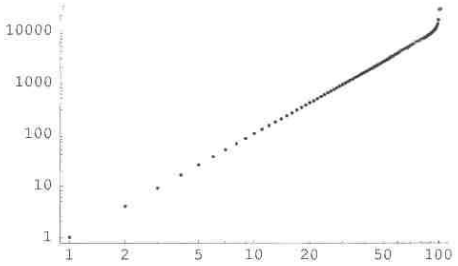

■ Step Auto-Correlation Average Function

■ Definition:

```
AutoCorAvg[periArr:{{_?NumericQ..}..}] :=
   Module[{i, j, corAvg = 0, corArr},

    (*Find correlation function for each perimeter in periArr*)
     corArr = Table[AutoCor[periArr[[i]]],
        {i, 1, Length[periArr]}];

     (*Average these correlation function together*)
     Plus @@ corArr/Length[corArr]];

AutoCorAvg::usage =
  "AutoCorAvg[{{x1,x2,x3,...xn},{y1,y2,...yn},..}] returns an equally weighted
    average of the step auto-correlation function list G(j) = {<(xi+j-
    xi)^2>,<(yi+j-yi)^2>,..}, where <> denotes an average
    over i, and both i and j are between 1 and n.";
AutoCorAvg[periArr : {{_?NumericQ..}..}] :=
  Module[{i, j, corAvg = 0, corArr},

    (*Find correlation function for each perimeter in periArr*)
    corArr = Table[AutoCor[periArr[[i]]], {i, 1, Length[periArr]}];

    (*Average the list and output*)
    Plus @@ corArr / Length[corArr]
  ];
```

```
AutoCorAvg::usage = "AutoCorAvg[{{\!\(x\_1\),\!\(x\_2\),\!\(x\
\_3\),...\!\(x\_n\)},{\!\(y\_1\),\!\(y\_2\),...\!\(y\_n\)},..\
}] returns an equally weighted average of the step \
auto-correlation function list G(j) = {<(\!\(x\_\(i + \
j\)\)-\!\(x\_i\)\!\(\()\^2\)\)>,<(\!\(y\_\(i + \
j\)\)-\!\(y\_i\)\!\(\()\^2\)\)>,..}, where <> denotes an \
average over i, and both i and j are between 1 and n.";
AutoCorAvg[periArr:{{_?NumericQ..}..}] :=
   Module[{i, j, corAvg = 0, corArr},
    corArr = Table[AutoCor[periArr[[i]]],
       {i, 1, Length[periArr]}]; Plus @@ corArr/
     Length[corArr]];
```

■ Sample Usage:

To see how the function works, simply type:

```
? AutoCorAvg
```

```
AutoCorAvg[{{x1,x2,x3,...xn},{y1,y2,...yn},..}] returns an equally weighted average
  of the step auto-correlation function list G(j) = {<(xi+j-xi)^2>,<(yi+j-yi)^2>,..},
  where <> denotes an average over i, and both i and j are between 1 and n.
```

The function will only work on a list of numerical values, as shown below:

```
AutoCorAvg[1]
```

```
AutoCorAvg[1]
```

```
Clear[a, b, c];
AutoCorAvg[{a, b, c}]
```

```
AutoCorAvg[{a, b, c}]
```

Here we test the function on a few simple lists:

```
AutoCor[{3, 4, 3, 4, 3, 4, 3}]
```

$$\left\{1, \frac{1}{5}, \frac{21}{20}, \frac{7}{20}, \frac{47}{40}, \frac{47}{40}, \frac{47}{40}\right\}$$

```
AutoCor[{1, 1, 1, 1, 1, 1, 1}]
```

```
{0, 0, 0, 0, 0, 0, 0}
```

```
AutoCorAvg[{{3, 4, 3, 4, 3, 4, 3}, {1, 1, 1, 1, 1, 1, 1}, {3, 4, 3, 4, 3, 4, 3}}]
```

$$\left\{\frac{2}{3}, \frac{2}{15}, \frac{7}{10}, \frac{7}{30}, \frac{47}{60}, \frac{47}{60}, \frac{47}{60}\right\}$$

■ Roughness

■ Definition:

```
Roughness::usage =
  "Roughness[{x1,x2,x3,...xn},{x1_,x2_,x3_,...,xn_}] returns the interface
    width, or roughness R = 1/n Sum_{i=1}^{n} Sqrt[(xi - xi_)^2]. If {x1_,x2_,x3_,...,xn_} is
    absent, it returns R = 1/n Sum_{i=1}^{n} Sqrt[(xi - x̄)^2], where x̄ is the average of xi.";
Roughness[peri : {_?NumericQ..}] := Module[{avg, intWidthList = {}},
   avg = Plus @@ peri / Length[peri];
   Print["Average value = ", avg];
   temp2 = Sqrt[(peri - avg)^2];
   Plus @@ temp2 / Length[temp2]
   ];
Roughness[peri : {_?NumericQ..}, eqPeri : {_?NumericQ..}] :=
  Module[{intWidthList = {}},
   temp2 = Sqrt[(peri - eqPeri)^2];
   Plus @@ temp2 / Length[temp2]
   ];
```

■ Sample Usage:

```
? Roughness
```

```
Roughness[{x1,x2,x3,...xn},{x1_,x2_,x3_,...,xn_}] returns the
  interface width, or roughness R = 1/n Sum_{i=1}^{n} Sqrt[(xi - xi_)^2]. If {x1_,x2_,x3_,...,xn_}
  is absent, it returns R = 1/n Sum_{i=1}^{n} Sqrt[(xi - x̄)^2], where x̄ is the average of xi.
```

Roughness only works on the proper type of input:

```
Roughness[{a, b}, 1]
```

```
Roughness[{a, b}, 1]
```

```
Roughness[1]
```

```
Roughness[1]
```

```
Roughness[{1, 1, 1, 1, 1, 1, 1}]
```

```
Average value = 1
```

```
0
```

```
Roughness[{1, 2, 1, 1, 1, 1, 1}] // N
```

Average value = $\frac{3}{7}$

```
0.244898
```

```
Roughness[Table[i, {i, 0, 100}]] // N
```

```
Average value = 50

25.2475
```

If the equilibrium perimeter is present, you can input it as in the following example:

```
Roughness[{1, 2, 3, 4, 5, 6, 7, 8}, {2, 2, 2, 2, 2, 2, 2, 2}] // N
```

```
2.75
```

C_{60}/Ag(111) Decorated Step Analysis

This notebook shows how the STM images of the C_{60} decorated Ag(111) islands were analyzed.

FUNCTIONS

■ Reading Images

```
ReadC60[filename_String] :=
  Module[{test = {}, testb = {}, testc = {}, pos = {}, pos2 = {}, center},
   test = Import[filename, "List"] // Partition[#, 2] &;
   testb = Transpose[test];
   testc = testb[[2]];
   pos = Transpose[{Mod[testc, 512], IntegerPart[testc / 512]}];
   center = Mean[pos];
   pos2 = Plus[#, -center] & /@ pos
  ];

ReadC60256[filename_String] :=
  Module[{test = {}, testb = {}, testc = {}, pos = {}, pos2 = {}, center},
   test = Import[filename, "List"] // Partition[#, 2] &;
   testb = Transpose[test];
   testc = testb[[2]];
   pos = Transpose[{Mod[testc, 256], testc / 256}];
   center = Mean[pos];
   pos2 = Plus[#, -center] & /@ pos
  ];
```

■ Finding C60

```
FindC60[poslist_, del_, out_String] :=
 Module[{rpos = {}, rpos2 = {}, rpos3 = {}, mylist = {}, mylist2 = {},
   mysublist = {}, final = {}, finala = {}, cart = {}, avg, flag, add, i, j, k},
  (*CONVERT TO POLAR COORDINATES*)
  rpos = Table[{Sqrt[poslist[[i, 1]]^2 + poslist[[i, 2]]^2] // N,
     360/(2 Pi) ArcTan[poslist[[i, 1]] // N, poslist[[i, 2]]]}, {i, 1, Length[poslist]}];
  (*SELECT ALL POINTS WITHIN A DEGREE (+/- del) FOR ALL ANGLES*)
  rpos2 =
   Table[{i, Select[rpos, i - del < #[[2]] < i + del &]}, {i, -179.5, 179.5, 2 * del}];
  (*DETERMINE HOW MANY POINTS WITHIN EACH DEGREE BIN*)
  rpos3 = Table[{rpos2[[i, 1]], Length[rpos2[[i, 2]]]}, {i, 1, Length[rpos2]}];
  (*FIND AVERAGE NUMBER OF POINTS IN EACH BIN... THIS WILL BE CUTOFF*)
  avg = Mean[rpos3][[2]] // N;
  (*GROUP ALL POINTS IN EACH BIN USING CUTOFF AS SEPARATOR FOR BINS*)
  mylist = {};
  flag = 1;
  For[i = 1, i ≤ Length[rpos3], i++,
   If[rpos3[[i, 2]] > avg,
     mysublist = Append[mysublist, rpos3[[i]]],
     mylist = Append[mylist, mysublist];
     mysublist = {};
     flag = 1;
    ];
  ];
  mylist = Append[mylist, mysublist];
  mylist2 = DeleteCases[mylist, {}];
  (*AVERAGE POINTS IN EACH BIN*)
  For[i = 1, i ≤ Length[mylist2], i++,
   For[j = 1, j ≤ Length[mylist2[[i]]], j++,
    finala = Append[finala, Select[rpos2, #[[1]] = mylist2[[i, j, 1]] &][[1, 2]]  ];
   ];
   final = Append[final, Mean[finala // Flatten // Partition[#, 2] &] ];
   finala = {};
  ];
  (*Checks to see if first and last parts are part of the same C60... if so,
   average*)
  If[Abs[final[[Length[final], 2]] - 360 - final[[1, 2]]] < 2,
   add = {(final[[Length[final], 1]] + final[[1, 1]])/2,
     (final[[Length[final], 2]] + 360 + final[[1, 2]])/2};
   final = Drop[final, -1];
   final = Drop[final, 1];
   final = Append[final, add]
  ];
  (*CONVERT BACK TO CARTESIAN COORDINATES*)
  cart = Table[{final[[i, 1]] Cos[final[[i, 2]] * 2 Pi/360],
```

```
    final[[i, 1]] Sin[final[[i, 2]] * 2π/3^n]}, {i, 1, Length[final
  (*EXPORT TO FILE AND OUTPUT POINTS*)
  Export[out, cart // N, "Table"];
  cart
 ];
```

■ Fitting 1 pt per degree or so for C60

```
FluxC60[poslist_, del_, out_String] :=
 Module[{rpos = {}, rpos2 = {} , final = {}, cart = {}, cart2 = {}, center , i, j, k},
  (*CONVERT TO POLAR COORDINATES*)
  rpos = Table[{√(poslist[[i, 1]]^2 + poslist[[i, 2]]^2) // N,
     360/(2π) ArcTan[poslist[[i, 1]] // N, poslist[[i, 2]]]}, {i, 1, Length[poslist]}];

  (*SELECT ALL POINTS WITHIN A DEGREE (+/- del) FOR ALL ANGLES*)
  rpos2 =
   Table[{Mean[Select[rpos, i < #[[2]] < i + del &]][[1]], i}, {i, -180, 180 - del, del}];
  final = rpos2;
  (*CONVERT BACK TO CARTESIAN COORDINATES*)
  cart = Table[{final[[i, 1]] Cos[final[[i, 2]] * 2π/360],
     final[[i, 1]] Sin[final[[i, 2]] * 2π/360]}, {i, 1, Length[final]}];
  (*EXPORT TO FILE AND OUTPUT POINTS*)
  Export[out, cart // N, "Table"];
  cart
 ];
```

■ Equilibrium Island Shape: EqShape[edge, imgN, pixN, fac]

```
EqShape[edge_, imgN_, pixN_, fac_] :=
 Module[{n, i, exList = {}, nedge = {}, nedge2 = {}, ecs1 = {}},
  nedge = Table[edge[[i]] / Mean[edge[[i]]], {i, 1, Length[edge]}];
  nedge2 = Take[nedge, imgN];
  ecs1 = Plus @@ nedge2 / imgN;
  exList = Table[fac i, {i, 1, pixN / fac}] // Partition[#, 1] &;
  Extract[ecs1, exList]
 ];
```

■ Fluctuation Analysis: FModes[edge, {img1,imgN}, pixN, fac, color]

```
FModes[T_, edges_, {img1_, imgN_}, pixN_, fac_, color_] :=
  Module[{edges1 = {}, edges2 = {}, ftedges = {}, ftedges2 = {},
    exList = {}, pixN2, eqshape = {}, kb = 8.617385 * 10^-2 (*meV/K*),
    ravg = 0, fptable = {}, fptable1 = {}, fptable2 = {}, file},
   eqshape = EqShape[edges, imgN, pixN, fac];
   exList = Table[fac i, {i, 1, pixN / fac}] // Partition[#, 1] &;
   edges1 = Table[Extract[edges[[i]], exList], {i, 1, Length[edges]}];
   medges1 = Mean /@ edges1;
   ravg = Mean[medges1];
   edges2 = Table[edges1[[i]] - eqshape * medges1[[i]], {i, img1, imgN}];
   ftedges = Table[(Abs[Fourier[edges2[[i]], FourierParameters → {-1, 1}]])^2,
     {i, 1, Length[edges2]}];
   pixN2 = pixN / fac;
   ftedges2 = Sum[ftedges[[i]], {i, 1, Length[ftedges]}] / Length[ftedges] //
     RotateLeft[#, pixN2 / 2 + 1] &;
   pref = (.5 kb T / π) ravg;
   fptable1 =
    Table[{pixN2 / 2 - i, pref / (ftedges2[[i]] * (pixN2 / 2 - i)^2)}, {i, 1, pixN2 / 2 - 1}];
   fptable2 = Table[{pixN2 / 2 - i, pref / (ftedges2[[i]] * (pixN2 / 2 - i)^2)},
     {i, pixN2 / 2 + 1, pixN2}];
   fptable = Union[fptable1, fptable2];
   file = "T" <> ToString[T] <> "_L" <>
     ToString[imgN - img1] <> "_N" <> ToString[pixN] <> "_TotalData.dat";
   Export[ToString[file], fptable];
   Print[ravg];
   fptable // ListPlot[#, PlotStyle → {AbsolutePointSize[5], Hue[color]},
      AxesLabel → {"k (mode #)", "β=k_B T R_avg / (2 π k^2 < | r_k | \(\^2\) >  (meV/nm)"},
      PlotRange → All, Epilog →
       Text["Equipartition of Energy of Fourier Modes", Scaled[{1 / 2, 6 / 5}]]] &
  ];
FModesCor[edges_, {img1_, imgN_}, pixN_, fac_, color_] := Module[{edges1 = {},
    edges2 = {}, ftedges = {}, ftedges2 = {}, exList = {}, pixN2, eqshape = {}},

   eqshape = EqShape[edges, imgN, pixN, fac];
   exList = Table[fac i, {i, 1, pixN / fac}] // Partition[#, 1] &;
   edges1 = Table[Extract[edges[[i]], exList], {i, 1, Length[edges]}];
   edges2 = Table[edges1[[i]] - eqshape * Mean[edges1[[i]]], {i, img1, imgN}];
   ftedges = Table[(Abs[Fourier[edges2[[i]], FourierParameters → {-1, 1}]])^2,
     {i, 1, Length[edges2]}]
  ];
FModesData[edges_, {img1_, imgN_}, pixN_, fac_, color_] :=
 Module[{edges1 = {}, edges2 = {}, ftedges = {},
   ftedges2 = {}, exList = {}, pixN2, eqshape = {}},
```

```
  eqshape = EqShape[edges, imgN, pixN, fac];

  exList = Table[fac i, {i, 1, pixN / fac}] // Partition[#, 1] &;
  edges1 = Table[Extract[edges[[i]], exList], {i, 1, Length[edges]}];
  edges2 = Table[edges1[[i]] - eqshape * Mean[edges1[[i]]], {i, img1, imgN}];
  ftedges = Table[(Abs[Fourier[edges2[[i]], FourierParameters → {-1, 1}]])^2,
    {i, 1, Length[edges2]}];
  pixN2 = pixN / fac;
  ftedges2 = Sum[ftedges[[i]], {i, 1, Length[ftedges]}] / Length[ftedges] //
    RotateLeft[#, pixN2 / 2 + 1] &;
  Table[{pixN2 / 2 - i, ftedges2[[i]] * (pixN2 / 2 - i)^2}, {i, 1, pixN2}]
 ]
```

DATA ANALYSIS

■ Data Analysis 1: fitting each C60

■ Read Data

```
SetDirectory["/home/tim/Research/Mathematica/C60Flux/042506"]
```

```
/home/tim/Research/Mathematica/C60Flux/042506
```

```
test = ReadC60["042506m50C60position.txt"] ;

C60data = Array[data, 90];

For[i = 19, i ≤ 85, i++,
 filename = "042506m " <> ToString[i] <> "C60positions.txt";
 C60data[[i]] = ReadC60[filename];
]

C60data[[50]] // ListPlot;
```

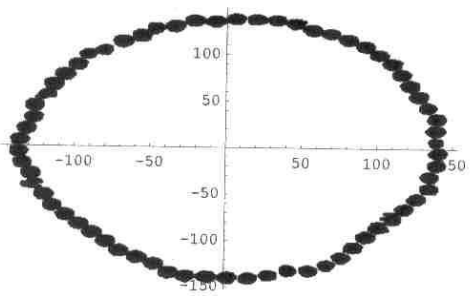

■ Fit Data

```
Clear[i, j, k];
```

Do data analysis on all files and write out to files:

```
For[k = 21, k ≤ 85, k++,
  FindC60[C60data[[k]], .5, "042506m" <> ToString[k] <> "C60positions.dat"];
  Print[k];
 ];
```

Read in output data from files:

```
posC60 = Array[data, 90];

For[i = 19, i ≤ 85, i++,
 filename = "042506m" <> ToString[i] <> "C60positions.dat";
 posC60[[i]] = Import[filename, "List"] // Partition[#, 2] &;
]
```

Test plot some of the data:

```
For[j = 19, j ≤ 19, j++,
  len = Length[posC60[[j]]];
  p1 = posC60[[j]] // ListPlot[#,
       PlotStyle → {Hue[.1], PointSize[.02]}, DisplayFunction → Identity] &;
  p2 = C60data[[j]] // ListPlot[#, DisplayFunction → Identity] &;
  Show[p2, p1, Graphics[Text[StyleForm[ToString[j]], {50, 50}]], PlotRange →
    {{-170, 170}, {-170, 170}} , AspectRatio → 1, DisplayFunction → $DisplayFunction];
];
```

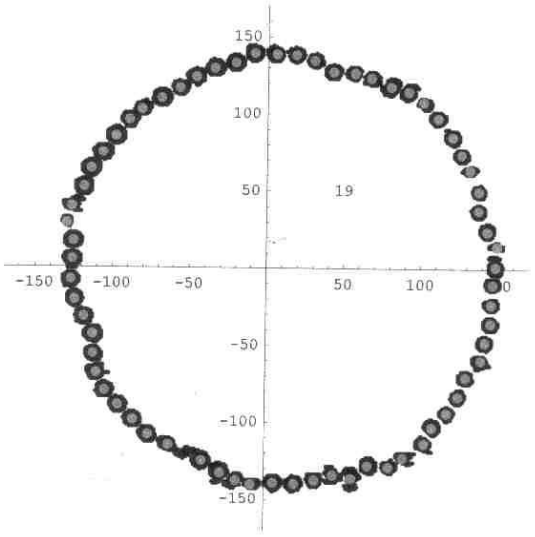

Now lets recorrect for the shift in the center and the stretch factors:

```
cposC60 = Array[data, 90];
cC60data = Array[data, 90];
Clear[avg];
stx = 1.30;
sty = 1.36;
For[j = 19, j ≤ 85, j++,
 avg = Mean[posC60[[j]]];
 cposC60[[j]] = Table[{30/512 * stx * (posC60[[j, k, 1]] - avg[[1]]),
    30/512 * sty * (posC60[[j, k, 2]] - avg[[2]])}, {k, 1, Length[posC60[[j]]]}];
 cC60data[[j]] = Table[{30/512 * stx * (C60data[[j, k, 1]] - avg[[1]]),
    30/512 * sty * (C60data[[j, k, 2]] - avg[[2]])}, {k, 1, Length[C60data[[j]]]}];
]
```

■ Equilibrium Crystal Shape

Here we take one of the islands:

```
posC60[[19]] // ListPlot[#, AspectRatio → 1, PlotStyle → {Hue[.1], PointSize[.04]}] &;
```

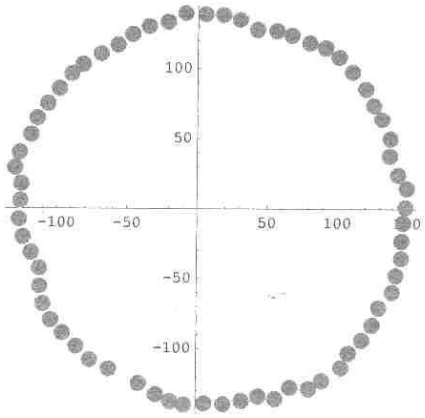

Convert all islands to polar coordinates:

```
posC60polar = Array[data, 85 - 19 + 1];
For[m = 19, m ≤ 85, m++,
  posC60polar[[m - 18]] = Table[{√(cposC60[[m, i, 1]]^2 + cposC60[[m, i, 2]]^2) // N, 360/(2 π)
      ArcTan[cposC60[[m, i, 1]] // N, cposC60[[m, i, 2]]]}, {i, 1, Length[cposC60[[m]]]}];
 ];

posC60polarB = posC60polar // Flatten // Partition[#, 2] &;
```

Place points in degree bins and then average all islands together to get the ECS:

```
del = 5;
posC60polarC =
  Table[Select[posC60polarB, i < #[[2]] < i + del &], {i, -180, 180 - del, del}];

ecs = Table[Mean[posC60polarC[[i]]][[1]], {i, 1, Length[posC60polarC]}];

pecs = ecs // PolarListPlot[#, AspectRatio → 1,
     PlotStyle → {Hue[.1], PointSize[.04]}, PlotRange → {{-13, 13}, {-13, 13}},
     Ticks → {{-12, -10, -8, -6, -4, -2, 2, 4, 6, 8, 10, 12},
       {-12, -10, -8, -6, -4, -2, 2, 4, 6, 8, 10, 12}},
     AxesLabel → {"x(nm)", "y(nm)"}, TextStyle → {FontSize → 22, FontWeight → Bold}] &;
```

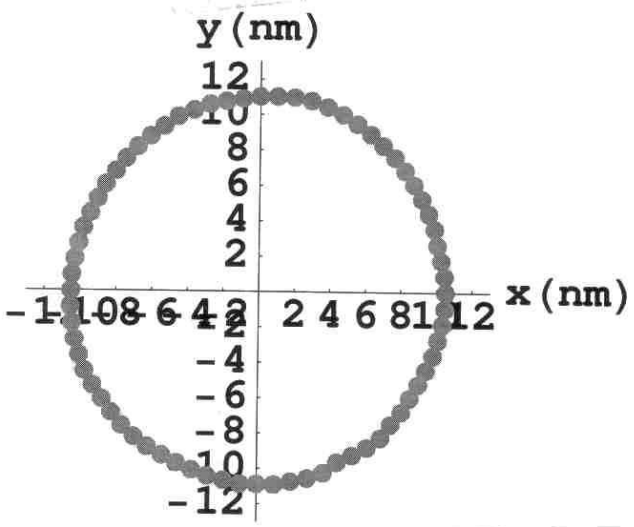

■ Distribution of Angles between C60:

Let's make a histogram of the angle between the C60:

```
vtable = Array[data, 85 - 19 + 1];

For[j = 19, j ≤ 85, j++,
  vtable[[j - 18]] = Table[
     v1 = cposC60[[j, i + 1]] - cposC60[[j, i]];
     v2 = cposC60[[j, i + 2]] - cposC60[[j, i + 1]];
     ArcCos[ v1.v2 / (√v1.v1 √v2.v2) ] * 360/(2π)
     , {i, 1, Length[cposC60[[j]]] - 2}];
];
```

```
C60hist = Histogram[vtable // Flatten,
    AxesLabel → {"θ (deg)", ""}, HistogramRange → {0, 60}, BarStyle → Hue[.1],
   TextStyle → {FontSize → 22, FontFamily → "Arial", FontWeight → Bold},
   Ticks → {{0, 5, 10, 15, 20, 25, 30, 35, 40, 45, 50, 55, 60}, Automatic},
   PlotLabel → "Distribution of Angle Between C60"];
```

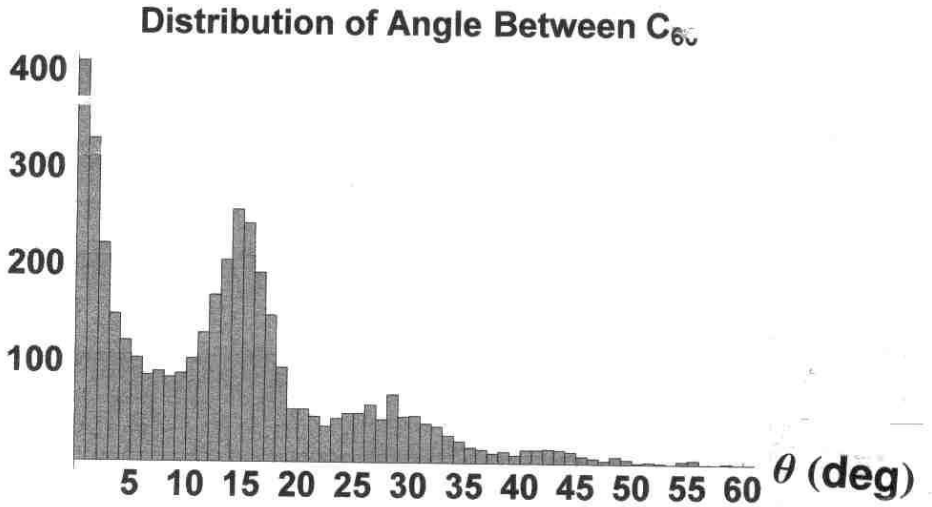

■ **Distribution of Distance between C60:**

Let's make a histogram of the distance between the C60:

```
dtable = Array[data, 85 - 19 + 1];

For[j = 19, j ≤ 85, j++,
  dtable[[j - 18]] = Table[
     v1 = cposC60[[j, i + 1]] - cposC60[[j, i]];
     √(v1.v1)
     , {i, 1, Length[cposC60[[j]] - 1}];
];
```

Printed by Mathematica for Students

```
C60hist = Histogram[dtable // Flatten,
   AxesLabel → {"d (nm)", ""}, BarStyle → Hue[.1], HistogramRange → {0, 2},
   TextStyle → {FontSize → 22, FontFamily → "Arial", FontWeight → Bold},
   PlotLabel → "Distribution of Distance Between C60"];
```

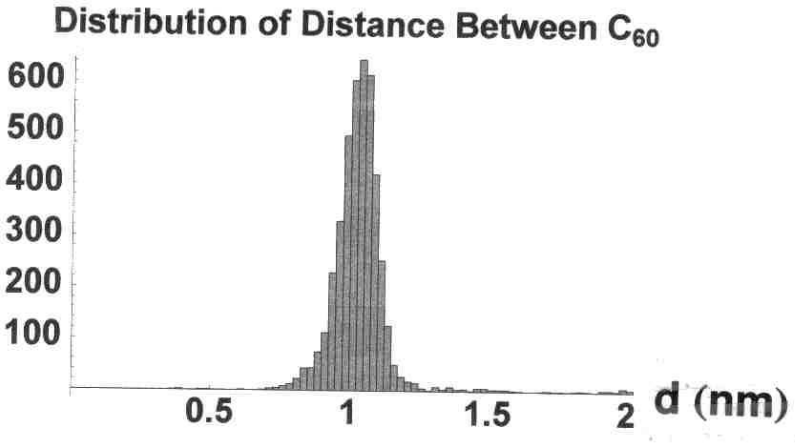

■ Data Analysis 2: fluctuation analysis with ~300 data (individual C60 not resolved)

■ Read Data

```
C60data = Array[data, 400];

For[i = 100, i ≤ 398, i++,
 filename = "042506m " <> ToString[i] <> "C60positions.txt";
 C60data[[i]] = ReadC60[filename];
]

C60data[[200]] // Length
```

```
2873
```

```
C60data[[200]] // ListPlot[#, AspectRatio → 1, PlotStyle → {Hue[.1], PointSize[.02]}] &;
```

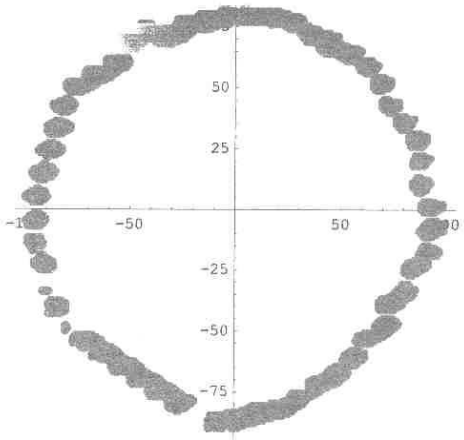

■ Getting equally spaced points around the perimeter

For this data set there are roughly 60 C60s...

```
check = C60data[[250]] //
   ListPlot[#, AspectRatio → 1, PlotStyle → {Hue[.6], PointSize[.02]}] &;

check1 = FluxC60[C60data[[250]], 6, "check.dat"] //
   ListPlot[#, PlotStyle → {Hue[.1], PointSize[.02]}] &;

Show[check, check1];
```

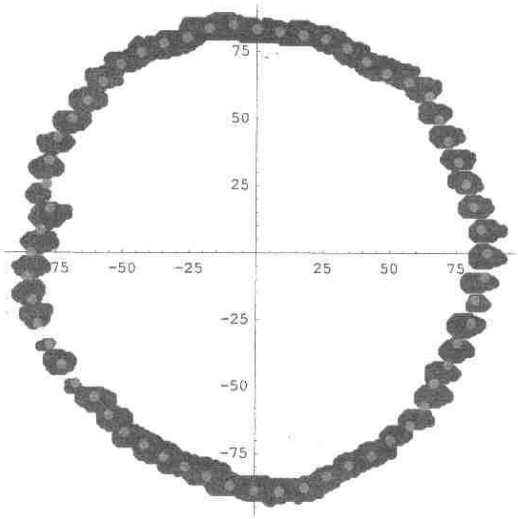

```
For[k = 100, k ≤ 398, k++,
  FluxC60[C60data[[k]], 6, "042506m" <> ToString[k] <> "C60flux_60.dat"];
  Print[k];
 ];
```

Here we read in the images from the files. With 60 C60, which is the proper sampling, we correct for the center offset, the stretch factors, and the pixel to nm conversion:

```
flux60C60 = Array[data, 700];
```

```
Clear[yo];
stx = 1.2922;
sty = 1.3870;
For[i = 100, i ≤ 398, i++,
 filename = "042506m" <> ToString[i] <> "C60flux_60.dat";
 yo = Import[filename, "List"] // Partition[#, 2] &;
 yo2 = Plus[#, -Mean[yo]] & /@ yo;
 flux60C60[[i]] =
  Table[{yo2[[i, 1]] * stx * 40/512, yo2[[i, 2]] * sty * 40/512}, {i, 1, Length[yo2]}]
]
```

```
check2 = flux60C60[[250]] //
   ListPlot[#, AspectRatio → 1, PlotRange → {{-10, 10}, {-10, 10}}] &;
```

```
Show[check, check1, check2];
```

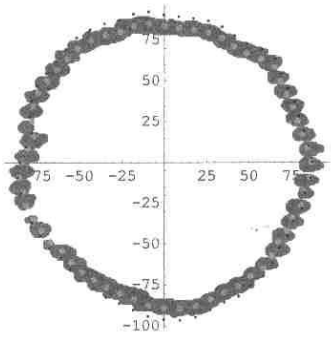

■ ECS and Fluctuation Analysis

Here we take all real images, getting rid of skipped numbers

```
flux60C60b =
  Select[flux60C60, Length[#] == 60 && NumericQ[#[[1, 1]]] == True && #[[1]] ≠ {0, 0} &];
```

Now we convert to polar coordinates:

```
redge60 = Table[Table[√(flux60C60b[[j, i, 1]]^2 + flux60C60b[[j, i, 2]]^2) // N,
    {i, 1, Length[flux60C60b[[j]]]}], {j, 1, Length[flux60C60b]}];
```

Here we can see the equivalence of the near equivalence of this and the original (where each theta wasn't exactly an integer). Notice the required rotation by 180 degrees

```
RotateLeft[redge60[[180]], 30] // PolarListPlot[#, AspectRatio → 1] &;
```

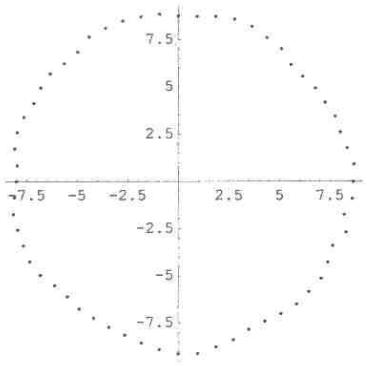


```
flux60C60b[[180]] // ListPlot[#, AspectRatio → 1] &;
```

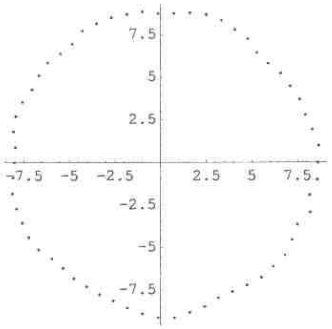

This ECS looks much more circular than the previous one:

```
Show[RotateLeft[EqShape[redge60, Length[redge60], 60, 1], 30] //
   PolarListPlot[#, PlotStyle → {Hue[.1], PointSize[.02]}] &];
```

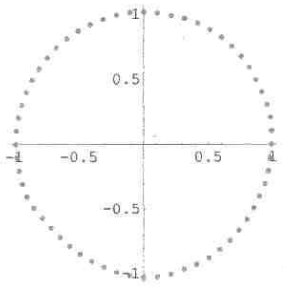

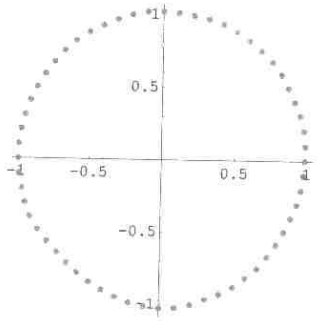

We are now ready to do the fluctuation analysis:

```
FModes[300, redge60, {1, Length[redge60]}, 60, 1, .9];
```

```
8.85107
```

We can import this data from the file it was read to and plot it:

```
alldata60 = Import["T300_L229_N60_TotalData.dat"];
alldata60p = Table[{alldata60[[i, 1]], alldata60[[i, 2]]/10}, {i, 1, Length[alldata60]}];

p60b = alldata60p //
   ListPlot[#, PlotStyle → {Hue[.8], PointSize[.02]}, PlotRange → {{0, 39}, {0, 100}},
     TextStyle → {FontSize → 22, FontFamily → "Arial", FontWeight → Bold},
     AxesLabel → {"k (mode #)", "β (meV/Ang)"}] &;
```

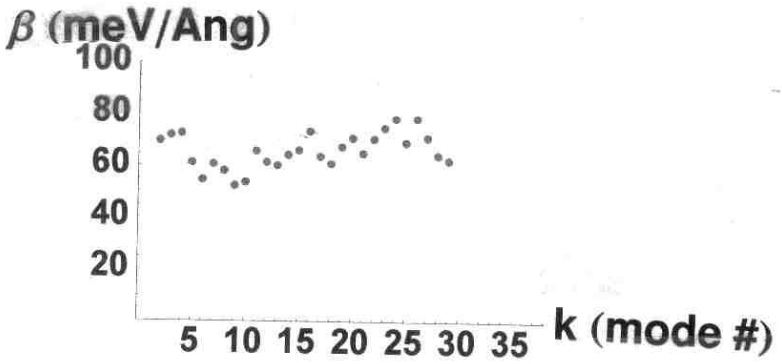

■ Correlation Analysis

```
img = {1, Length[redge60]};
pix = 60;
div = 1;
ftA1 = FModesCor[redge60, img, pix, div, .1];

? AutoCor

AutoCor[{x1,x2,x3,...xn}] returns the step auto-correlation function G(j) = <(xi,j-
  xi)^2>, where <> denotes an average over i, and both i and j vary between 1 and n.

range = Length[redge60];
p6 = AutoCor[Transpose[ftA1][[6]]];
pp6 = p6 // ListPlot[#, PlotRange → {{0, range}, Automatic},
      PlotStyle → {PointSize[.014]}, AxesLabel → {"t(pict. number)", "G(t)"}] &;
p5 = AutoCor[Transpose[ftA1][[5]]];
pp5 = p5 // ListPlot[#, PlotRange → {{0, range}, Automatic},
      PlotStyle → {PointSize[.014], Hue[1]}] &;
p4 = AutoCor[Transpose[ftA1][[4]]];
pp4 = p4 // ListPlot[#, PlotRange → {{0, range}, Automatic},
      PlotStyle → {PointSize[.014], Hue[.8]}] &;
p3 = AutoCor[Transpose[ftA1][[3]]];
pp3 = p3 // ListPlot[#, PlotRange → {{0, range}, Automatic},
      PlotStyle → {PointSize[.014], Hue[.9]}] &;
p2 = AutoCor[Transpose[ftA1][[2]]];
pp2 = p2 // ListPlot[#, PlotRange → {{0, range}, Automatic},
      PlotStyle → {PointSize[.014], Hue[.1]}] &;

p7 = AutoCor[Transpose[ftA1][[7]]];
pp7 = p7 // ListPlot[#, PlotRange → {{0, range}, Automatic}, PlotStyle →
       {PointSize[.014], Hue[.6]}, AxesLabel → {"t(pict. number)", "G(t)"}] &;
p8 = AutoCor[Transpose[ftA1][[8]]];
pp8 = p8 // ListPlot[#, PlotRange → {{0, range}, Automatic},
      PlotStyle → {PointSize[.014], Hue[1]}] &;
p9 = AutoCor[Transpose[ftA1][[9]]];
pp9 = p9 // ListPlot[#, PlotRange → {{0, range}, Automatic},
      PlotStyle → {PointSize[.014], Hue[.8]}] &;
p10 = AutoCor[Transpose[ftA1][[10]]];
pp10 = p10 // ListPlot[#, PlotRange → {{0, range}, Automatic},
      PlotStyle → {PointSize[.014], Hue[.9]}] &;
p11 = AutoCor[Transpose[ftA1][[11]]];
pp11 = p11 // ListPlot[#, PlotRange → {{0, range}, Automatic},
      PlotStyle → {PointSize[.014], Hue[.1]}] &;
```

```
Show[pp10, pp9, pp8, pp7, pp6, pp5, pp4, pp3, PlotRange → {{0, 50}, {0, 0.00012}}];
```

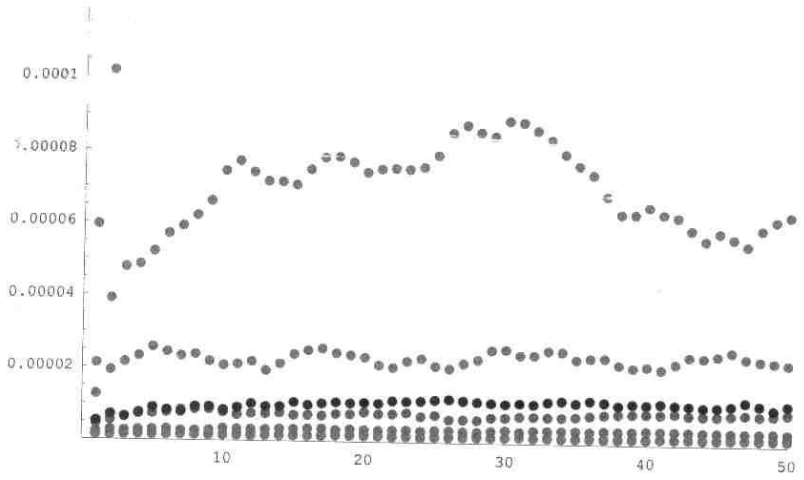

■ Animate

You can make an animation using the following. I show only the first image here:

```
Table[Print[i]; Print[i * 13.1072 "s"];
  fluxC60[[i]] // ListPlot[#, PlotRange → {{-16, 16}, {-16, 16}},
     PlotStyle → {Hue[0], PointSize[.02]}, AspectRatio → 1] &, {i, 20, 624}];
```

```
20

262.144 s
```

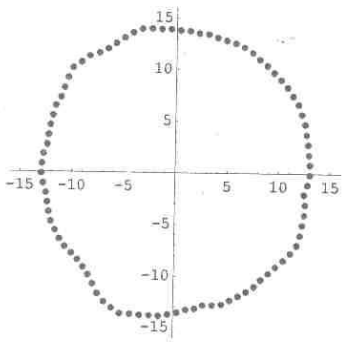

BIBLIOGRAPHY

[1] J. V. Barth, G. Costantini, and K. Kern, Nature **437**, 671 (2005).

[2] J. Tersoff, C. Teichert, and M. G. Lagally, Phys. Rev. Lett. **76**, 1675 (1996).

[3] A. Li, F. Liu, and M. G. Lagally, Phys. Rev. Lett. **85**, 1922 (2000).

[4] A.-L. Barabási, Appl. Phys. Lett. **70**, 2565 (1997).

[5] H.-C. Jeong and E. D. Williams, Surf. Sci. Rept. **34**, 171 (1999).

[6] M. P. A. Fisher, D. S. Fisher, and J. D. Weeks, Phys. Rev. Lett. **48**, 368 (1982), As a historical side note, at the time of writing their response, Fisher, Fisher, and Weeks were at Bell labs, where the noted physicist C. Herring was as well. Although Herring did not play a direct role in the paper, he was surely aware of the orientation dependence of the step line tension. In fact, he wrote extensively on the subject, and poetically referred[20] to polar plots of the free energy as flowers.

[7] D. B. Abraham, Phys. Rev. Lett. **47**, 545 (1981).

[8] H. J. Leamy, G. H. Gilmer, and K. A. Jackson, *Surface Physics of Materials* Vol. 1 (Academic, New York, 1975), p. 121.

[9] Y. Akutsu and N. Akutsu, J. Phys. A: Math. Gen. **19**, 2813 (1986).

[10] A. F. Andreev, Sov. Phys.–JETP **53**, 1063 (1982).

[11] N. C. Bartelt, T. L. Einstein, and E. D. Williams, Surf. Sci. Lett. **240**, L591 (1990), and references therein.

[12] M. Giesen, Prog. Surf. Sci. **68**, 1 (2001).

[13] S. V. Khare and T. L. Einstein, Phys. Rev. B **57**, 4782 (1998).

[14] B. Blagojević and P. M. Duxbury, Phys. Rev. E **60**, 1279 (1999).

[15] N. C. Bartelt, J. L. Goldberg, T. L. Einstein, and E. D. Williams, Surf. Sci. **273**, 252 (1992).

[16] C. Rottman and M. Wortis, Phys. Rev. B **24**, 6274 (1981).

[17] M. Giesen, C. Steimer, and H. Ibach, Surf. Sci. **471**, 80 (2001).

[18] J. W. Cahn and R. Kikuchi, J. Phys. Chem. Solids **20**, 94 (1961).

[19] S. Dieluweit, H. Ibach, M. Giesen, and T. L. Einstein, Phys. Rev. B **67**, 121410(R) (2003).

[20] C. Herring, Phys. Rev. **82**, 87 (1951).

[21] N. Akutsu and Y. Akutsu, Surf. Sci. **376**, 92 (1997).

[22] R. V. Moere, H. J. W. Zandvliet, and B. Poelsema, Phys. Rev. B **67**, 193407 (2003).

[23] R. V. Moere, H. J. W. Zandvliet, and B. Poelsema, Phys. Rev. B **68**, 073404 (2003).

[24] J. E. Avron, H. van Beijeren, L. S. Schulman, and R. K. P. Zia, J. Phys. A: Math. Gen. **15**, L81 (1982).

[25] R. K. P. Zia and J. E. Avron, Phys. Rev. B **25**, 2042 (1982).

[26] W. K. Burton, N. Cabrera, and F. C. Frank, Phil. Trans. Roy. Soc. (London) Series A-Math and Phys. Sci. **243**, 299 (1951).

[27] T. W. Burkhardt, Z. Phys. **29**, 129 (1978).

[28] H. J. W. Zandvliet, H. B. Elswijk, E. J. van Loenen, and D. Dijkkamp, Phys. Rev. B **45**, 5965 (1992).

[29] M. Kollar, I. Spremo, and P. Kopietz, Phys. Rev. B **67**, 104427 (2003).

[30] N. C. Bartelt, T. L. Einstein, and E. D. Williams, Surf. Sci. **276**, 308 (1992).

[31] H. J. W. Zandvliet, Phys. Rev. B **61**, 9972 (2000).

[32] M. Giesen-Seibert and H. Ibach, Surf. Sci. **316**, 205 (1994).

[33] Explicitly, the contribution to the lattice-gas Hamiltonian of all NN bonds is $\epsilon_1 \Sigma_{\langle i,j \rangle} n_i n_j$, where the site-occupation variable $n_i = 0, 1$, and the summation is over all NN pairs of sites. It is well known that $\epsilon_1 \rightarrow -4J_1$ in the corresponding Ising model, so that T_c is determined by $\sinh(|\epsilon_1|/2k_BT) = 1$. Unfortunately, the variety of notations in papers on this subject can and often do lead to confusion. In the papers by Van Moere et al.,[22,23] $\varepsilon_{1,2}$ have the opposite sign of our $\epsilon_{1,2}$. In Giesen et al.[17] and somewhat implicitly in Dieluweit et al.,[19] the so-called Ising parameter, ε, is $\varepsilon_k = 2J = -\frac{1}{2}\epsilon_1$.

[34] C. Steimer, M. Giesen, L. Verheij, and H. Ibach, Surf. Sci. **329**, 47 (2001).

[35] A. Bogicevic, S. Ovesson, P. Hyldgaard, B. I. Lundqvist, H. Brune and D. R. Jennison, Phys. Rev. Lett. **85**, 1910 (2000).

[36] P. J. Feibelman, Phys. Rev. B **60**, 11118 (1999).

[37] Using EAM, C. S. Liu and J. B. Adams, Surf. Sci. **294**, 211 (1993) found $\varepsilon_k = 139$meV. Using a pair-potential expansion from a first-principles database of surface energies, L. Vitos, H. L. Skriver, and J. Kollár, Surf. Sci. **425**, 212 (1999) obtained $\varepsilon_k = 163$meV. With an *spd* tight-binding model, F. Raouafi, C. Barreteau, M. C. Desjonquères, and D. Spanjaard, Surf. Sci. **505**, 183 (2002) calculated $\varepsilon_k = 146$meV.

[38] T. J. Stasevich, T. L. Einstein, and S. Stolbov, Phys. Rev. B **73**, 115426 (2006).

[39] G. Kresse and J. Hafner, Phys. Rev. B **47**, 558 (1993).

[40] G. Kresse and J. Hafner, Phys. Rev. B **49**, 14 251 (1994).

[41] G. Kresse and Furthmüller, Comput. Mater. Sci. **6**, 15 (1996).

[42] G. Kresse and Furthmüller, Phys. Rev. B **54**, 11169 (1996).

[43] T. L. Einstein, *Handbook of Surface Science* Vol. 1 (Elsevier Science, Amsterdam, 1996), Chap. 11.

[44] I. Vattulainen, unpublished, private communication, in conjunction with J. Merikoski, I. Vattulainen, J. Heinonen, and T. Ala-Nissila, Surf. Sci. **387**, 167 (1997).

[45] T. L. Einstein, Langmuir **7**, 2520 (1991).

[46] T. L. Einstein, Surf. Sci. **84**, 497 (1979).

[47] R. Sathiyanarayanan, T. J. Stasevich, and T. L. Einstein, unpublished.

[48] V. Shenoy and C. V. Ciobanu, Surf. Sci. **554**, 222 (2004).

[49] D. B. Abraham and P. Reed, J. Phys. A: Math. Gen. **10**, L121 (1977).

[50] R. K. P. Zia, J. Stat. Phys. **45**, 801 (1986).

[51] In deriving the equivalent of our Eq. (3.5) for honeycomb lattices, N. Akutsu, J. Phys. Soc. Jpn. **61**, 477 (1992) noted that what we call $\eta_{\pm}(\theta)$ can be written $(2/\sqrt{3})\sin(\theta \pm \pi/3)$.

[52] H. Ibach and W. Schmickler, Phys. Rev. Lett. **91**, 016106 (2003), This simple equivalency does not hold for stepped surfaces in an electrochemical system, where the electrode potential ϕ is fixed rather than the surface charge density conjugate to ϕ.

[53] G. Schulze Icking-Konert, M. Giesen, and H. Ibach, Phys. Rev. Lett. **83**, 3880 (1999).

[54] G. H. Wannier, Rev. Mod. Phys. **17**, 50 (1945).

[55] The calculation can be facilitated by writing $\eta_i \equiv a_i \cos\theta + b_i \sin\theta$ and then using Eq. (3.10) to show $\tilde{s}_i = [(b_i^2 - a_i^2)(\cos^2\theta - \sin^2\theta) - 4a_i b_i \sin\theta\cos\theta]/[a_i\cos\theta + b_i \sin\theta]$.

[56] Eq. (3.17) bypasses several intermediate quantities that are important for Zia's[50] general treatment but cumbersome here. Our ψ_2 has the opposite sign from Zia's, and our angle θ—which vanishes for close-packed step orientations—differs by 30° from his. Note also that interchanging ψ_1 and ψ_2 on the LHS of Eq. (3.16) inverts the LHS, from which it is easy to see that $\beta(\theta)$ of Eq. (3.15) is symmetric about $\theta = 30°$. The LHS of Eq. (3.17) is obviously invariant under the interchange of ψ_1 and ψ_2.

[57] N. Akutsu and Y. Akutsu, J. Phys.: Condens. Matter **11**, 6635 (1999).

[58] In Eqs. (4.30)-(4.33) of Akutsu and Akutsu,[57] their W corresponds to our z^2 and their angles, like Zia's,[50,56] differ from ours so that their $\pi/2$ is our 0 and their 0 is our $\pi/6$.

[59] T. J. Stasevich, T. L. Einstein, R. K. P Zia, M. Giesen, H. Ibach, and F. Szalma, Phys. Rev. B **70**, 245404 (2004).

[60] M. Ondrejcek, W. Swiech, C. S. Durfee, and C. P. Flynn, Surf. Sci. **541**, 31 (2003).

[61] J. Krug (private communication).

[62] G. Ehrlich and F. Watanabe, Langmuir **7**, 2555 (1991).

[63] B. N. J. Persson, Surf. Sci. Rept. **15**, 1 (1992).

[64] E. I. Altman and R. J. Colton, Phys. Rev. B **48**, 18244 (1993).

[65] T. Sakurai, X. D. Wang, T. Hashizume, V. Yurov, H. Shinohara, and H. W. Pickering, Appl. Surf. Sci. **87-8**, 405 (1995).

[66] E. I. Altman and R. J. Colton, Surf. Sci. **295**, 13 (1993).

[67] T. Jung, R. Chlittler, J. K. Gimzewski, and F. J. Himpsel, Appl. Phys. A **61**, 467 (1995).

[68] C. Tao, T. J. Stasevich, T. L. Einstein, and E. D. Williams, Phys. Rev. B **73**, 125436 (2006).

[69] S. Kodambaka, V. Petrova, S. V. Khare, D. D. Johnson, I. Petrov, and J. E. Greene, Phys. Rev. Lett. **88**, 146101 (2002).

[70] F. Szalma, H. Gebremariam, and T. L. Einstein, Phys. Rev. B **71**, 035422 (2005).

[71] S. V. Khare and T. L. Einstein, Phys. Rev. B **54**, 11752 (1996).

[72] K. L. Man, A. Pang, T. J. Stasevich, F. Szalma, T. L. Einstein, and M. Altman, unpublished.

[73] L.-L. Wang and H.-P. Cheng, Phys. Rev. B **69**, 165417 (2004).

[74] G. Danker, O. Pierre-Louis, K. Kassner, and C. Misbah, Phys. Rev. E **68**, 020601 (2003).

[75] P. Kuhn and J. Krug, in *Multiscale Modeling of Epitaxial Growth Series*, edited by A. Voigt, Basel, 2005, Birkhäuser, cond-mat/0405068.

[76] M. Giesen and S. Dieluweit, J. Mol. Catal. A-Chem. **216**, 263 (2004).

[77] J.-S. McEwen, S. H. Payne, and C. Stampfl, Chem. Phys. Lett. **361**, 317 (2002).

[78] W. Luo and K. A. Fichthorn, Phys. Rev. B **72**, 115433 (2005).

[79] A. P. J. Jansen and W. K. Offermans, ICCSA 2005, LNCS **3480**, 1020 (2005).

[80] T. J. Stasevich, H. Gebremariam, T. L. Einstein, M. Giesen, C. Steimer, and H. Ibach, Phys. Rev. B **71**, 245414 (2005).

[81] P. Hohenberg and W. Kohn, Phys. Rev. **136**, B864 (1964).

[82] W. Kohn and L. J. Sham, Phys. Rev. **140**, A1133 (1965).

[83] J. P. Perdew, *Electronic Structure Theory of Solids* (Academie Verlag, Berlin, 1991).

[84] J. P. Perdew, J. A. Chevary, S. H. Vosko, K. A. Jackson, M. R. Pederson, D. J. Singh, and C Fiolhais, Phys. Rev. B **46**, 6671 (1992).

[85] M. Methfessel and A. T. Paxton, Phys. Rev. B **40**, 3616 (1989).

[86] J. Neugebauer and M. Scheffler, Phys. Rev. B **46**, 16 067 (1992).

[87] K. A. Fichthorn and M. Scheffler, Phys. Rev. Lett. **84**, 5371 (2000).

[88] K. A. Fichthorn, M. L. Merrick, and M. Scheffler, Phys. Rev. B **68**, 041404(R) (2003).

[89] This behavior is in contrast, for example, to semiempirical studies of a few kinds of adsorbates on Pt(001), where sizable differences existed between chain and compact clusters, due seemingly to substantial configuration-dependent lateral relaxations; see A. F. Wright, M. S. Daw, and C. Y. Fong, Phys. Rev. B **42**, 9409 (1990).

[90] C. Fiolhais, L. M. Almeida, and C. Henriques, Prog. Surf. Sci. **74** (2003).

[91] D. Spišák, Surf. Sci. **489**, 151 (2001).

[92] X. Wang, Y. Jia, Q. Yao, F. Wang, J. Ma, and X. Hu, Surf. Sci. **551**, 179 (2004).

[93] H. S. Johnston and C. A. Parr, J. Am. Chem. Soc. **85**, 2544 (1963).

[94] N. A. Levanov, A. A. Katsnel'son, A. É. Moroz, V. S. Stepanyuk, W. Hergert, and K. Kokko, Phys. Solid State **41**, 1216 (1999).

[95] M.-C. Marinica, C. Barreteau, M.-C. Desjonquères, and D. Spanjaard, Phys. Rev. B **70**, 075415 (2004).

[96] R. C. Nelson, T. L. Einstein, S. V. Khare, and P. J. Rous, Surf. Sci. **295**, 462 (1993).

[97] M. Schimschak and J. Krug, Phys. Rev. Lett. **78**, 278 (1997).

[98] M. Schimschak and J. Krug, Phys. Rev. Lett. **80**, 1674 (1998).

[99] O. Pierre-Louis and T. L. Einstein, Phys. Rev. B **62**, 13697 (2000).

[100] K. Thürmer, D.-J. Liu, E. D. Williams, and J. D. Weeks, Phys. Rev. Lett. **83**, 5531 (1999).

[101] E. Bänsch, F. Hausser, O. Lakkis, B. Li, and A. Voigt, J. Comput. Phys. **194**, 409 (2004).

[102] E. Bänsch, F. Hausser, and A. Voigt, SIAM J. Sci. Comput. **26**, 2029 (2005).

[103] J. D. Faires and R. Burden, *Numerical Methods*, 2nd Ed. (Brooks/Cole Publishing Co., Pacific Groves, 1998).

[104] L. Balykov and A. Voigt, Multiscale Model. Simul. **5**, 45 (2006).

[105] J. Krug, H. T. Dobbs, and S. Majaniemi, Z. Phys. B **97**, 281 (1995).

[106] T. J. Stasevich, C. Tao, F. Hausser, A. Voigt, E. D. Williams and T. L. Einstein, unpublished.

[107] In Rottman and Wortis[16] there appears to be a pair of sign or letter typos in Eq. 11.